Addis Ababa University
College of Technology & Built Environment
Center for Renewable Energy Technology

Development of Solar Baking Oven Integrated with Linear Fresnel Parabolic Mirror Reflector (LFPMR)

By

Abiyot Lakew (GSR/5450/15)

Advisor

Dr. Solomon Tesfamariam

A Thesis Submitted to the School of Graduate Studies of Addis Ababa University in Partial Fulfillment of the Requirements for the Degree of Master of Science in Renewable Energy Technology

February 2026
Addis Ababa, Ethiopia

Addis Ababa University

College of Technology & Built Environment

Center for Renewable Energy Technology

"Development of Solar Baking Oven Integrated with Linear Fresnel Parabolic Mirror Reflector (LFPMR)"

By

Abiyot Lakew

Approved by Board of Examiners:

Solomon T/mariam		05/03/2026
Advisor	Signature	Date
Mesfin Belayneh (PhD)		05/03/2026
Internal Examiner	Signature	Date
Kamil Dino Adem (PhD)		05/03/2026
External Examiner	Signature	Date
Ebrahim T/[illegible] (PhD)		06/03/2026
Chairman	Signature	Date
Director, Postgraduate Program	Signature	Date

Declaration

I, the undersigned, hereby declare that the thesis entitled “Development of a Solar Baking Oven Integrated with a Linear Fresnel Parabolic Mirror Reflector (LFPMR)” is my original work. I affirm that this study has been carried out in accordance with accepted ethical and scholarly standards, and that all sources of information and materials used in the preparation of this thesis have been duly acknowledged.

This thesis is submitted in partial fulfillment of the requirements for the degree of Master of Science in Renewable Energy Technology at Addis Ababa University, College of Technology and Built Environment, Center for Renewable Energy Technology. The thesis is deposited in the University’s Library and is made available to users in accordance with the library regulations.

I further declare that this thesis has not been submitted, in whole or in part, to any other institution for the award of any academic degree, diploma, or certificate.

Author	Signature	Date

Advisor	Signature	Date

DEDICATION

I dedicate this thesis manuscript to my beloved wife and daughter for their encouragement, loving support and being always enthusiastic to see my success.

ACKNOWLEDGEMENTS

First and foremost, I would like to express my sincere gratitude to my advisor, Dr. Solomon Tesfamariam, for his invaluable guidance, continuous support, and constructive feedback throughout the course of this research. His technical insight, encouragement, and Supportive mentality were second to none in shaping this study and ensuring its successful completion.

I am deeply grateful to the faculty members of the Center for Renewable Energy Technology, College of Technology and Built Environment, Addis Ababa University, for providing the academic foundation, resources, and learning environment necessary for this work.

Finally, I would like to express my heartfelt appreciation to my family and friends for their unwavering moral support, patience, and encouragement throughout my academic journey. Their belief in me provided the motivation and resilience needed to complete this work.

Above all, I am grateful to God for the strength, perseverance, and opportunity to successfully complete this study.

ABSTRACT

The increasing demand for sustainable medium-temperature thermal energy applications highlights the need for cost-effective solar thermal technologies. This study presents the numerical modeling, simulation, and experimental validation of a solar baking oven integrated with a Linear Fresnel Parabolic Mirror Reflector (LFPMR). Optical performance was evaluated using Monte Carlo ray-tracing simulations in SolTrace to assess flux distribution, absorbed power, and optical efficiency under two aiming strategies: plate-based aiming (Case 1) and global aiming (Case 2). Under a direct normal irradiance of 1,000 W/m² and an aperture area of 5.13 m², Case 1 produced an absorbed power of 1.64 kW, corresponding to an optical efficiency of 36%. In contrast, Case 2 increased the absorbed power to 2.22 kW and improved the optical efficiency to 49.7%, indicating significantly enhanced solar energy capture with the global aiming approach. Thermal behavior and airflow within the baking chamber were analyzed using ANSYS Fluent, incorporating the optical heat flux as a boundary condition. The simulations predicted stable air temperatures ranging from 425 to 443 K and buoyancy-driven convection that promotes uniform heat transfer across baking trays. A prototype was fabricated and experimentally tested under no-load and load conditions. The oven achieved a stagnation temperature of 330°C, corresponding to a first figure of merit of 0.37. Bread baking tests demonstrated successful baking of 9.2 kg of dough within 70 minutes at tray temperatures between 201 and 250 °C, with an overall system efficiency of 36%. The results confirm that LFPMR-based solar thermal systems offer a technically viable and energy-efficient solution for medium-temperature applications such as solar baking, with potential for decentralized and community-scale deployment.

***Keywords**: Solar baking oven; Linear Fresnel Parabolic Mirror Reflector; SolTrace; ANSYS Fluent; Optical efficiency; Thermal performance; Renewable energy*

Contents

Declaration **i**

ACKNOWLEDGEMENTS **iii**

ABSTRACT **iv**

List of Figures **viii**

List of Tables **xi**

List of Acronyms and Abbreviations **xii**

Chapter 1 Introduction **1**

- 1.1 Background of the Study 1
- 1.2 Problem Statement 3
- 1.3 Objectives of the Study 4
    - 1.3.1 General Objectives 4
    - 1.3.2 Specific Objectives 4
- 1.4 Scope and limitation of the Study 5
- 1.5 Significance of the Study 5
- 1.6 Organization of the Thesis 6

Chapter 2 Literature Review **7**

- 2.1 Overview of solar cooking technologies 7
- 2.2 Classification of solar cooker 10
    - 2.2.1 Direct solar cookers 11
    - 2.2.2 Indirect solar cookers 20

Chapter 3 Materials and Methods **38**

- 3.1 System Description 38
- 3.2 Materials Selection 41
- 3.3 Measuring Instruments and Experimental setup 43

3.4 Simulation model development 46

3.4.1 Geometry and model setup 46

3.4.2 Geometry preparation and global alignment 48

3.5 Governing equations 55

3.5.1 Radiation model 55

3.5.2 Turbulent model 56

3.6 Numerical methods and Boundary conditions 57

3.7 Performance analysis 59

3.7.1 Concentration ratios 59

3.7.2 Intercept factor 59

3.7.3 Optical efficiency 60

3.7.4 Figure of merit 60

3.7.5 Thermal efficiency of the system 60

3.7.6 Water boiling test 61

Chapter 4 Results and Discussion 63

4.1 Simulation Result 63

4.1.1 Optical model result 64

4.1.2 Receiver Energy and Optical Efficiency 66

4.1.3 Surface Heat Flux Characteristics and Flux Distribution 68

4.1.4 Thermal simulation result 69

4.2 Experimental Result 76

4.2.1 No load result 78

4.2.2 The load test 82

Chapter 5 Conclusion and Recommendations 88

5.1 Conclusion 88

5.2 Recommendations 90

Reference 92

Appendix 102

Appendix A: Materials for Solar Bakery Construction 102

Appendix B: Experimental data collection format 103

Appendix C: ANSYS exporter for SolTrace 105

Appendix D: SolTrace lk script 106

Appendix E: ANSYS UDF 109

Appendix F: Part drawings 110

Appendix G: Construction of Prototype 112

List of Figures

Fig. 2.1 The global impact of the solar cookers application [4] 8
Fig. 2.2 Different types of solar cookers.. 10
Fig. 2.3 Different types and modification of solar box cookers Box type cooker: (a) without reflector and (b to f) with single, two, three, four and eight reflectors [32] 11
Fig. 2.4 Solar box cooker with reflector and insulated box cover with transparent cover [11].... 12
Fig. 2.5 Solar panel cooker with cooking pot and reflector [11] 12
Fig. 2.6 Novel Box-type solar oven [33] 14
Fig. 2.7 Box type solar baking oven integrated with a parabolic reflector [31] 15
Fig. 2.8 non-tracking box-type solar cooker integrated with CPC as booster-reflector with step absorber (lift-side) and integrated into building (right-side) [30]... 16
Fig. 2.9 Solar concentrator cooker [11] 17
Fig. 2.10 Solar injera fryer setup [29]... 17
Fig. 2.11 Solar baking oven [35] 18
Fig. 2.12 Tube type direct solar oven bread baking system [36].. 19
Fig. 2.13 Parabolic concentrator solar bread cooker [37].. 20
Fig. 2.14 Schematic diagram of the twin vessel solar cooking system (TWSCS) [39] 21
Fig. 2.15 Simulated solar oven geometry [22].. 22
Fig. 2.16 the novel solar bakery unit using metal hydride based thermal energy storage system [51].. 23
Fig. 2.17 Solare oven integrated with evacuated tube solar collectors and compound parabolic concentrators (ETCs-CPC) [40].. 24
Fig. 2.18 Scheffler reflector Solar baking system [41]&[42] 25
Fig. 2.19 Parabolic dish concentrator using indirect solar Injera stove [38] 26
Fig. 2.20 solar Injera baking system [43] 27
Fig. 2.21 Linear Fresnel collectors with the cavity receiver [44] 27
Fig. 2.22 Linear Fresnel field showing only two receiver target point (left-side) and single and multi-tube receiver (right-side) [45] 28
Fig. 2.23 Linear Fresnel collectors with a multi-tube receiver [46] 29
Fig. 2.24 (a) Linear Fresnel (LF), (b) parabolic trough (PT) and (c) central receiver (CR) [47] . 30

Fig. 2.25 Fresnel concentrator with cavity absorber (left-side) and Fresnel reflector SolTrace model (right-side) [48] 31
Fig. 2.26: Cross Linear concentrated solar power (left-side) and SolTrace optical simulation model (right-side) [49] 32
Fig. 2.27 linear Fresnel reflector solar concentrating Hot Water system [50] 32
Fig. 3.1 Manual tracked linear Fresnel parabolic mirror reflector (LFPMR) system configuration 38
Fig. 3.2 Concentrating solar baking oven parts 40
Fig. 3.3 Mirror reflector and transparent glass with absorber plates 42
Fig. 3.4 Insulation blanket and bakery with frame 42
Fig. 3.6 K type thermocouples integration over different position of the solar oven 44
Fig. 3.7 Solar radiation measurement using solar power meter in prototype testing 45
Fig.3.8 Electronic balance 45
Fig. 3.9 Model integration layout and inputs of SolTrace and ANSYS modelling software 47
Fig. 3.10 The meshed geometry of the solar oven 48
Fig. 3.11 The exported bottom part of the solar oven showing the absorber in green, the glass in red and sidewall in yellow 49
Fig. 3.12 The mirror field and the receiver geometry definition in SolTrace 51
Fig. 3.13 Aiming at plane perpendicular to the mirror field (a) and aiming at global plane parallel to the mirror field (b) 52
Fig. 3.14 Mirror aiming point grouping 53
Fig. 4.1 Global horizontal irradiance (GHI) and ambient temperature for 5/25/2024 63
Fig. 4.2 SolTrace stage definition for the solar oven receiver and mirror field 64
Fig. 4.3 Ray count with average absorber flux 65
Fig. 4.4 SolTrace ray tracing parameters applied in this study 66
Fig.4.5 Ray distribution at different stages 67
Fig. 4.6 Flux distribution through the absorber plates elements for case one (left) and case two (right) 68
Fig.4.7 Power distribution through the absorber plate elements for case one (left) and case two (right) 69
Fig.4.8 Simulation convergence control through area weighted average temperature 70

Fig.4.9 Temperature contour at the mid plane of the solar oven 71
Fig. 4.10 Wall temperature contour of the absorber plates.. 72
Fig. 4.11 Velocity vector plot at the mid plane of the solar baking chamber 73
Fig. 4.12 Density variation (left-side) and pressure variation (right-side) of air inside the solar oven 74
Fig.4.13 Turbulent intensity of the air inside the solar oven 75
Fig.4.14 The measured and satellite global horizontal irradiance (GHI) and direct normal irradiance (DNI) for 5/25/2024 76
Fig.4.15 The measured and satellite global horizontal irradiance (GHI) and direct normal irradiance (DNI) for 5/30/2024 77
Fig.4.16 The measured and satellite global horizontal irradiance (GHI) and direct normal irradiance (DNI) for 6/4/2024 77
Fig.4.17 The measured air temperature over baking trays for the day of 5/20/2024 for no load condition 78
Fig.4.18 The measured air temperature over baking trays for the day of 5/25/2024 for no load condition 79
Fig. 4.19 The measured air temperature over baking trays for the day of 6/4/2024 for no load condition 79
Fig.4.20 The absorber temperature and direct normal irradiance (DNI) for 6/4/2024 no load condition 81
Fig. 4.21 Water and oven air temperature with direct normal irradiance (DNI) for 5/31/2024 water boiling test in load condition.. 83
Fig. 4.22 The linear fit of Q''/Ib vs. $(Twm - Ta)/Ib$.. 84
Fig.4.23 The measured tray air temperature with the absorber temperature for the day of 5/30/2024 for load condition.. 85
Fig.4.24 Bread crumb temperature 86
Fig. 4.25 Baking process and baked bread texture 86

List of Tables

Table 2.1 Different types of cooking and their type of heat transfer mechanisms [9] 9
Table 2.2 Comparison of different solar cooker [28] 13
Table 2.3 literature review summary 33
Table 3.1 Optical parameters used in the LK script.. 54
Table 3.2 Thermo-physical properties of the air... 58
Table 3.3 Solar oven material properties 58
Table 4.1 Result of average flux on absorber plate with ray count and percentage difference 65
Table 4.2 Result of the optical model 67
Table 4.3 Baking chamber air temperature over the trays for no load experiment 80
Table 4.4 Temperature of the trays from the simulation and experiment with the percentage error 82

List of Acronyms and Abbreviations

Symbol	Name (unit)
P_0, P_1, P_2	Coordinates of the triangle
x_m	Triangular face centroid
$\hat{n}_m$	Unit normal
A	Area
R_y	Rotational matrix
t	Translation vector
F_{row}	Focal length
δ	Solar declination angle
ω	Hour angle
α	Solar altitude
A	Azimuth angle
$\emptyset$	Latitude of the place
N	Day number of the year
s_x , s_y and s_z	Sun vector in x,y and z
H	Mirror centroid
ρ	Density of air (kg/m^3)
$\vec{v}$	Fluid velocity vector, (m/s)
∇p	Static pressure gradient, (Pa)
$\bar{\bar{\tau}}$	Stress tensor, (N/m^2)
g	Gravitational acceleration, (m/s^2)
$\vec{F}$	Momentum source term, (kg/ m^{2}s^2)
E	Total energy transfer, (J/kg)
k	Thermal conductivity
E	Enthalpy of dry air, (J/ kg)
S_h	Volumetric heat sources, (W/m^3)
R	Specific gas constant, (J/kg K)
T	Temperature of air, (K)
σ	Stefan-Boltzmann constant
F_{ij}	View factor
ε_i	Emissivity
J_i	Radiosity
Ra	Rayleigh number
β	Coefficient of thermal expansion (K^{-1})
κ	Turbulent kinetic energy, (m^2/s^2)

$\overset{\equiv}{\tau}$	Stress tensor, (N/m^2)
μ_t	Turbulent viscosity, (N s/m^2)
CR_m	Concentration ratio
A_{am}	Mirror concentrator surface area (m^2)
A_{ab}	Absorber surface area (m^2)
Γ	Intercept factor
η_{opt}	Optical efficiency
F_1	First figure of merit
F_2	Second figure of merit
T_{ps}	Stagnation temperature
T_{amb}	Average ambient temperature
I_b	Direct normal radiation
Q_u	Useful energy
$\eta_{th,sys}$	Thermal efficiency
Q_{sh}	The sensible heat (kJ/kg)
Q_{lh}	Latent heat (kJ/kg)
$\mathrm{c_{pb}}$	Specific heat of bread (J/kg.°C.)
$\dot{Q}''$	Rate of useful energy
F'	Heat exchange efficiency factor
COR	Opto-thermal ratio
h_a	Enthalpy of dry air, (J/ kg)
C_a	Specific heat of air, (kj/kg K)
P_a	Atmospheric pressure, (N/m^2)

Chapter 1

Introduction

1.1 Background of the Study

In recent years, the global emphasis on sustainability has prompted significant research into mitigating the environmental impact of various human activities, including cooking and food preparation. Traditional cooking methods, often reliant on biomass and fossil fuels, continue to pose significant challenges globally, particularly in developing regions [1], [2]. An estimated 2.4 billion people globally still depend on solid fuels for cooking and no access to clean cooking appliance [3], leading to indoor air pollution and adverse health effects [4]. Additionally, the combustion of biomass and fossil fuels contributes to deforestation and greenhouse gas emissions, aggravating environmental degradation and climate change [5].

Ethiopia, like many countries in sub-Saharan Africa, faces challenges associated with reliance on biomass fuels for cooking, which contributes to indoor air pollution, deforestation, and adverse health outcomes [6]. Although attempts have been made to enhance the availability of clean cooking options, a significant segment of Ethiopia's population continues to face a deficiency in modern energy resources for cooking, especially in rural regions [6].

In response to these challenges, there has been a growing interest in sustainable cooking technologies, with solar cooking emerging as a promising solution. Solar cooking harnesses the abundant and renewable energy of the sun to generate heat, offering a clean, environmentally friendly, and cost-effective cooking alternative [7]. Among solar cooking devices, concentrating solar ovens have gained much attention for their ability to concentrate sunlight onto a cooking chamber, enabling faster cooking times and higher temperatures [1].

Concentrating solar ovens typically utilize reflective surfaces, such as mirrors, which focus sunlight onto a cooking vessel or chamber. By concentrating solar radiation, this oven can achieve temperatures sufficient for baking, boiling, and roasting, making them versatile for a range of cooking applications [8], [9].

However, despite their potential benefits, the widespread adoption of concentrating solar ovens faces several challenges. Designing efficient solar ovens requires considerations of several factors such as thermal insulation, concentrator design, tracking mechanisms, and materials selection [10], [11]. Furthermore, the performance of solar ovens may vary depending on factors such as geographical location, weather conditions, and user behavior [12].

A significant research gap exists in the field of concentrating solar baking ovens, offering an opportunity to create cost-effective solutions that positively impact communities [13]. This study aims to bridge this gap by developing and evaluating a cost-effective solar baking oven integrated with linear Fresnel Parabolic Mirror Reflector (LFPMR). By building on recent advancements in solar technology, this study aims to advance sustainable cooking practices and promote the adoption of solar energy solutions, particularly in the Ethiopian context. The objective is to provide a reliable and affordable solar baking technology that reduces dependence on biomass and supports sustainable development.

This research aims to develop and evaluate the performance of a solar baking oven capable of baking bread while reducing reliance on biomass fuels. It addresses the limited application and performance evaluation of linear Fresnel parabolic mirror reflectors in solar baking systems by experimentally and numerically assessing a prototype integrated with a solar baking oven. The study demonstrates the practical potential of this technology, particularly in regions such as Ethiopia where access to clean cooking solutions remains limited.

1.2 Problem Statement

Ethiopia has significant potential for solar cooking [14], yet currently, less than one percent of this energy resource is being utilized [14], [15]. The primary challenges include optimizing the design of solar cookers to achieve high thermal efficiency, ensuring reliable performance across varying climatic conditions, and adapting the technology for diverse baking processes and products.

While advancements in solar energy technologies have shown significant promise, their practical application in specific areas such as solar baking remains relatively underexplored. Concentrating solar energy systems, which utilize mirrors or lens to focus sunlight onto a small area, have been demonstrated to enhance energy efficiency across various applications, including solar thermal power generation and industrial processes [12]. However, the integration of these technologies into everyday applications, such as baking, presents a unique set of challenges that have not been extensively studied.

Research has shown that while concentrating solar technologies have seen successful application in large-scale industrial settings, their potential for small-scale and domestic use remains largely unexplored [4], [12], [16]. This gap in research limits the broader adoption of solar baking technologies, which could otherwise contribute significantly to sustainable energy solutions and reduce reliance on non-renewable energy sources.

Addressing these challenges requires a detailed investigation into the modeling, optimization, and practical performance of concentrating solar baking ovens. This study aims to fill this gap by providing an in-depth performance analysis of solar baking oven integrated with linear Fresnel parabolic mirror reflector, evaluating its efficiency and practicality.

1.3 Objectives of the Study

1.3.1 General Objectives

The main objective of the study is to model, simulate, construct and assess the performance of solar baking oven integrated with Linear Fresnel Parabolic Mirror Reflector, with the aim of developing a sustainable and energy-efficient solution for bread baking applications.

1.3.2 Specific Objectives

- To develop a model and perform numerical simulations of a concentrating solar baking oven for performance optimization.
- To construct a concentrating solar baking oven prototype with a focus on maximizing solar energy concentration.
- To experimentally evaluate and validate the performance of the solar baking oven prototype under real operating conditions.

1.4 Scope and limitation of the Study

The scope of this study encompasses the modelling, simulation, fabrication of prototype, and performance evaluation of a concentrating solar baking oven. The research focuses on developing an optimized design through simulation, constructing a functional prototype, and thoroughly testing its performance. While the study aims to provide comprehensive insights, there are limitations to consider. The performance evaluation will be conducted in a specific geographic location and season with particular solar conditions, which may affect the generalizability of the results. Additionally, the study will be based on a single prototype design, and results may vary with different designs or configurations.

1.5 Significance of the Study

This study is significant in several aspects. First, it supports global efforts to reduce greenhouse gas emissions and reliance on fossil fuels by demonstrating the feasibility of solar energy for bread baking applications. The adoption of solar-powered baking systems can substantially reduce the environmental and health impacts associated with conventional cooking fuels.

Second, the proposed solar baking system offers important economic benefits, particularly in regions with high solar resource availability. By reducing or eliminating fuel costs, the system has the potential to improve the livelihoods of small-scale bakeries and households, while enhancing energy access and affordability.

Third, this research contributes to the advancement of solar cooking and baking technologies by providing detailed insights into system design, optical and thermal performance evaluation, and experimental validation. The combined use of numerical simulation and prototype testing strengthens the understanding of system behavior and supports design optimization.

Finally, evaluating the system under practical operating conditions provides valuable information for developing solar baking technologies that are efficient, scalable, and adaptable to diverse user needs. This contributes to the wider adoption of renewable energy–based cooking solutions and supports the transition toward sustainable and environmentally friendly technologies.

1.6 Organization of the Thesis

This thesis is organized into five chapters. Chapter one presents the background of the study, the problem statement, research objectives, scope and limitations, significance of the research, and the overall structure of the thesis. Chapter two provides a comprehensive review of the literature on solar baking ovens, concentrating solar technologies, Linear Fresnel reflectors, optical–thermal modeling approaches, and performance evaluation techniques, highlighting existing gaps and theoretical foundations. Chapter three describes the materials and methods adopted in this study, including system modeling, numerical simulations, and experimental testing procedures. Chapter four presents the numerical and experimental results, along with detailed analysis, validation, and performance evaluation. Finally, Chapter five summarizes the key findings, draws conclusions, and provides recommendations for future research and system improvement. The thesis concludes with references and appendices containing simulation codes, material specifications, technical drawings, and experimental data collection formats.

Chapter 2

Literature Review

This chapter examines the existing body of research on solar ovens that utilize concentrated solar power for cooking and baking. It starts with an overview of solar cooking technologies and the principles behind solar concentration and then explores materials selection and key design considerations, emphasizing the factors that influence thermal performance and the evaluation metrics used to assess these systems. Finally, it identifies critical research gaps in the field of concentrating solar ovens that lay the groundwork for future studies and advancements in the technology.

2.1 Overview of solar cooking technologies

Energy is a fundamental driver of human development and survival and it is widely recognized as a critical factor in economic growth and development [17]. To mitigate and reduce the current environmental crises, effective utilization and development of an energy efficient alternative and renewable energy resources were found to be the focus of the twenty first century policy making and research [17].

Cooking is one of the major energy intensive processes in any part of the world due to its importance to human survival. In United States of America, the energy used for cooking accounts between 37% and 53% of the total energy consumption. In developing nations, like sub-Saharan Africa, the energy from firewood, biomass, conventional fuels and electricity accounts 80% of the energy use for cooking food [8]. Solar energy is a sustainable alternative for energy-intensive processes such as cooking because it is renewable and environmentally friendly [8], [17], [18].

Solar energy has been used for cooking food after the age of civilization and the first reported publication of solar cooker, a box cooker, was used to cook a fruit is published by Horace de Saussure in the 1767 [11]. Over the past four decades, solar cooking technology has been regarded as a tool for combating poverty in developing countries due to its minimal environmental impact. With advances in research, the application of solar energy has gained increasing acceptance across various fields, including solar cooking [4].

It is estimated that more than 3.7 million solar cookers have been deployed worldwide, providing cooking services equivalent to approximately 7 billion food preparations for about 13.4 million people globally [19]. It is also reported around 40% of the global population uses fire wood for cooking [20]. In developing countries, it was reported in 2018 that about 2.65 billion people has no access to clean cooking appliance [19] and specifically in Ethiopia the figures shows that only 10% of the population has access to clean cooking [21].

In developing countries, household air pollution due to the use of fire wood or other traditional sources of fuel contributes for 3.2 million deaths. According to reports from 2020, among these deaths, approximately 237,000 occurred in children under five years of age [4].. Fig. 2.1 shows the impact of solar cooking application in different sectors [4].

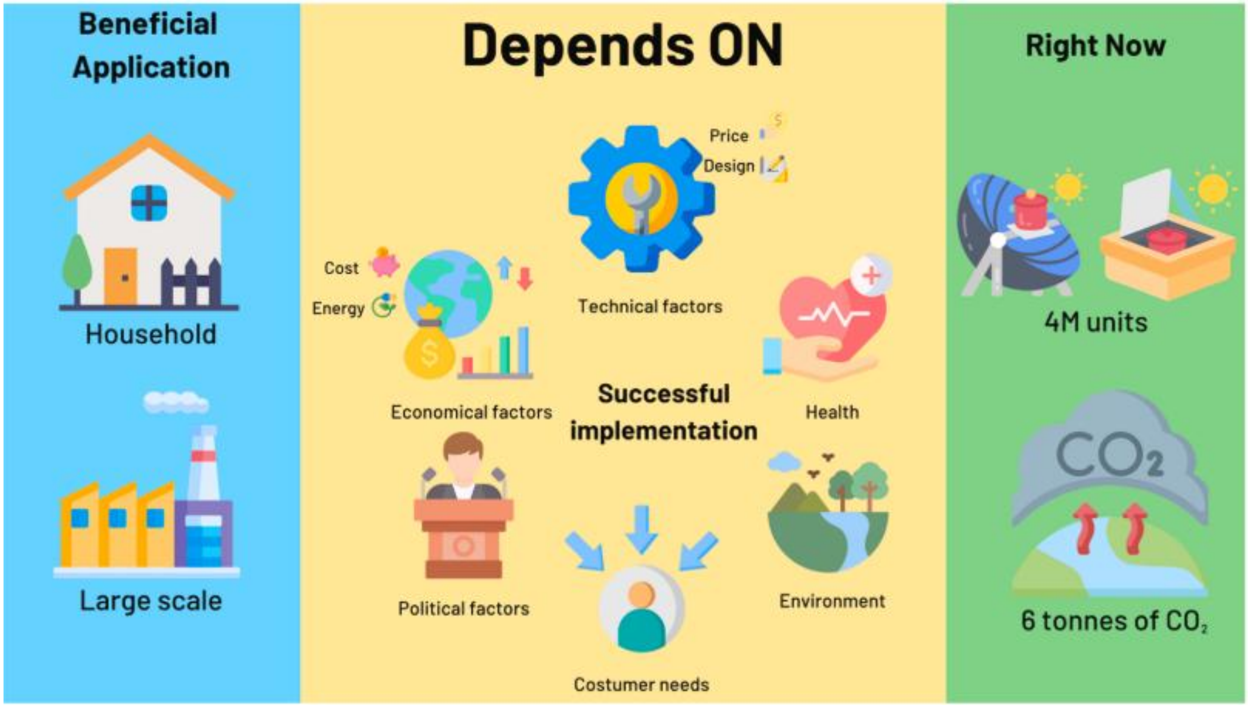

Fig. 2.1 The global impact of the solar cookers application [4]

Cooking can be categorized mainly as baking, roasting, broiling, boiling and frying depending on the applied temperature in the cooking process, the methods of the heat transfer (conduction, convection, or radiation), and the duration of the cooking process [9], [12]. Table 2.1 shows the different types of cooking and there description with the type of heat transfer mechanisms and their use [9].

Table 2.1 Different types of cooking and their type of heat transfer mechanisms [9]

Category	Description	Heat transfer mechanism	Uses
Baking	Food in oven with temperature range of 100 to 300 ℃	Convection (air), radiation (oven walls), conduction (pan)	Flour-based foods and fruits
Roasting	Food in oven with temperature range of 100 to 300 ℃	Convection (air), radiation (oven walls) and conduction (pan)	Meats and nuts
Broiling	Food in oven with temperature range up to 300 ℃	Primarily radiation (burner) with some convection (air) and conduction (pan)	Meats
Frying	Food submerged in hot oil (deep-frying) or cooked in a thin layer of fat (pan-frying)	Deep-frying, conduction (pan), convection (liquid) and Pan-frying conduction (pan)	Meats and vegetables
Stewing or boiling	Food cooked in boiling or simmering water	Conduction (pan) and convection (liquid)	Meats, vegetables, grains and pastas
Other cooking methods, such as microwave and radio frequency	Food in oven	Generate heat within the food by electromagnetic waves and molecular friction. Don't use a common heating method (conduction, convection or radiation)	Meat, rice and vegetables

Bread is used as a common food by human kind dates back to prehistoric period. Traditionally bread is prepared using baking oven powered by firewood, electricity and other sources. However, recent environmental challenges associated with the use of conventional energy sources have increased interest in solar baking systems as a means of mitigating environmental impacts [22]. Among the various solar cooking systems, solar baking can be considered a subcategory of solar cooking [23].

Bread baking is a fundamental food process where dough is converted into two different parts (crumb and crust) where both have distinct texture and porosity through a controlled application of heat and moisture. The effectiveness of the baking process is strongly influenced by several practical design parameters, among which oven temperature is critical; for most bread types, it typically ranges from 180 °C to 220 °C to ensure proper starch gelatinization, protein coagulation, and crust formation [24], [25]. Equally important is the baking time, which typically ranges from 20 to 40 minutes depending on dough size and temperature, as it governs the balance between crumb softness and crust browning [25], [26]. By controlling these and other parameters like air flow distribution and humidity of the baking air, the bread can achieve the desired texture, volume, flavor, and shelf life.

2.2 Classification of solar cooker

Solar cookers can be found in different types owning to their design and specific application. Solar cooking technologies can be classified based on the heat transfer mechanism to the cooking pot or vessel as a direct type and an indirect type solar cooker [27]. In direct type solar cooking, cooking energy is obtained directly from solar radiation during the cooking process within the solar cooker. Another classification of solar cookers is based on the manner in which solar radiation is concentrated or focused onto the cooking pot or vessel. In this classification there are three groups, the first is group that includes solar cookers that focus solar radiation on the top and the sides of the cooking vessel. In this group solar box cookers, panel cooker and funnel cookers are included. In the second group, solar cookers that focus solar radiation on the bottom of the cooking vessel are included. This category comprises parabolic, Fresnel, and trough-type concentrators. The third group includes all indirect cooker, where the heat is collected outside the oven and transferred to the cooking vessel by the heat transfer fluids [28]. Fig.2.2 shows different types of solar cooking systems.

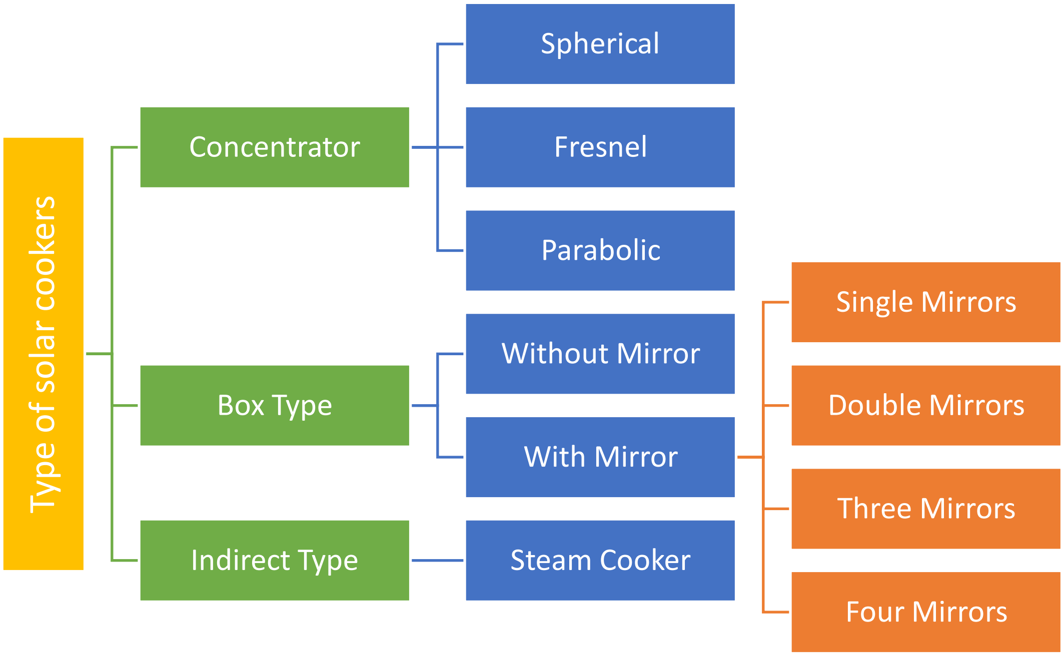

Fig. 2.2 Different types of solar cookers

2.2.1 Direct solar cookers

Direct solar cookers are systems in which solar radiation is concentrated and applied directly to the cooking vessel without the use of intermediate heat transfer fluids or separate collectors. Common designs in this category include box-type and panel-type solar cookers, as well as concentrating cookers that employ parabolic dishes, Scheffler reflectors, compound parabolic concentrators, and hybrid box-type configurations. Performance results from the literature show that direct systems can reach absorber temperatures of 165 to 180 ℃ [29], [30]. Scheffler ovens have demonstrated the ability to bake 32 loaves in 85 to 110 minutes [22], while hybrid box-parabolic ovens achieved absorber temperatures of 121℃ [31]. Box-type and panel-type solar cookers, together with parabolic solar cookers, are classified as direct-type solar cookers [27]. The Box type solar cooker is the most researched and advanced type of solar cooking method with different modifications as shown in the Fig.2.3 [32].

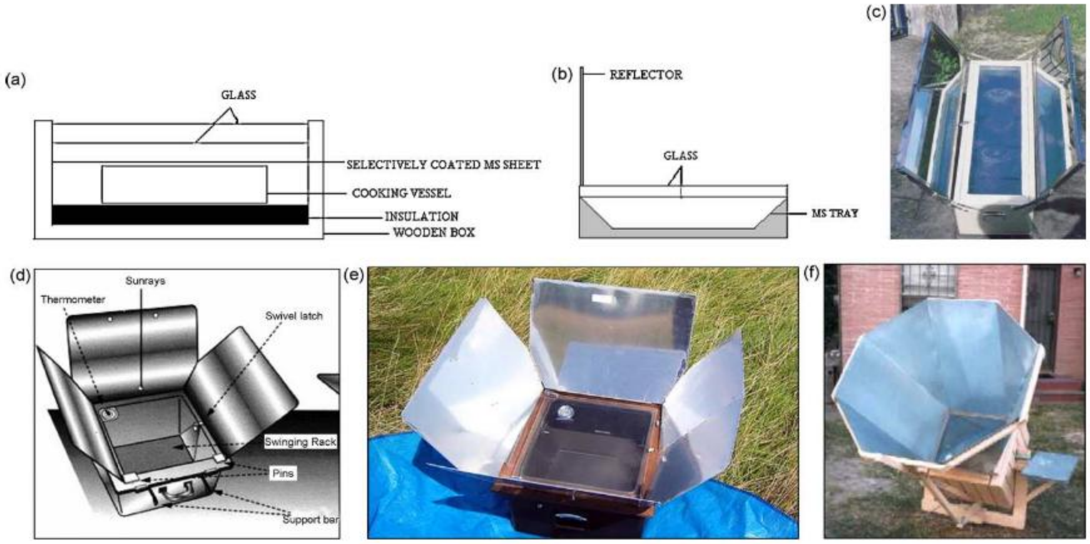

Fig. 2.3 Different types and modification of solar box cookers Box type cooker: (a) without reflector and (b to f) with single, two, three, four and eight reflectors [32]

The box and panel type solar cookers are classified under low temperature cooker where the maximum stagnation temperature can range between around 80℃ to 120℃ and used for slow cooking and in small scale applications [22], [23]. Box-type solar cookers are non-concentrating, direct-type solar cookers that operate based on the greenhouse effect. Solar radiation passes through a transparent glazing, typically single or double glass, and is absorbed by blackened interior surfaces and the cooking vessel. The generated heat is retained within the cooker by minimizing convective and radiative heat losses (Fig.2.4) [11].

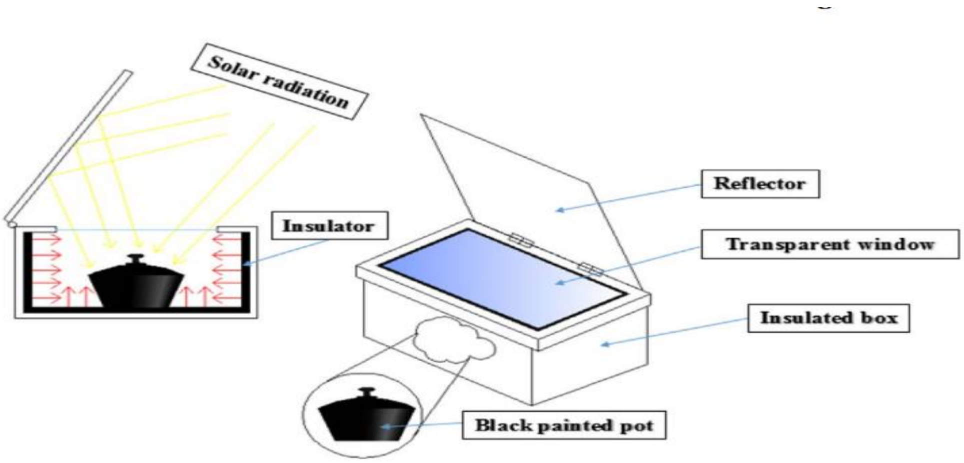

Fig. 2.4 Solar box cooker with reflector and insulated box cover with transparent cover [11]

Panel solar cookers are hybrid of box and parabolic solar cooker designs and it is simple and portable (Fig.2.5). However, they are in the low temperature solar cooker group and different studies have improved the design to increase their performance by adding various reflector configurations [33].

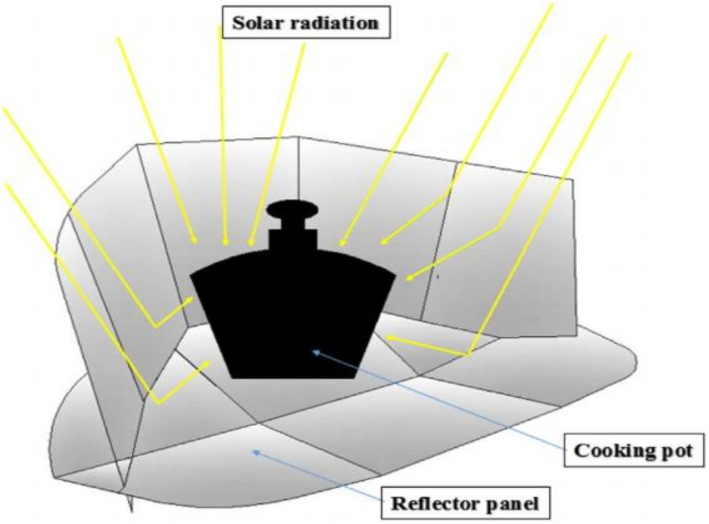

Fig. 2.5 Solar panel cooker with cooking pot and reflector [11]

Over the years, several improvements have been introduced, including better insulation materials, selective absorber coatings, and auxiliary reflectors to increase operating temperature and cooking time. These enhancements have enabled box-type and panel-type solar cookers temperature to increase and reduce the cooking time. Table 2.2 shows different types of solar cooker with their performance indicators.

Table 2.2 Comparison of different solar cooker [28]

Type	**Max Temp (°C)**	**Efficiency (%)**	**Cooking Time**	**Cost (USD)**	**Best use**
Box with one reflector	130 to 140	Around 77	60 to 90 min	Around 60	Households, slow cooking
Panel (COOKIT)	90 to 110	Around 67	60 to 90 min	1 to20	Low-income, emergency relief
Funnel	Around 90 to 150	Not specified	30 to 90 min	<50	Community
Parabolic	>250	Around 31.5	30 to 40 min	270 to 700	Restaurants, fast cooking, frying
Indirect (PV)	PV capacity 200 to 300 W	System-dependent	Any time	Around 240	Indoor, night cooking
Commercial	>250 (steam)	Varies	30 to 60 min	>1000	Institutions, mass feeding

In the study conducted by Silva et al.[33], a novel solar box type solar oven was designed and its thermal performance was evaluated experimentally to address the lower thermal efficiency and heat retention of solar box cooker for sustainable cooking (Fig.2.6). The solar box cooker was integrated with a steel plate as thermal mass and rock-wool insulation, and equipped with an inclined double-glazing cover. Its performance was experimentally evaluated using four food types: rice, cake, vegetables, and bread. The results of their study showed that the box-type solar oven achieved internal temperatures exceeding 160 °C, with a maximum recorded temperature of 180 °C. The maximum thermal efficiency of the box-type solar oven was found to be 38%, showing an improvement of approximately 25 to 30% compared to a conventional box-type solar cooker. The result from the cooking test of the improved solar box type oven showed that a total cooking time of 90 min, 120 min, 60 min and 110 min for the rice, cake, vegetables, and bread respectively.

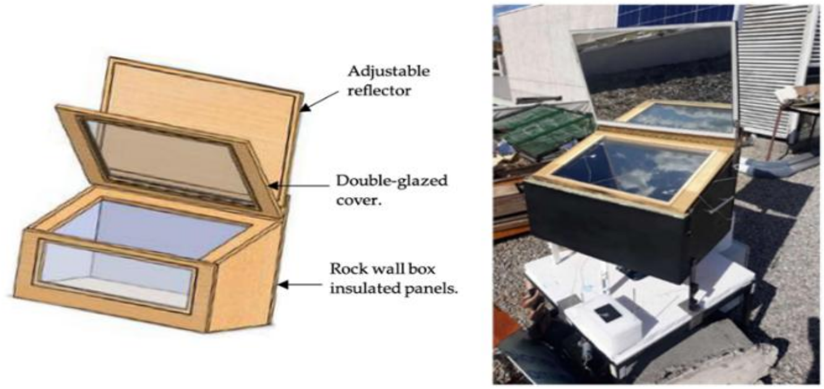

Fig. 2.6 Novel Box-type solar oven [33]

Mekonnen and Kebede [31] developed and experimentally evaluated solar baking oven integrated with a parabolic reflector to improve the conventional box-type solar cooker performance under Bahir Dar weather conditions (Fig.2.7). The outer body of the box-type solar baking oven was constructed from plywood and covered with a glass glazing having a transmittance of 0.9, while a flat mirror reflector was employed as a booster to enhance solar radiation capture. The parabolic trough reflector was built from aluminum with a focal length of 0.104 m, depth of 0.500 m and diameter of 0.150 m. The absorber pipe, coated with black paint to achieve an absorptivity of 0.9, was used together with an aluminum baking tray and a stainless-steel baking chamber. The backing tray was placed in their design at the focal line of the parabolic trough reflector with a rectangular shape and its capacity was 15 breads per cycle with a bread size of 11 ×10 × 8 cm each. The result of their study indicated a maximum absorber pipe temperature of 121.1 ℃, with a first figure of merit F_1 of 0.12 and a standard stagnation temperature of 102.3℃. The total baking time was 50 minutes, representing a reduction compared to a conventional box-type solar oven. The system was capable of baking up to 60 loaves per day in three cycles; however, its capacity was limited for larger batch baking.

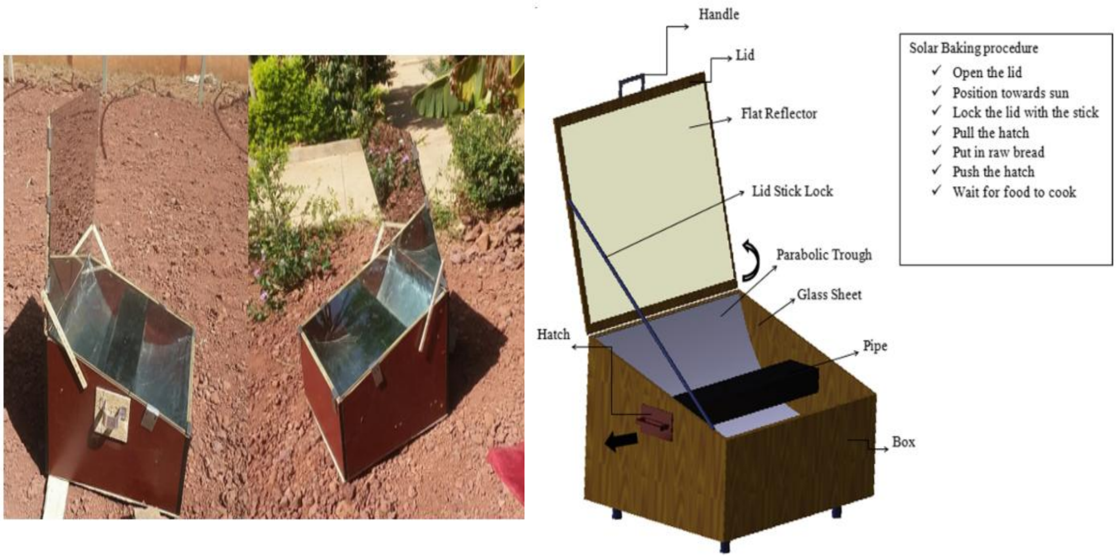

Solar Baking procedure
- ✓ Open the lid
- ✓ Position towards sun
- ✓ Lock the lid with the stick
- ✓ Pull the hatch
- ✓ Put in raw bread
- ✓ Push the hatch
- ✓ Wait for food to cook

Fig. 2.7 Box type solar baking oven integrated with a parabolic reflector [31]

Moreover, a novel building-integrated box-type solar cooker incorporating a fixed asymmetric compound parabolic concentrator (CPC) booster reflector was designed and experimentally tested to enhance stationary cooker performance and enable indoor use without the need for solar tracking, as reported by Harmim et al. [30] (Fig.2.8). It was built from an insulated box of $0.434\,m^2$ aperture area with double glazing cover and stainless-steel absorber plate in a step-shape with absorptivity of 0.95. The CPC reflectors was integrated at the top and bottom of the box-type solar cooker made from a small rectangular mirror mounted on wooden frames with aperture area $0.712\,m^2$ and focal distance of 0.235m and 0.3m for the upper and bottom reflectors respectively with concentration ratio of 2. The study reported first and second figures of merit of 0.152 and 0.470, respectively, along with a standardized cooking power of 78.9 W. The maximum absorber temperature of the box type solar cooker was found to be 166 ℃ and 127.7 ℃ with and without CPC reflectors respectively. Using this design, the cooking time was 2 h 55 min for 0.6 kg of bread and 2 h 30 min for 0.4 kg of bread, with a production capacity of two baking cycles per day. Their results demonstrate an improvement in efficiency due to the building-integrated design; however, both the cooking time and production capacity require further enhancement.

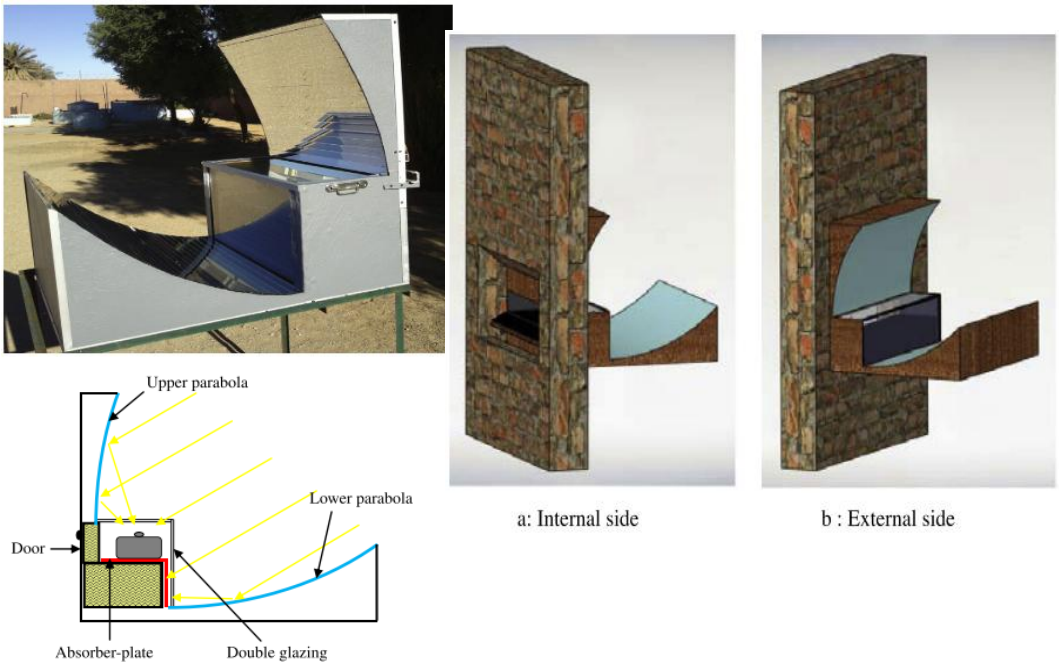

a: Internal side

b : External side

Fig. 2.8 non-tracking box-type solar cooker integrated with CPC as booster-reflector with step absorber (lift-side) and integrated into building (right-side) [30]

Concentrating cookers are designed to focus solar radiation onto the bottom surface of the cooking vessel or onto a separate collector, which then transfers the heat to the cooking vessel (Fig.2.9) [11]. Under concentrating cookers, parabolic solar cookers and solar cookers created by planer mirrors, reflective foils or lenses are included [28] and can be used in baking, cooking and frying application [34]. Direct concentrator solar cookers, including parabolic dishes and Scheffler reflectors, focus solar radiation directly onto the cooking vessel. Parabolic dishes typically achieve thermal efficiencies of 40–62% and provide cooking powers ranging from 400 to 600 W, enabling baking, frying, and roasting at temperatures above 200 °C. Scheffler reflectors, with their fixed-focus geometry, attain efficiencies of 26–57% and cooking powers of 300–500 W, while also allowing indoor cooking through the use of secondary reflectors [12].

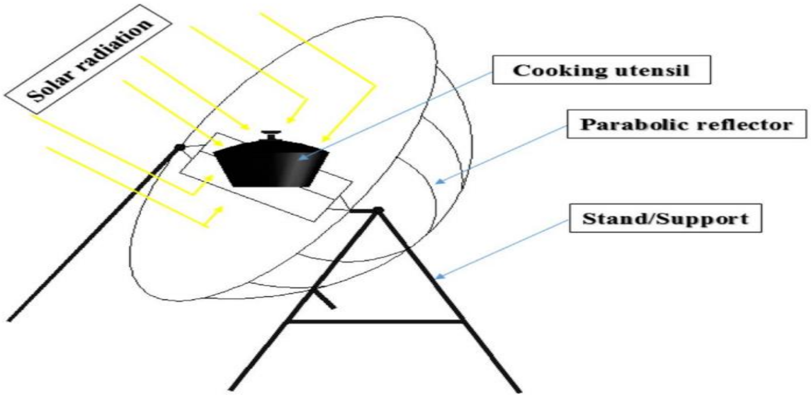

Fig. 2.9 Solar concentrator cooker [11]

Gallagher [29] investigated the performance of a solar fryer constructed from quasi-parabolic, flat, hexagonal segments made of aluminized polyester, designed to distribute the focus onto the bottom of the pan for injera baking (Fig.2.10). The experimental results demonstrated an average heating power of 640 W with an optical efficiency of 60 %, enabling the baking of 4 kg of injera per hour. The pan reached a cooking temperature of approximately 180 ℃ within the first 20 minutes. However, the design required preheating between baking cycles.

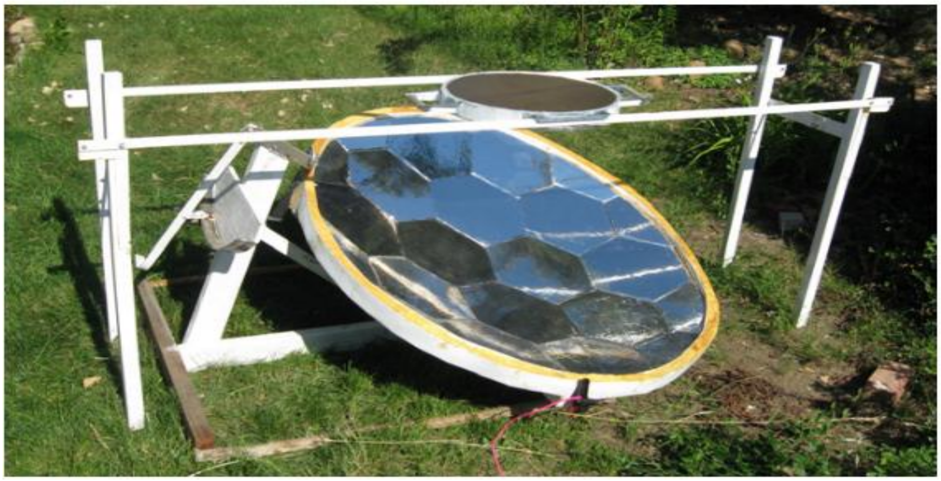

Fig. 2.10 Solar injera fryer setup [29]

In a related study, a novel dual-purpose direct-type parabolic solar oven was investigated for baking bread, aiming to optimize baking quality and reduce reliance on fossil fuels and firewood Farimani et al. [35] (Fig.2.11). The study employed laboratory optimization using an electric heat source to simulate solar flux, followed by experimental validation under real solar radiation conditions. The solar oven was constructed with a chrome-plated plastic parabolic reflector, a cast iron absorber plate, a blackened aluminum top plate, and a vacuum-insulated baking chamber with fiberglass insulation. The results indicated that an optimum baking chamber height of 2 cm, with a container temperature of 210 ℃ and an incoming flux of 60 W at the top, produced bread in 7 minutes for a 70 g dough. The overall efficiency of the solar oven was found to be 44 %, with a cooking power per unit area of 4269 W/m². Furthermore, a baking temperature of 210 ℃ was shown to yield superior bread quality compared to 150 ℃ and 180 ℃.

Fig. 2.11 Solar baking oven [35]

Furthermore, a tube-type direct solar oven was developed and experimentally evaluated to provide a low-cost, locally manufacturable solution for bread baking under Addis Ababa weather conditions (Aragaw and Adem [36]) (Fig.2.12). The focal geometry was determined using SOLTRACE ray-tracing simulations, and the baking process was modeled with COMSOL thermal simulations. These results were further validated through experimental tests, including no-load, water-boiling, and bread-baking experiments. The oven materials included a cylindrical aluminum receiver (0.1 m×1 m, painted black), a transparent acrylic airtight cover (140 mm×140 mm), a parabolic aluminum reflector (1.15 m×1 m), and a sliding aluminum tray with rubber-sealed door. Their study result showed a stagnation temperature of 127 ℃ was reached in 67 min, a first figure of merit F_1 equal to 0.32, and overall thermal efficiencies of 43.9%, 42.1%, and 38.3% under average solar irradiance of 305, 259, and 232 W/m^2, respectively. Bread baking tests demonstrated a utilization efficiency of 35% at an average solar irradiance of 396 W/m², with a heating time of 51 minutes required to raise the temperature of

1 kg of bread from 25.1 °C to 88.6 °C. When comparing the experimental results with the simulation, there was a 16-minute difference in baking time. The simulation under predicted the baking time due to limitations in the prototype construction, particularly the inability to achieve an airtight seal. Their finding showed that the airtight cover significantly reduced convective losses, improving performance compared to other direct solar cookers.

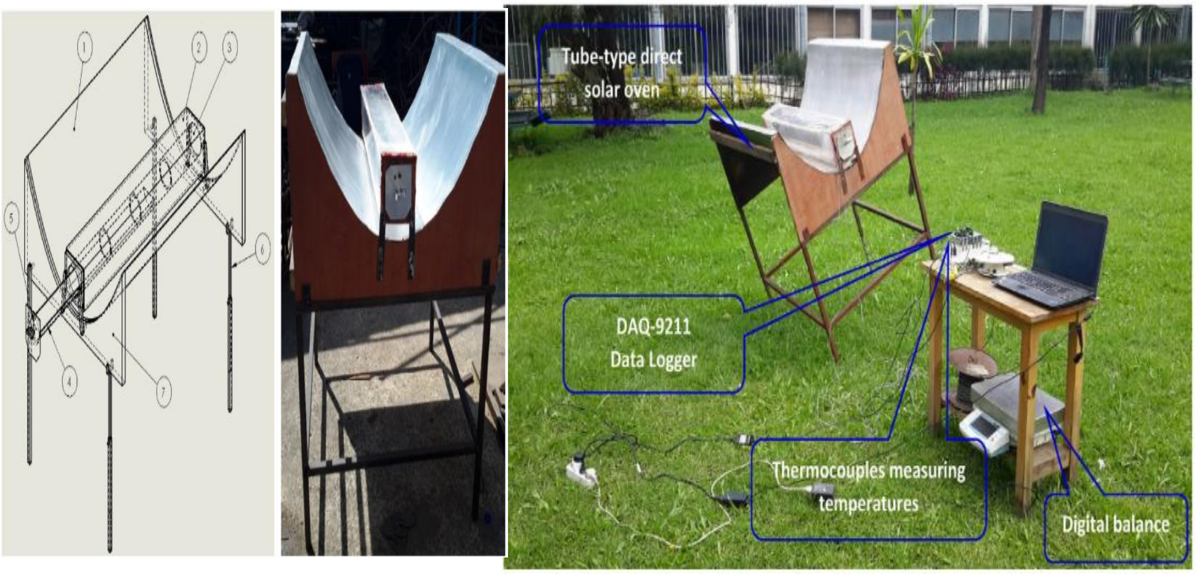

Fig. 2.12 Tube type direct solar oven bread baking system [36]

In another study, Nazari et al.[37] Designed and tested a domestic solar bread cooker equipped with a parabolic concentrator, with the objective of improving bread baking performance and predicting the required cooking plate temperature using artificial intelligence hybrid models (Fig.2.13). The system was constructed with a galvanized steel parabolic concentrator of 1.30 m diameter, exhibiting a reflectivity between 0.9 and 0.95. The cooking plate, made from 6 mm aluminum with an absorptivity of 0.8–0.9, was insulated on the top and enclosed on the sides with galvanized steel. The results of the study showed that the cooking plate reached 180 °C within 20–25 minutes, enabling the system to bake 12 breads per hour, each weighing 0.2 kg with a diameter of 45 cm.

Fig. 2.13 Parabolic concentrator solar bread cooker [37]

2.2.2 Indirect solar cookers

Indirect solar cookers differ from the direct solar cooker in that they use a heat transfer medium including steam, thermal oil, and air to carry energy from the solar concentrator to the cooking chamber. This separation between the solar receiver and the cooking vessel helps to control the cooking process, improves the safety of the operation, and the facilities thermal energy storage integration. Indirect systems are based on Linear Fresnel Reflectors (LFRs), parabolic troughs, or evacuated tube collectors. And they are applied in medium and large capacity solar cooking. Steam based injera baking system achieved stove temperatures between 135 to 160 ℃ with dish stagnation temperatures up to 255 ℃ [38]. Applications of indirect systems extend to community kitchens, schools, and institutional bakeries, where medium to large batch cooking is required.

Chaudhary et al. [39] developed and experimentally evaluated a twin vessel solar cook stove (TWSCS) for simultaneous cooking of two different food items using evacuated tube solar collectors integrated with aluminum reflecting sheet (Fig.2.14). Their designed system composed of 40 evacuated tubes with a 1.5 m length and diameter of 0.037 to 0.047 m connected to a header and circulating Hytherm-500 heat transfer fluid through the two cooking vessels. Under the evacuated tube solar collectors, aluminum reflecting sheet are integrated to enhance solar radiation absorption. The cooking vessel one is vapor-tight stainless steel pressure cooker and cooking vessel two is welded closed vessel with vapor vent. Both vessels had upper cooking units and lower HTF passage units with a baffle, insulated with glass wool and enclosed in galvanized iron or wood. The results from their study indicated that the temperature of the heat transfer fluid entering cooking vessel one ranged from 90 °C to 132 °C, while for cooking vessel two, it ranged from 76 °C to 127 °C. The instantaneous heat transfer fluid energy input for cooking vessel one was found to be between 201 to 296 kJ and for cooking vessel two was between 231 to 387 kJ. The thermal efficiency of the twin-vessel solar cook stove ranged from 11.8% to 78.6%, with the maximum efficiency observed at the beginning of the cooking process and the minimum at the end. The cooking time for the cooking vessel one with 3 liters of mixture of rice and water temperature of 104 °C was found to be 170 min and cooking vessel two with 2.5 liters of kadhi and khoa temperature of the 99 °C were found to be 190 and 470 min respectively. However, the system requires improvements in cooking time and scalability to accommodate higher-capacity loading.

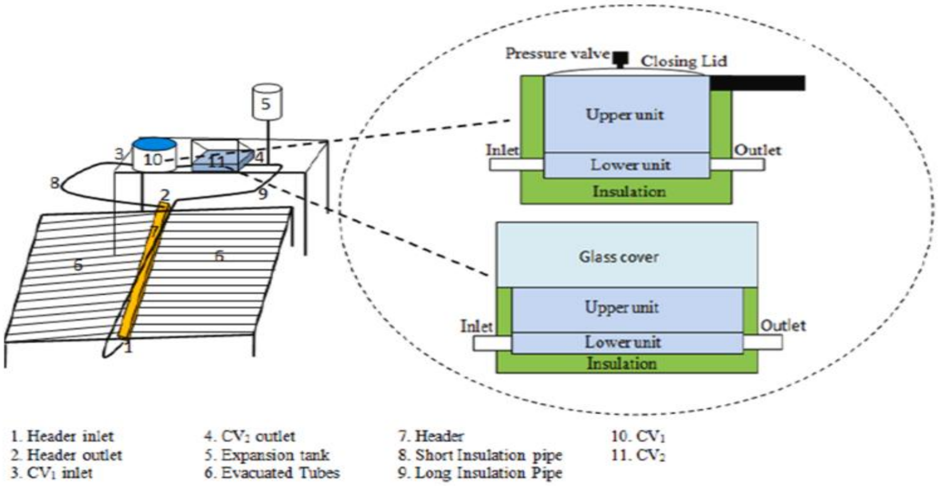

Fig. 2.14 Schematic diagram of the twin vessel solar cooking system (TWSCS) [39]

For community-scale baking applications, the thermal performance of Scheffler parabolic solar ovens was investigated and compared with conventional parabolic solar cookers, using experimental tests and numerical modeling, as reported in the study by Ouqazzamar et al. [22] (Fig.2.15). The solar oven was capable of loading a total of 32 breads, with a combined weight of 15 kg, distributed over two trays, each bread measuring 5 cm in thickness and 16 cm in diameter. The materials and configurations included Scheffler-type reflectors with aperture areas of 3.914 m^2 and 5.324 m^2 and a baking chamber with two trays. The performance analysis results showed a first figure of merit (F_1) of 0.30 and a second figure of merit (F_2) of 0.85, with a corresponding cooking power of 434 W. The optical efficiency of the Scheffler parabolic solar oven was found to be 0.899. Their results showed that the Scheffler cooker outperformed conventional parabolic dishes, achieving faster cooking times and higher efficiency. Solar baking tests indicated that with a Scheffler reflector area of 2.83 m^2 for 15 kg of bread, the cooking time was 110 min, whereas increasing the reflector area to 3.75 m^2 reduced the cooking time to 85 min. Validation of the simulation model demonstrated that it could accurately predict the experimental temperature results, with an average absolute relative error of 3 %.

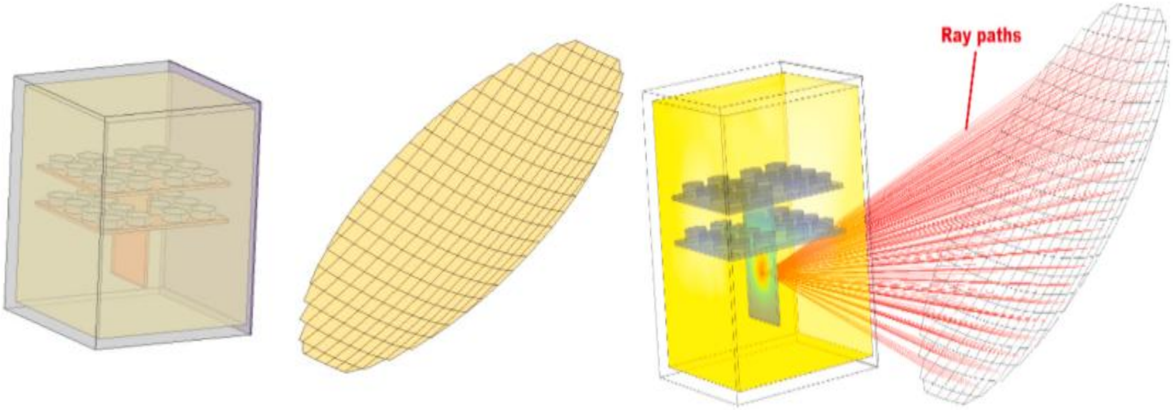

Fig. 2.15 Simulated solar oven geometry [22]

To address solar intermittency and enhance baking performance, the integration of a metal hydride–based thermal energy storage (MH-TES) reactor with a solar bakery unit was investigated using COMSOL simulations by Ayub et al. (Fig 2.16). Their system included a 10 m^2 Scheffler parabolic concentrator and a baking chamber integrated with high-temperature metal hydride (HTMH) thermal energy storage featuring annular truncated hollow conical fins. The integration of the MH-TES improved the solar bakery unit's energy efficiency from 6% to 42.89%, enabling continuous baking even at night or under cloudy conditions, with a maximum energy output of 1560 W and an exergy output of 174 W.

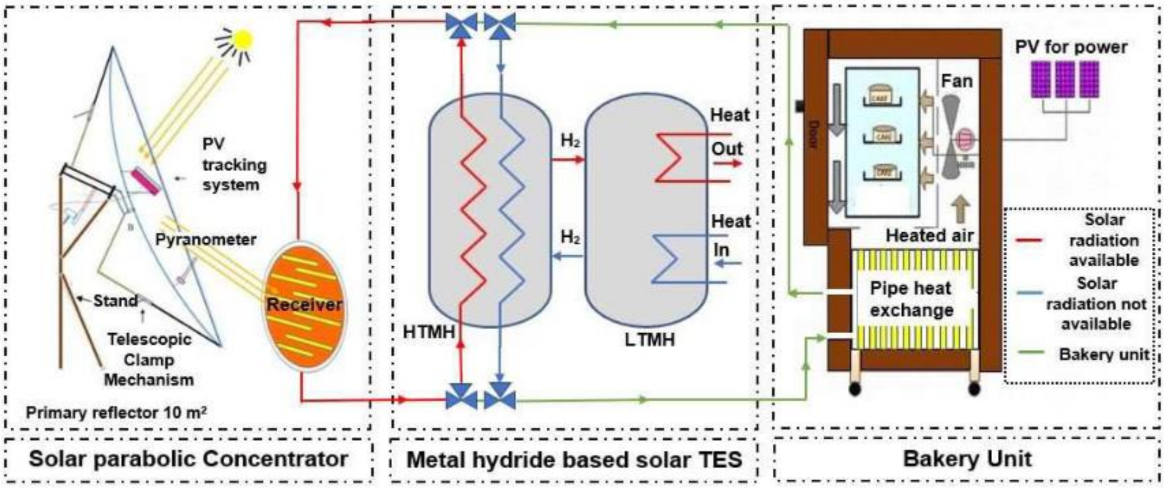

Fig. 2.16 the novel solar bakery unit using metal hydride based thermal energy storage system [51]

In an effort to replace conventional electric baking systems, a solar-powered baking oven integrated with evacuated tube solar collectors was experimentally evaluated for its performance by Forsythe and Madyira [40] (Fig.2.17). The solar oven was constructed from stainless-steel sheets with rock-wool insulation sandwiched between the layers, covered by a double layer of fiberglass, and equipped with an inlet fan to facilitate air circulation. The result showed that a baking temperature between 200 to 250 °C with inlet air velocity of 1.8 m/s. The power required to bake 400 g (3 loaves) of bread was found to be 2.182 kW and baking time of 40 min with efficiency of 0.72 using 28 evacuated tube collectors. By integrating the compound parabolic concentrators, the efficiency increased to 78% and the total required evacuated tube collector reduced to 25.

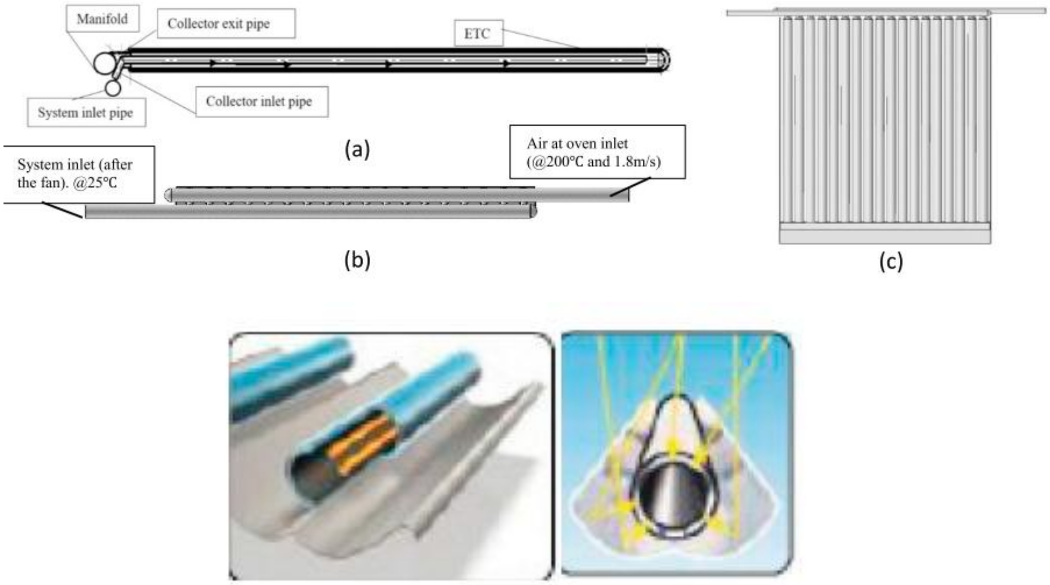

Fig. 2.17 Solare oven integrated with evacuated tube solar collectors and compound parabolic concentrators (ETCs-CPC) [40]

Ayub et al.[41] They designed and evaluated a decentralized solar bakery unit employing Scheffler reflector technology to reduce reliance on conventional fuels. Using the computational fluid dynamics (CFD) simulation tool ANSYS FLUENT, the airflow distribution within the baking chamber was modeled (Fig.2.18). The solar baking unit was built from stainless steel baking chamber which contains three perforated trays and insulated with rock wool insulation. The bottom of the baking chamber contains a secondary reflector integrated with a zigzag absorber plate covered with a transparent glass and solar powered fan for air circulation inside the backing chamber. The fixed focus Scheffler reflector aperture area was 10 m^2 with concentration ration of 100. The results from their study showed that the receiver temperature ranged between 300 and 400 ℃, with an available solar power at the receiver of 3.46 kW and an average receiver efficiency of 63%. The air temperature at the baking chamber inlet was found to be between 200 to 230 ℃ and the energy supplied to the baking chamber was 3.29 kW and energy utilization ratio of the baking chamber was 45%. The average air velocity inside the baking chamber was found to be around 0.5 m/s and the air flow distribution inside the backing chamber was relatively uniform which favors the backing process. The temperature of the air over the backing trays was found to be around 180 ℃ and total baking time of the cake was found to be 35 min. In a related study by the same authors [42], using the same Scheffler-based system, the results showed a total baking time of 35 minutes. The integration of a secondary reflector significantly improved the receiver efficiency, increasing it from 37 % to 65 %. The study reported exergy losses ranging from 0.19 to 1.08 kW, exergy efficiency between 6.62 % and 56.46 %, and an overall system exergy efficiency of 59.26 %.

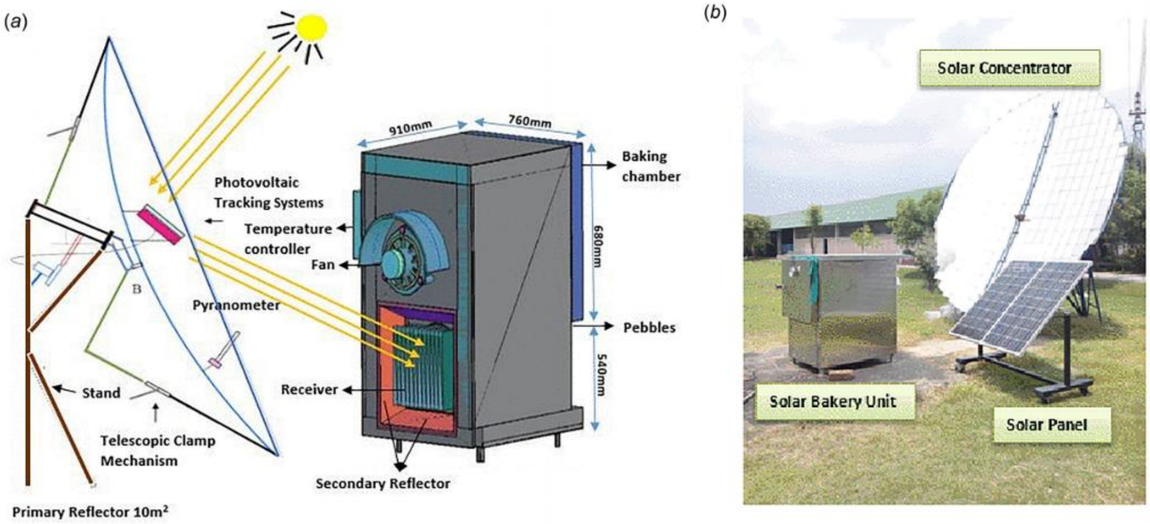

Fig. 2.18 Scheffler reflector Solar baking system [41]&[42]

A steam-based solar thermal Injera baking system using a parabolic dish concentrator for high-temperature indoor baking, achieving improved efficiency as an alternative to conventional biomass stoves in Ethiopia was studied by Tesfaye et al. [38] (Fig.2.19). The manually tracked dish has an aperture area of 2.54 m^2 and a concentration ratio of 325 with insulated stainless-steel pipe and heat exchanger installed to deliver steam at 250 °C to stove. Their study reported a stagnation temperature of 255 °C, with the baking pan temperature varying between 135 and 160 °C, and a baking energy consumption of 0.1 kWh per Injera. The baking time for a single Injera was found to be 2 min and 30 sec. The heat loos at different location were found to be 304 W at a receiver, 270 W at the stove and 95 W through the pipeline. However, the baking temperature was found to be lower than the convention baking temperature of 180 to 220°C.

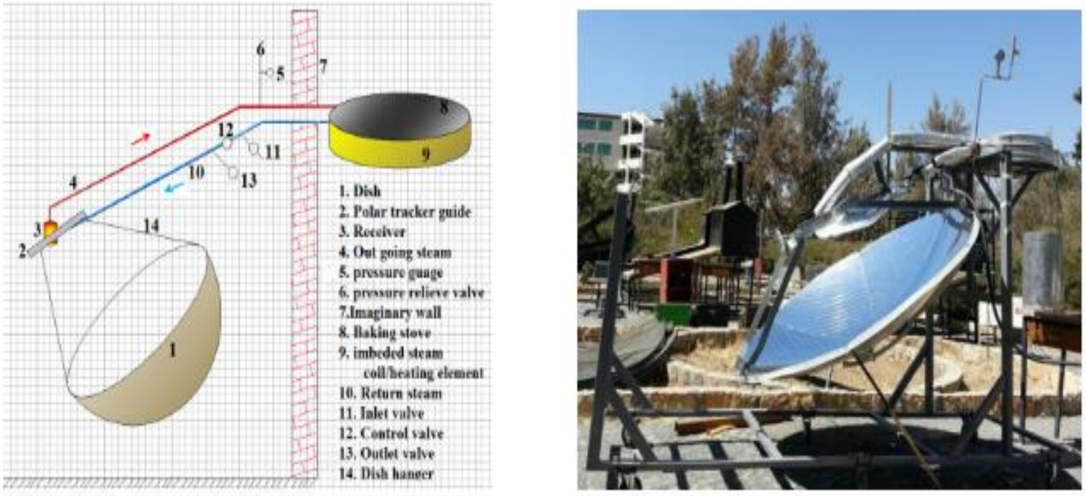

Fig. 2.19 Parabolic dish concentrator using indirect solar Injera stove [38]

On the other hand, a parabolic trough solar thermal Injera baking system was designed and evaluated for producing 11,000 Injera, using Computational Fluid Dynamics (CFD) simulations in ANSYS Fluent and optical analysis with Soltrace, aiming to replace conventional electric Mitads, as reported by Retta et al. [43] (Fig.2.20). The solar parabolic trough collector integrated with cylindrical oil chamber under each 92 Mitads and phase changing thermal storage unit. The receiver length was set to be 100 m with 0.21 diameter and a parabolic trough length was 100 m with aperture width of 5.763 m and depth of 1.2m. The aperture area of the parabolic trough was 532.9 m^2 and the focal length was calculated to be 1.7 m with concentration ratio of 16.03. The Soltrace was used to evaluate the heat flux distribution on the receiver plates and ANSYS fluent was used to evaluate the temperature distribution through the baking plate. The result showed that the system delivered 2.11 kW energy for each Mitad with a total system energy consumption of 1216.5 MJ/h and thermal efficiency of 57 %. The baking plate temperature was found to be between 130 to150 ℃ with total baking time of 3 min. The initial time taken to reach the baking temperature of 130 ℃ was reported to be 30 min and for the consecutive cycle it takes 1 min in each round of baking to get to this temperature. The result from the temperature over the plate was found to be in the acceptable range for Injera baking and their design showed that the system can provide 11,000 Injera in 6 hours.

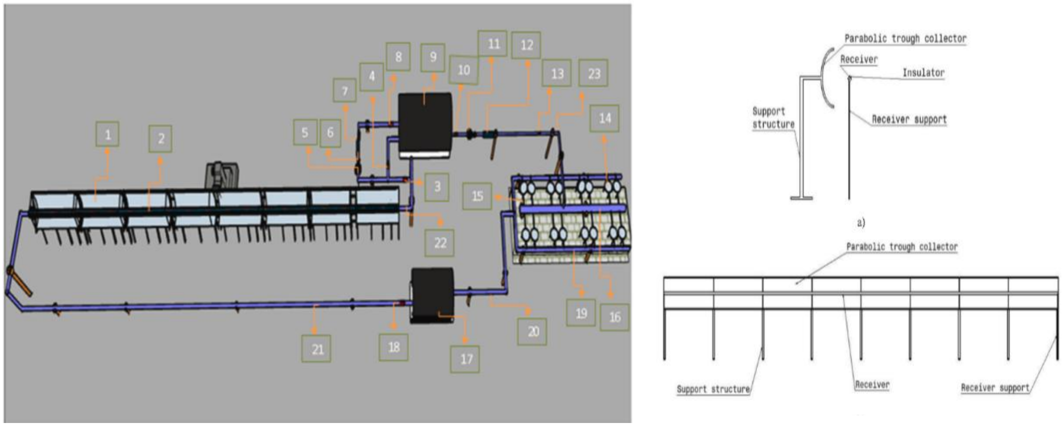

Fig. 2.20 solar Injera baking system [43]

Using SolTrace and ANSYS modeling tools, the optical, thermal, and economic performance of a Linear Fresnel Collector (LFC) mirror field coupled with a multi-tube trapezoidal cavity receiver was optimized through simulation-based analysis, as studied by Moghimi et al. [44] (Fig.2.21). In their modeling they used LK scripting in SolTrace to evaluate the optical performance using 1 million rays and used the result in ANSYS to optimize the system. There result showed that an increase in mirror rows above 22 reduced the thermal efficiency due to shading however the economic optimization showed that using 30 rows will reduce the cost. Also increasing the receiver height improves the optical efficiency but increase the installation cost. The thermal model resulat showed that the heat loss through radiation was significant inside the receiver, however, the study did not experimental validated their result.

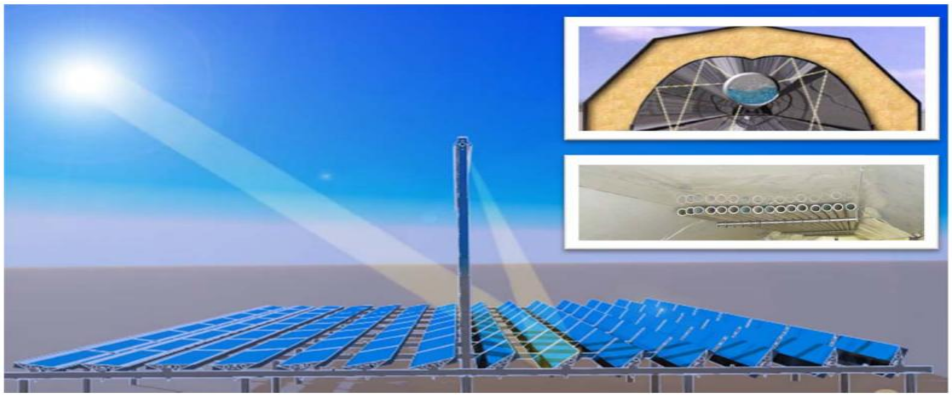

Fig. 2.21 Linear Fresnel collectors with the cavity receiver [44]

Rungasamy et al. [45] conducted a comparative optical and thermal performance evaluation of different receivers for etendue-conserving compact linear Fresnel reflector field to identify the best receiver design using SolTrace Monte Carlo Ray Tracing (MCRT) simulations for optical modeling and ANSYS for thermal modeling of heat loss simulation in four different receiver configuration (Fig.2.22). There result showed that the adapted tailored edge ray concentrator (TERC) monotube receiver achieved the highest optical efficiency of 56.93% however the thermal loss of this receiver was found to be higher than all the other recovers. Whereas the compound parabolic concentrator monotube receiver has a lower optical efficiency of 51.29% compared to the other three recovers however, its thermal loss was found to be the least. Also, an increase in a receiver cover glass was found to increase the heat loss from the chamber. The experimental result was found to be comparable with the simulation result with max temperature difference error of 3.35%.

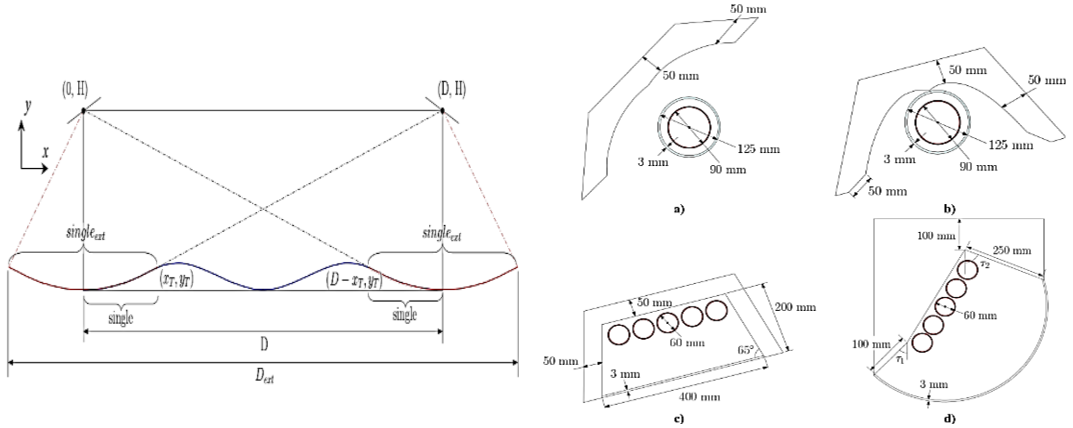

Fig. 2.22 Linear Fresnel field showing only two receiver target point (left-side) and single and multi-tube receiver (right-side) [45]

A study was conducted to evaluate the optical performance of several Linear Fresnel Collector (LFC) configurations, aiming to maximize useful energy output and minimize shading and blocking effects, according to Montes et al. [46] (Fig.2.23). They used Matlab for ray tracing and validated their result with the SolTrace to evaluate annual performance of central LFC and compact LFC design using hourly solar data at different receiver height of between 8 to 12 m and mirror field width of between 16 to 26 m. Their results showed that a wider mirror field combined with an elevated receiver distance led to higher annual energy efficiency due to reduced blockage losses. In contrast, optical efficiency was maximized with a narrower mirror field paired with an elevated receiver. In SolTrace, 100,000 rays were simulated and validated against solar noon results obtained from MATLAB. The study showed optical efficiencies of 60.67% and 60.71% for SolTrace and MATLAB, respectively.

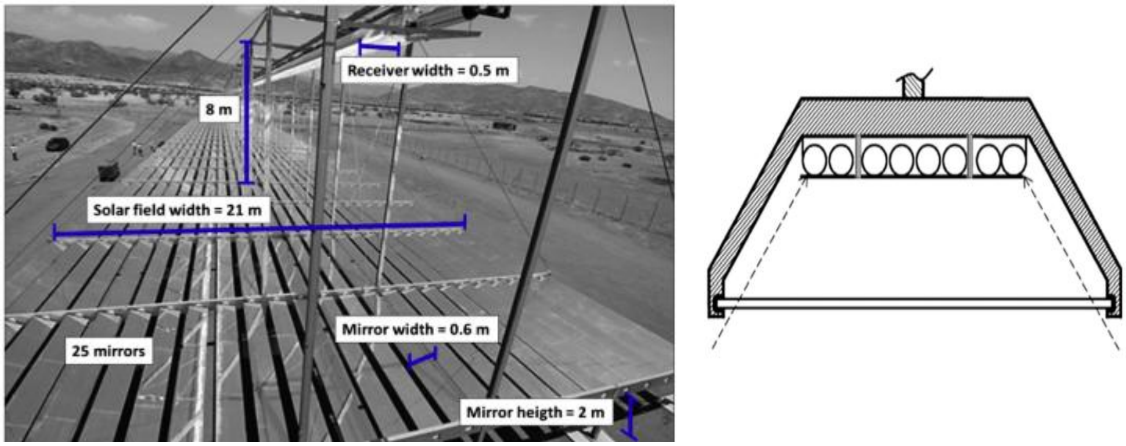

Fig. 2.23 Linear Fresnel collectors with a multi-tube receiver [46]

Furthermore, Kincaid et al. [47] conducted a comparative optical performance study on three major CSP technologies namely linear Fresnel (LF), parabolic trough (PT), and central receiver (CR) and evaluated annual optical efficiency and incidence angle sensitivity (Fig.2.24). They employed the SolTrace ray-tracing tool to model sun shape distributions, optical errors, and incidence angle modifiers. The results indicated that the annual optical efficiencies for the parabolic trough, central receiver, and linear Fresnel were 60%, 52%, and 40%, respectively. The metric levelized cost of heat (LCOH) for linear Fresnel collector was found to be 2.7 cents per kWh_{th} with total collector cost of 175 \$ /m^2 whereas for parabolic trough collector with a same LCOH will have an installed cost of 262 \$/m^2. The selection of a linear Fresnel collector can be a trade off between cost and loss in optical efficiency. Their study found that the application of linear Fresnel collector can result the lowest cost due to its structural simplicity and has a potential to replace the natural gas process heating in California market.

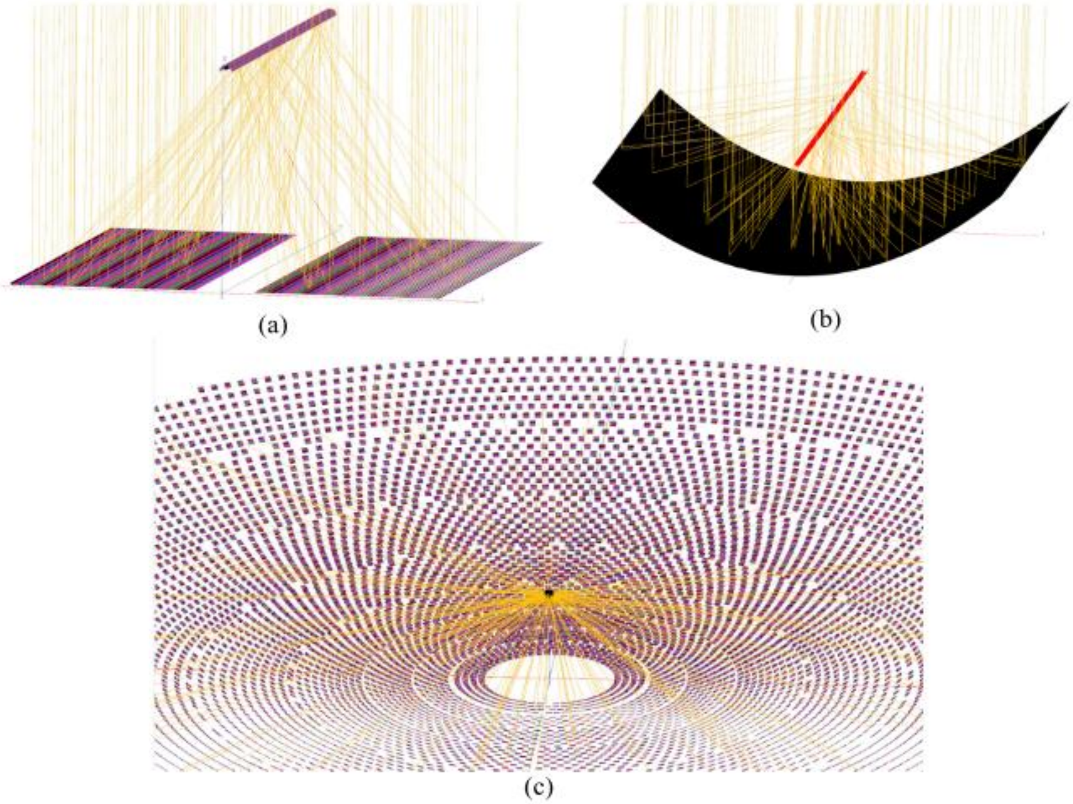

Fig. 2.24 (a) Linear Fresnel (LF), (b) parabolic trough (PT) and (c) central receiver (CR)

Moreover, Said et al. [48] assessed the optical performance of a Linear Fresnel Reflector (LFR) designed as a solar water heater at the University of Blida, Algeria (Fig.2.25). The system was developed using a flat mirror of a size 1.5 m length and 0.1m width with a total of 11 flat mirrors having effective area 1.65m^2. The trapezoidal receiver cavity integrated with four copper absorber tubes of 22mm diameter and 1.6m length with a secondary reflector. They used MATLAB to simulate their system and validated with SolTrace result for flux distribution on the receiver tubes. The result from there study showed a concentration ratio of 6.74 for 7 mirrors, 8.6 for 9 mirrors and 9.77 for 11 mirrors. The thermal efficiency also shows an increase with the number of mirrors and it was found to be 29.13 % for 11 mirrors, 27.13% for 9 mirrors and 20.7% for 7 mirrors. The optical efficiency was found to be between 26.98 to 42.65% and average intercept factor of 0.936 to 0.972. Also, increasing the number of mirrors can increase the concentration ratio, optical efficiency and thermal efficiency of the system, however this is only true up to an optimum number of mirrors because the effect of shading and blockage can counteract it advantage. The result from SolTrace showed a comparable result with the MATLAB simulation result with an absolute difference of 0.03 to 0.72.

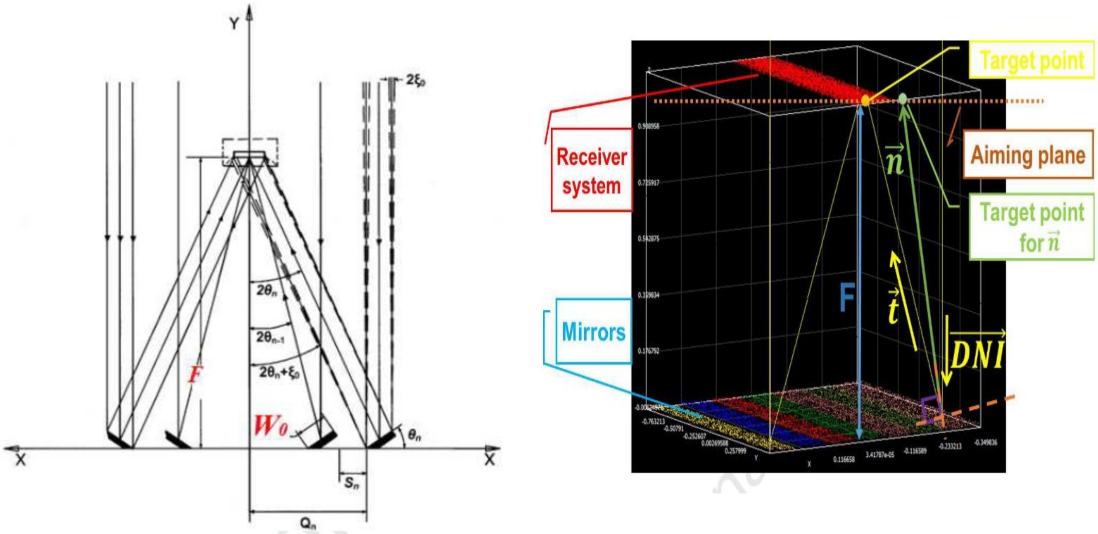

Fig. 2.25 Fresnel concentrator with cavity absorber (left-side) and Fresnel reflector SolTrace model (right-side) [48]

Mishra et al. [49] performed a numerical evaluation using optical and thermal analysis of a cavity linear receiver (CLR) with parallel tubes for a novel Cross-Linear Concentrated Solar Power (CL-CSP) system and demonstrated in a 30 kW pilot plant in Bhopal, India (Fig.2.26). They used a Monte Carlo Ray Tracing (MCRTM) simulation in SolTrace to evaluate flux distribution and used ANSYS Fluent for thermal and hydraulic analysis. Also, they used MATLAB to map the flux distribution result from SolTrace to ANSYS Fluent as a volumetric heat source. The receiver cavity is insulated with rock wool and it includes absorber tubes of 33.4 diameters and was closed with glass cover. Their study found that the optical efficiency reached 67.6% at solar noon, but it gradually declined as the afternoon approached. The thermal efficiency was found to be 40 % at working fluid temperature of 873 K and increased to 90% when the working fluid temperature decreased to 373K. The surrounding wind speed was found to affect the thermal efficiency by increasing the convective heat loss of the cavity. Also, the reflectivity of the cavity was found to influence the optical efficiency reflectivity range of 0.6 to 1. The results also indicated significant non-uniformity in both flux distribution and temperature along the axial and radial directions of the absorber tube.

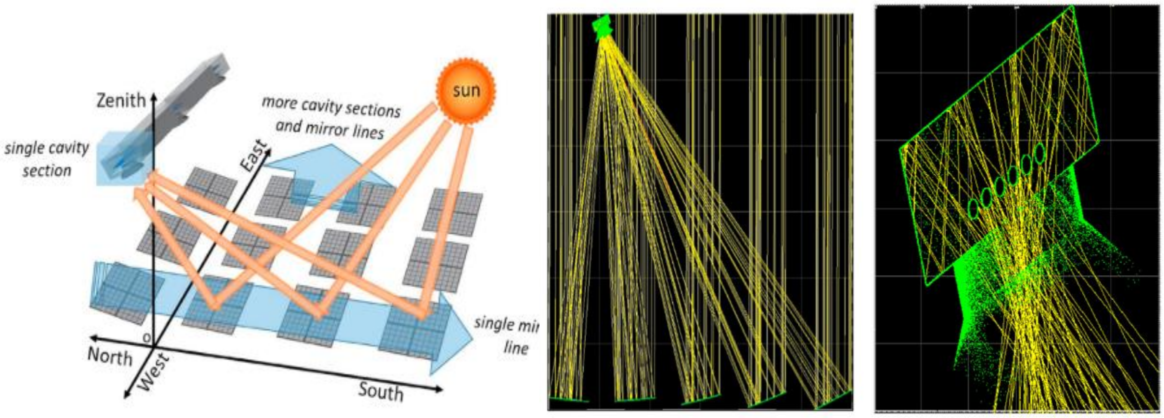

Fig. 2.26: Cross Linear concentrated solar power (left-side) and SolTrace optical simulation model (right-side) [49]

In their study, Babu et al. [50] evaluate the performance of a linear Fresnel reflector solar concentrating hot Water system using horizontal absorbers with varying width of 58 reflectors with concentration ratio of 31.4 (Fig.2.27). They compared the variable width reflector thermal performance with the constant width reflector. The result showed a maximum temperature of 78℃ at the outlet with thermal efficiency of 41.2%. However, when compared with a system with same concentration ratio and aperture diameter, the thermal efficiency difference between the variable and constant width reflector there is 1.2 thermal efficiency differences.

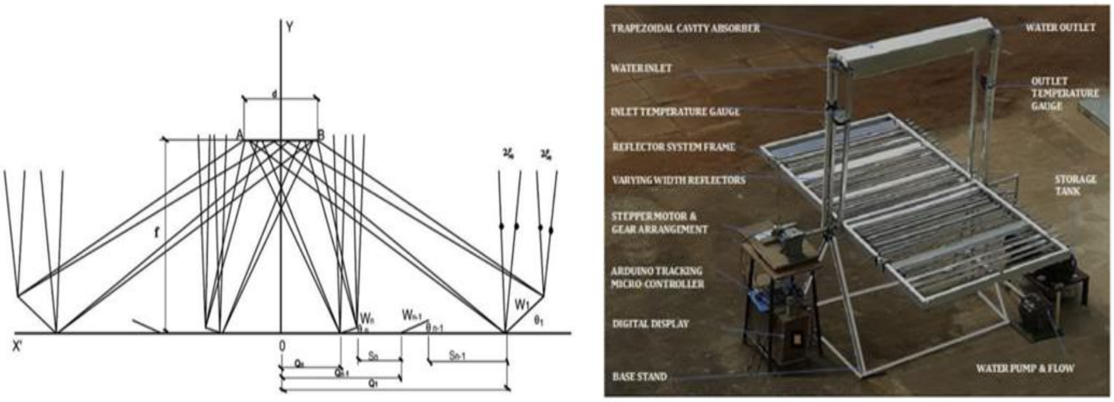

Fig. 2.27 linear Fresnel reflector solar concentrating Hot Water system [50]

Despite these improvements, box or panel-type solar cookers are fundamentally limited in their performance and they cannot reliably achieve and sustain a temperature between 200 to 300 ℃ which is required in a medium to large capacity baking or cooking. Their application is limited to low capacity cooking and for slow cooking applications [1].

The reviewed literatures demonstrate that both direct and indirect solar cooking systems have distinct strengths and limitations. Direct cookers show, simplicity and low cost which makes them suitable for household and small community applications. Indirect cookers, by contrast, offer greater control and scalability. They achieve higher efficiencies but require more complex engineering and higher upfront investment. The result from the review shows that there is a tradeoff between accessibility and technical sophistication and that highlights the need for designs that balance efficiency, cost, and user convenience (Table 2.3).

Moreover, linear Fresnel reflectors are generally considered to have strong potential for medium- and large-scale cooking applications worldwide [12]. However, to date, there are no studies in the open literature that investigate the use of solar linear Fresnel reflectors in solar baking units. Furthermore, no research in the Ethiopian context has explored the integration of linear Fresnel reflectors with a solar bread baking oven.

Table 2.3 literature review summary

Researcher & Year	**Objective**	**Methodology**	**Materials / Design**	**Findings**	**Gap Identified**	**Capacity Classification**	**Key Thermal / Optical Parameters**	**System Classification**
Gallagher (2011) [29]	Solar fryer for injera bread	Prototype + thermal loss analysis	Quasi-parabolic Mylar mirror, aluminum pan	Pan reached 180 °C; with 4 kg injera/hr	Mirror size smaller than optimal	Small/medium	Optical efficiency 60% and cooking power of 640 W	Direct-Concentrating -Domestic
Babu et al. (2019) [50]	Improve LFR hot water system	Analytical + PSO + experimental	Linear Fresnel reflector, trapezoidal absorber	Outlet temp 76 to 78 °C	Needs better geometry & coatings	Medium	Efficiency 41.2%	Indirect - Concentrating - Institutional

Ouqazzamar et al. (2026) [22]	Scheffler ovens for bread	FEM modeling	Scheffler reflector, stainless oven	Baked 32 loaves in 85-110 min and standardized cooking power of 434 W	Needs large-batch validation	Large 15kg bread	Optical efficiency 0.899 and F_1 of 0.30 and F_2 of 0.85	Direct - Concentrating - Institutional
Farimani et al. (2022) [35]	Dual-purpose Lavash oven	Simulation + solar validation	Parabolic reflector, cast iron absorber	Bread baked in 7 min; with 70g dough loading efficiency 44.1%	Needs storage integration	Small	Reflectivity 0.9–0.95 with cooking power of 4269 W/m^2 and baking Temp. of 210 °C	Direct - Concentrating - Domestic
Ayub et al. (2020) [51]	MH-TES solar bakery	COMSOL simulation	Scheffler reflector, MH storage, Dowtherm oil	Efficiency improved to 42.9%	Needs experimental validation	Large	Exergy efficiency 34%	Indirect - Concentrating - Institutional
Aragaw & Adem (2022) [36]	Tube-type solar oven	SOLTRACE + COMSOL + prototype	Cylindrical oven; parabolic reflector	Stagnation temp 127 °C in 67min, efficiency 38-44%	Airtight sealing issues	Small/medium	Baking time 51 min for 1kg loading and F_1 of 0.32 and utilization efficiency of 35%	Direct - Concentrating - Domestic
Nazari et al. (2020) [37]	AI modeling of plate temp	Hybrid MSCA + TLBO + ANFIS	Parabolic concentrator, aluminum plate	Plate temp 180 °C; for 10 to 12 breads/hr	Needs climate validation	Medium	Reflectivity 0.9-0.95	Direct - Concentrating - Domestic/Institutional
Chaudhary & Yadav	Twin vessel ETC	Experimental	40 ETCs,Hytherm-500 HTF	Rice/kadhi/khoa cooked; efficiency	Needs HTF optimizati	Medium/large	HTF temp 90–132 °C	Indirect - Non-concentrating -

(2020) [39]	cooking			between 11.8% to 78.6%	on		loaded in 2.5 and 3 Liters	Domestic/Community
Mekonnen & Kebede (2020) [31]	Hybrid box-parabolic oven	Prototype	Plywood box, parabolic trough	Max absorber temp 121 ℃ and 50 min baking time	Needs higher absorber temps	Medium size with 60 breads in 3 cycles baking	F_1 = 0.1204	Direct - Hybrid - Domestic
Harmim et al. (2013) [30]	CPC box cooker	Prototype + testing	Asymmetric CPC booster, stainless box	Absorber temps 165-166 ℃ and for 0.6 kg and 0.4 kg bread, cooking time of 2 h:55min and 2h:30 min	Needs geometry optimization	Medium	Cooking power 78.9 W and F_1 = 0.152, F_2 = 0.47	Direct - Concentrating - Domestic
Forsythe & Madyira (2019) [40]	Solar baking oven	Numerical + ETC prototype	28 ETCs, stainless oven	Oven temp 200-250 ℃, efficiency 72-78%	Needs scaling	Medium/large	Power demand 2.182 kW with baking time of 40 min for 400g (3 loaves)	Indirect - Non-concentrating - Institutional
Tesfay et al. (2014) [38]	Steam-based Injera baking	Polar-mounted dish + steam loop	2.54 m² dish, steam coil	Stagnation temp 255 °C; stove temp 135-160 °C	Needs auto-tracking & storage	Medium	CR =325, baking time of 2 min and 30 sec per injera	Indirect - Concentrating - Domestic
Retta et al. (2024) [43]	Large-scale Injera baking	CFD + Soltrace + PCM	Parabolic troughs, 92 anodized Mitads	11,000 Injera/day, efficiency 57.4% baking plate temperature was found to be between 130 to 150 ℃	Needs PCM optimization	Institutional/large	Heating capacity 2.11 kW/Mitad and total baking time of 3min	Indirect - Concentrating - Institutional

Ayub et al. (2018) [41]	Energy & exergy solar bakery	Experimental + thermodynamic modeling	Scheffler reflector, zigzag receiver, pebble bed	EUR 25-75%, exergy efficiency 6.6-56%, average receiver efficiency 63%., utilization ratio of the baking chamber was 45%.	Needs receiver optimization	Medium	Exergetic factor 59.26% receiver temperature b/n 300 to 400 ℃	Indirect - Concentrating - Domestic
Moghimi et al. (2017) [44]	Optimise LFC mirror & receiver	SolTrace + CFD + ANSYS DX	Multi-tube trapezoidal cavity, variable focal length	Optimum 22 mirrors for thermal efficiency, 30 mirrors for cost	Needs prototype validation	Institutional/ Process heat	Radiative losses dominant	Indirect - Concentrating - Institutional
Rungasamy et al. (2022) [45]	Compare Fresnel receivers	SolTrace and CFD	CPC monotube, TERC monotube/multitube, trapezoidal multitube	TERC monotube best: optical eff. 56.9%, low thermal loss	Needs coating/insulation optimization	Institutional/ Process heat	Thermal loss factor comparisons, the experimental result was comparable with simulation	Indirect - Concentrating - Institutional
Montes et al. (2014) [46]	Compare central vs compact LFC	Matlab ray tracing + SolTrace validation	Fresdemo prototype; central vs CLFC	Useful energy efficiency highest at Fresdemo config (21 m width, 12 m receiver height)	Compact LFC suffers ray dispersion	Institutional/ Process heat	Useful energy efficiency metric and optical efficiency of 60.7%	Indirect - Concentrating - Institutional
Kincaid et al. (2018) [47]	Compare LF, PT, CR optics	SolTrace ray tracing	Hyperlight LF, EuroTrough PT, SAM	Annual optical eff.: PT 60%, CR 52%, LF 40%	Needs integration with thermal/st	Utility-scale CSP	IAMs, intercept factors and cost	Indirect - Concentrating - Institutional/

			CR		orage		lower for LF	Utility
Said et al. (2019) [48]	Optical prototype LFR	Matlab + SolTrace validation	11 flat mirrors; trapezoidal cavity, copper tubes	Optical eff. 26.9–42.6%, CR 6.7–9.8	Needs scaling & coatings	Domestic/small CSP	Intercept factor 0.94,CR up to 9.8	Indirect - Concentrating - Domestic
Mishra et al. (2021) [49]	Optical – thermal analysis of CLR for CL-CSP	SolTrace MCRT + CFD (ANSYS Fluent) + MATLAB coupling	30 kW CL-CSP pilot, CLR with absorber tubes	High non-uniform flux/temperature, CLR mitigates cosine losses vs LFR/PTC	Needs geometry/insulation/tube optimization	Institutional/Process heat	Receiver temp 373 K to 873 K, mass flow 0.0925 kg/s,	Indirect - Concentrating - Institutional

Chapter 3

Materials and Methods

This chapter presents the materials and methods employed in the modelling, simulation, fabrication, and experimental evaluation of the solar baking oven integrating a linear Fresnel parabolic mirror reflector (LFPMR). The overall approach combines numerical simulation and experimental techniques to assess the performance of solar baking oven. Optical performance analysis was conducted using ray tracing simulations, SolTrace, to evaluate key parameters such as solar concentration ratio and flux distribution on the receiver. Thermal performance analysis was carried out through numerical simulations using ANSYS Fluent to predict temperature distribution, heat transfer characteristics, and thermal behaviour of the oven system. These simulation results were subsequently validated through experimental testing of the fabricated prototype under real operating conditions.

3.1 System Description

The system designed in this study is a compact, manually tracked linear Fresnel parabolic mirror reflector (LFPMR) built as a rigid assembly combining a three-row mirror field and connected through the horizontal support frame to a solar baking oven, which comprises an absorber compartment with a baking chamber, as shown in Fig.3.1.

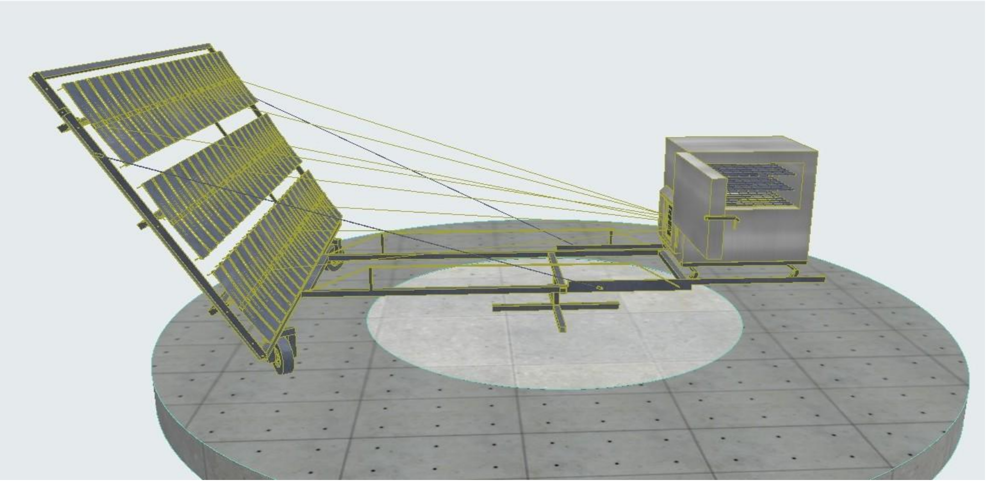

Fig. 3.1 Manual tracked linear Fresnel parabolic mirror reflector (LFPMR) system configuration

The conceptual configuration and mechanical layout were developed based on the structural and operational principles of the Lytefire solar concentrator system, whose technical information provided reference data for mirror design, arrangement, tracking strategy, and structural integration. However, the absorber configuration, optical modeling, thermal analysis, and performance evaluation presented in this study were independently designed, implemented, and optimized for the LFPMR solar baking application [52].

The concentrator mirror field consists of three rows with 19 mirror elements per row, each measuring 0.15 m by 0.60 m, providing a total concentration area of 5 m². To minimize shading effects and ease of independent calibration, a horizontal clearance of 0.025 m is maintained between adjacent mirrors within each row. In addition, the spacing between rows is set at 0.10 m between the bottom and middle rows and 0.15 m between the middle and top rows. The mirror field is mounted on an inclined rectangular frame at 60° from horizontal. The mirror frame is mounted and supported by two tires at the bottom of the base frame, and two tension cables run from the left and right sides of the upper part of the mirror frame to the anchor points on the horizontal base frame.

The solar baking oven, which comprises of an absorber compartment and a baking chamber, has a volume of 0.75 m × 1.00 m × 1.00 m (width, depth, and height). The lower portion of the solar oven includes 038m by 0.38m front transparent glass orifice for solar radiation entrance and vertical absorber plates placed at the bottom wall at different offsets distance and size. The transparent glass closes the front opening of the lower cavity and provides a controlled interface to the mirror field while limiting convective and radiative heat losses. The upper part of the solar oven is baking chamber with three compartments to accommodate three aluminum baking trays having size 0.4 m by 0.7 m (width and length) and mounted on mesh wire tray supports with 0.123 m vertical gaps between trays. The bottom tray was positioned 0.50 m above the oven's bottom wall. A loading door on the right side of the baking chamber, with a height of 0.60 m, provides access for baking operation.

The solar baking oven sits on four caster wheel tires which are integrated in a trolley on the horizontal base frame, and it enables a manual translation of the solar oven towards the concentrator and away to adjust the focal length variation at different times of the day, distance between the concentrating mirror and solar oven orifice which is fitted with transparent glass.

Both caster wheels and wheel barrow wheels are integrated with a pin lock to lock the solar oven and the mirror frame in position during operation once adjusted.

The horizontal support is mounted on a central rotational pivot with cross bar that provides a single rotational degree of freedom to both the mirror field and the solar baking oven so that they can co-rotate as a rigid assembly about this pivot, and the relative geometry between the mirror field and solar oven is preserved during tracking. The overall solar bakery parts are shown in the Fig. 3.2.

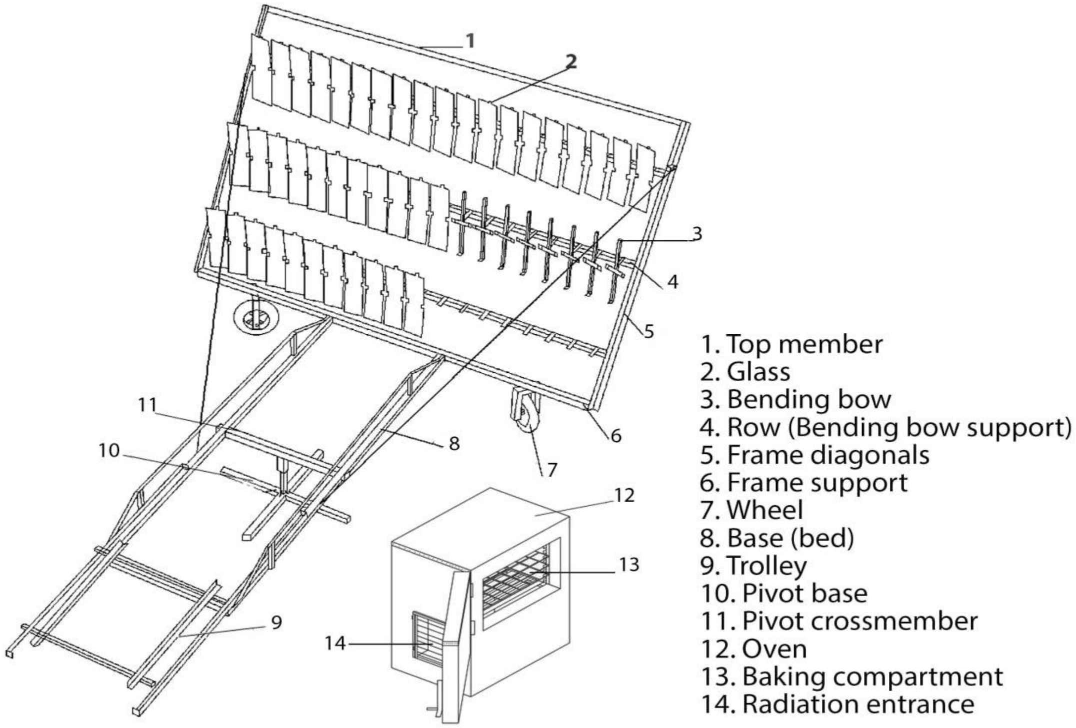

Fig. 3.2 Concentrating solar baking oven parts

The operation and tracking of the linear Fresnel parabolic mirror reflector (LFPMR) is manual and less complex in terms of design. A handle installed on the left side of the mirror frame provides mechanical leverage for moving the three row mirror fields up and down to focus the radiation in to the oven's orifice, radiation entrance, and manual rotation of the whole assembly about the central pivot. The oven translation is performed by rolling it on its tires along the rails and locking it in place when the desired focal position is reached.

This configuration utilizes single-axis co-rotation with focal tuning translation. The entire optical assembly rotates together, preserving the bisector aiming geometry computed for each mirror, while the solar oven position along the rails is adjusted to optimize intercept for different sun elevations or seasonal conditions. In operation a manual tracking adjustment is being done every 15 minutes in a day and additional seasonal repositioning as well. Cable bracing, mechanical locks, and ergonomic handle sizing were provided to ensure safe manual operation and to meet a target angular accuracy.

Concentrated solar radiation heats the vertical absorber plates, warming the air in the lower cavity. The hot air rises to the top baking chamber due to buoyancy, passes through louver perforations, mesh wire try support, around tray edges, and transfers heat to the product on the trays. The combination of absorber plate position and mesh wire trays support promotes uniform flow distribution and temperature.

3.2 Materials Selection

The selection of materials for the construction of the concentrating solar baking oven was guided by defined performance criteria. Key considerations included thermal conductivity, optical reflectivity, durability, cost effectiveness, and local availability.

For the solar concentrator, linear Fresnel parabolic mirror reflector, highly reflective glass mirror sheets were utilized due to their high solar reflectance, resistance to environmental degradation, and suitability for precise optical applications (Fig. 3.3). The absorber, serving as the receiver of concentrated solar radiation, consisted of mild steel plates, selected for their adequate thermal conductivity and capability to withstand elevated operating temperatures.

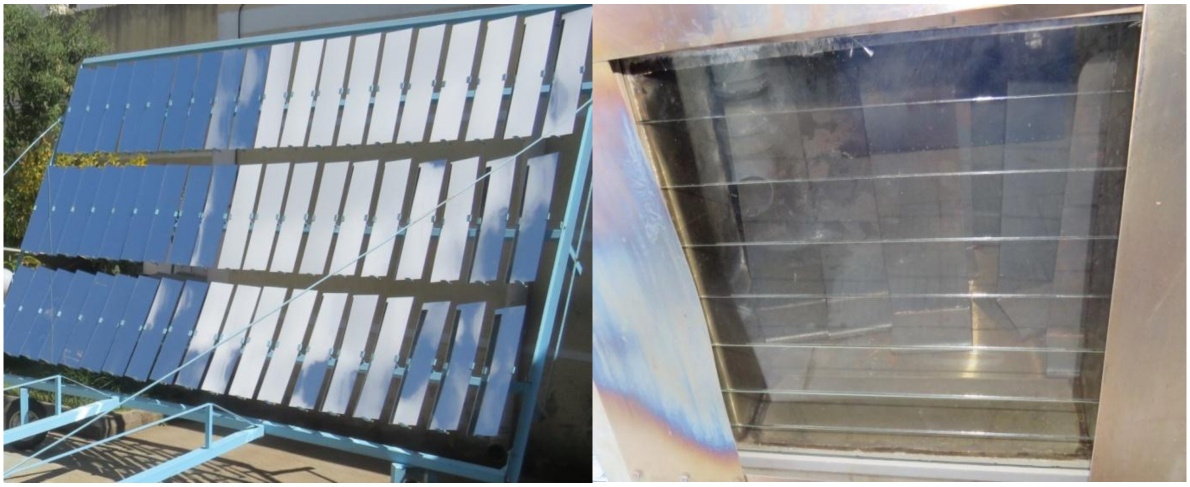

Fig. 3.3 Mirror reflector and transparent glass with absorber plates

The oven chamber is made up of a double layer configuration to enhance thermal insulation and minimize heat losses (Fig. 3.4). The inner shell consisted of stainless steel to withstand high operating temperatures and to comply with food grade requirements. The outer shell comprised of steel sheets that provided mechanical protection. Fiberglass insulation material was placed between the inner and outer shells to reduce conductive heat losses. The insulation thickness was determined based on the simulated temperature distribution to ensure safe outer surface temperatures and reduce heat loss. A 100 mm thick fiberglass layer (24 kg/m³) was used to provide effective thermal insulation. Transparent glass glazing was installed at the radiation entry opening to allow solar energy transmission into the oven chamber.

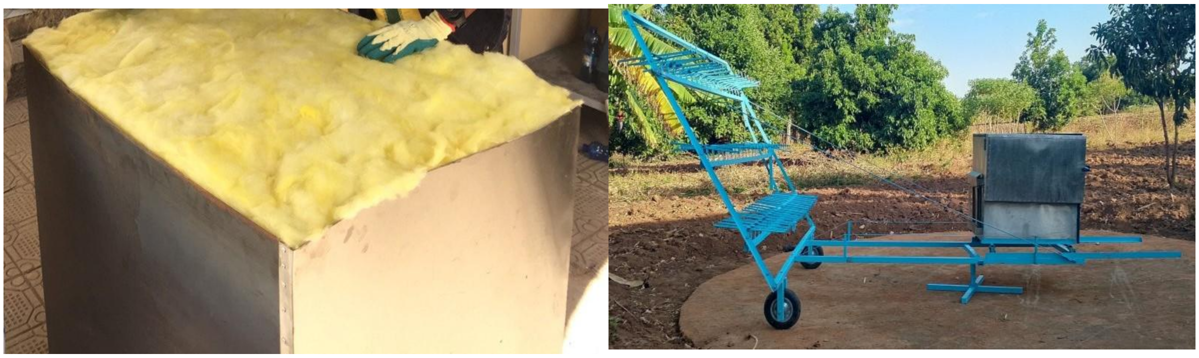

Fig. 3.4 Insulation blanket and bakery with frame

To improve thermal energy retention, the oven door incorporated a silicone gasket that ensured an airtight seal. The concentrator and oven assembly mounted on a steel structural frame selected for its mechanical strength, durability, and suitability for outdoor conditions. The structural frame maintained system stability and structural integrity throughout operation. The detail material list is attached in Appendix A.

3.3 Measuring Instruments and Experimental setup

The performance study of linear fresnel parabolic mirror reflector (LFPMR) integrated with a solar oven system is conducted in Addis Ababa, Ethiopia, located at 9°01′48″N latitude and 38°44′24″E longitude and 2,340 meters above sea level. The location receives an average daily solar insolation of approximately 5.83 kWh/m^2 and average annual sunshine duration of 2,439 hours per year. With peak solar radiation period between December and March and minimum radiation during June and August [53].

The experimental investigations were conducted at Addis Ababa University College of Technology and Built Environment Campus during May and June 2024. Two operating conditions were considered, no-load (stagnation) and a load (baking) tests. The no load test was conducted in three repetitions on May 20 and 25 and June 04 2024 and the load test was conducted on May 30 2024. The experimental setup used during the testing periods is shown in Fig.3.5.

During the experiment, both temperature and solar radiation were measured and recorded systematically. Temperature measurements were conducted using a K type thermocouple system (Creative Control, Mumbai, India), which is a multi-channel device capable of measuring temperatures up to 1200 °C with an accuracy of ±2.2 °C. A total of six thermocouple channels were deployed at strategic locations within the solar oven system, and data were recorded at 15-minute intervals.

In the baking chamber, three thermocouples were installed on the baking trays to monitor the temperature distribution during operation. Two additional thermocouples were placed in the receiver chamber, one positioned near the glass cover and the other close to the absorber plate, to capture thermal behavior in the heat absorption region. The remaining thermocouple was used to measure the ambient air temperature. The detailed placement of the thermocouples is illustrated in Fig. 3.6.

Fig. 3.5 K type thermocouples integration over different position of the solar oven

Solar radiation measurements were carried out using a solar power meter (SM206-SOLAR Solar Power Meter). The instrument is capable of measuring global horizontal irradiance within a range of 0.1 to 2000 W/m², with an accuracy of ±0.1 W/m² (Fig.3.7). The solar power meter operates within a temperature range of 0 °C to 40 °C and under relative humidity conditions of less than 80%. During the experiments, the meter was mounted on the top surface of the solar oven to ensure representative measurement of the incident solar radiation, and data were recorded at 15-minute intervals and validated with NASA data.

Fig. 3.6 Solar radiation measurement using solar power meter in prototype testing

The mass of dough and bread were measured using electronic balance with a capacity 200 g ± 0.1kg (Fig.3.8). The weight loss in g was calculated by using the measured weight difference before and after baking in triplicate manner and taking the average value.

Fig.3.7 Electronic balance

3.4 Simulation model development

3.4.1 Geometry and model setup

In this section the numerical modeling approach used in the manually tracked linear Fresnel parabolic mirror reflector (LFPMR) and the solar oven assembly with its performance evaluation will be presented. The optical model for LFPMR systems has been developed using SolTrace software which is developed by the National Renewable Energy Laboratory (NREL) [54], [55]. This software can model from simple to complex optical systems using Monte-Carlo ray tracing [48]. It is also one of widely used optical model tool and used in different solar power system modeling [48], [56]. Its result when compared with experimental data, have shown a good agreement [57], [58].

The SolTrace simulation results of the LFPMR integrated with solar oven were employed to assess the optical performance of the system and to estimate the solar power delivered to the oven absorber. Based on these results, a thermal model of the system was developed in ANSYS Fluent, where the power output obtained from SolTrace was applied as a boundary heat flux to predict the temperature distribution and airflow behavior within the solar oven assembly. The coupling methodology and data exchange between the two modeling tools are illustrated in Fig. 3.9.

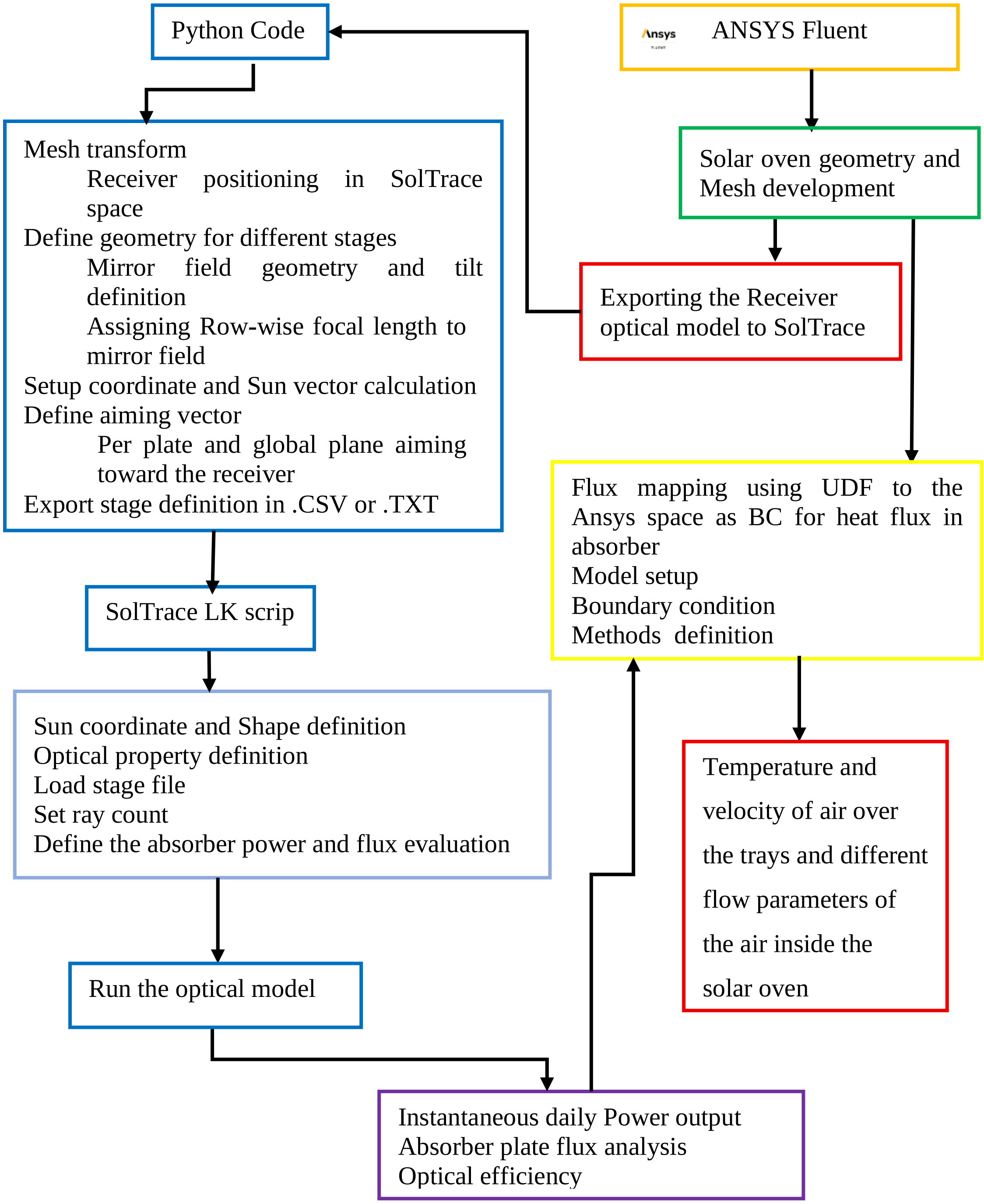

Fig. 3.8 Model integration layout and inputs of SolTrace and ANSYS modelling software

3.4.2 Geometry preparation and global alignment

The three-dimensional (3D) geometry of the solar oven assembly was developed using ANSYS Design Modeler. The model was divided into two main sections: the lower section, which includes the absorber plates, front glass cover, and side walls, and serves as the domain for optical modeling; and the upper section, which contains the baking trays and is coupled with the lower section for thermal analysis in ANSYS Fluent. To reduce computational cost without compromising model accuracy, the geometry was simplified by limiting the number of absorber plates to three. These absorber plates were strategically arranged behind the glass cover to effectively intercept the concentrated solar radiation reflected from the mirror field.

Following geometry creation, the computational mesh was generated using ANSYS Meshing, consisting of 482,284 irregular triangular elements. The mesh quality assessment yielded a minimum orthogonal quality value of 0.20, which is considered acceptable for this class of numerical simulations[59]. The developed mesh of the solar oven is shown in Fig.3.10.

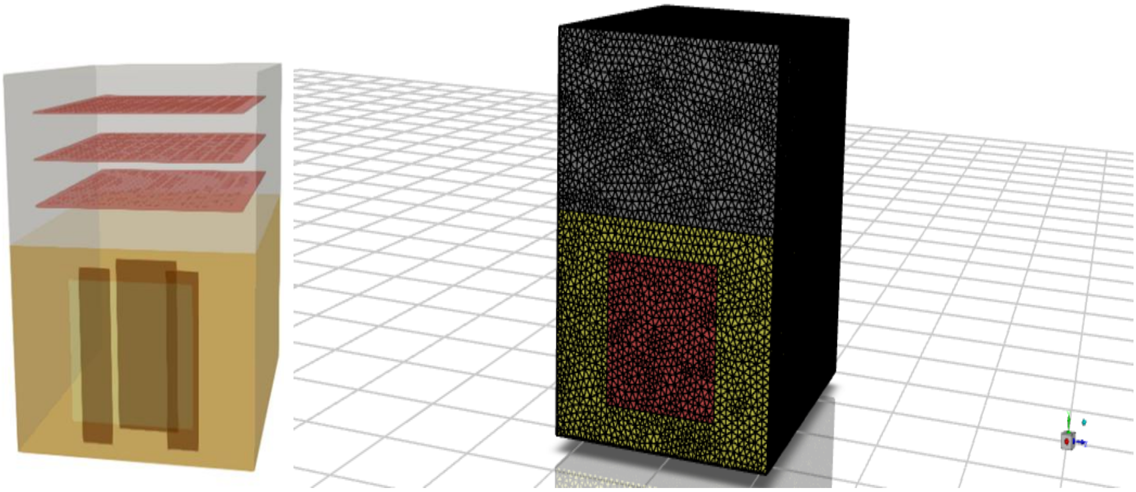

Fig. 3.9 The meshed geometry of the solar oven

3.4.2.1 The receiver geometry

Once the meshing process finished the bottom part of the solar oven model geometry is exported from Ansys Meshing to be used in optical modelling. This includes the frontal glass, side walls, and the three vertical absorber plates as shown in Fig.3.11.

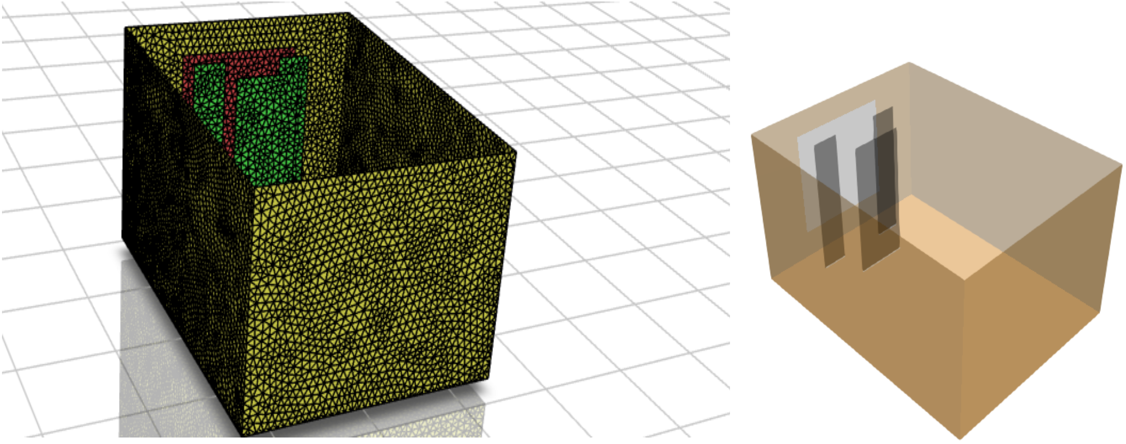

Fig. 3.10 The exported bottom part of the solar oven showing the absorber in green, the glass in red and sidewall in yellow

The mesh generated in ANSYS was exported and converted into Visualization Toolkit (VTK) format and saved as three separate components, namely the absorber, the glass cover, and the side walls, to enable their import into SolTrace as distinct optical stages. Since SolTrace operates using simplified geometric representations, the irregular triangular mesh produced in ANSYS was transformed into a compatible format that could be accurately interpreted within the SolTrace ray tracing environment. [60]. To achieve this, each flat irregular triangular element was rotated in y axis, and the corner coordinates of the triangle were identified [60]. For every triangular face the centroid, unit normal and area were computed using Equ.3.1-3.3,

$$x_m = \frac{1}{3}(P_0 + P_1 + P_2) \tag{3.1}$$

$$\hat{n}_m = \frac{(P_1 - P_0) \times (P_2 - P_0)}{|(P_1 - P_0) \times (P_2 - P_0)|} \tag{3.2}$$

$$A = \frac{1}{2}|(P_1 - P_0) \times (P_2 - P_0)| \tag{3.3}$$

The receiver geometry is positioned 0.8 m above the ground, aligned with the mirror field and oriented toward it by translating the receiver by (0, 1.51) in the X and Y directions. A rigid transformation is applied to convert the geometry exported in the ANSYS coordinate system into the SolTrace global coordinate system. In SolTrace, the Z-axis points north, the X-axis points west, and the Y-axis points upward toward the zenith. This transformation is performed using the rotational matrix shown in Equation 3.4, which is applied to the receiver geometry[60].

$$R_y = \begin{bmatrix} \cos\theta & 0 & \sin\theta \\ 0 & 1 & 0 \\ -\sin\theta & 0 & \cos\theta \end{bmatrix} \qquad 3.4$$

The transformation of the centroid points of the triangular face of receiver geometry is performed using Equ.3.5 which applies the rotational matrix (R_y) and translation vector (t) to place the geometry at required position in global Y (0.8m). Similarly, the triangular face normal is transformed by the same rotational matrix to preserve distance and orientation of the triangular face using Equ.3.6 [60].

$$x_s = R_y x_m + t \qquad 3.5$$

$$\hat{n}_s = R_y \hat{n}_m \qquad 3.6$$

3.4.2.2 Mirror field geometry and tilt

The mirror field was constructed in a three parallel row and each row contains 19 reflective mirrors. Its three parallel rows are fixed in y direction at 0.72 m,1.334 m and 1.974 m for row one, two and three respectively. Each row is assigned to a separate focal length for row one ($F_{row\,1}$), row two ($F_{row\,2}$) and row three ($F_{row\,3}$) of 3.001m, 3.389 m and 3.894 m respectively (Fig.3.12). From this focal length the parabolic curvature of each row was evaluated by considering the symmetric future of the mirror plates, the curvature in X and Y direction is equal and evaluated using Equ.3.7 [55].

$$C_x = C_y = \frac{1}{2F_{row}} \qquad 3.7$$

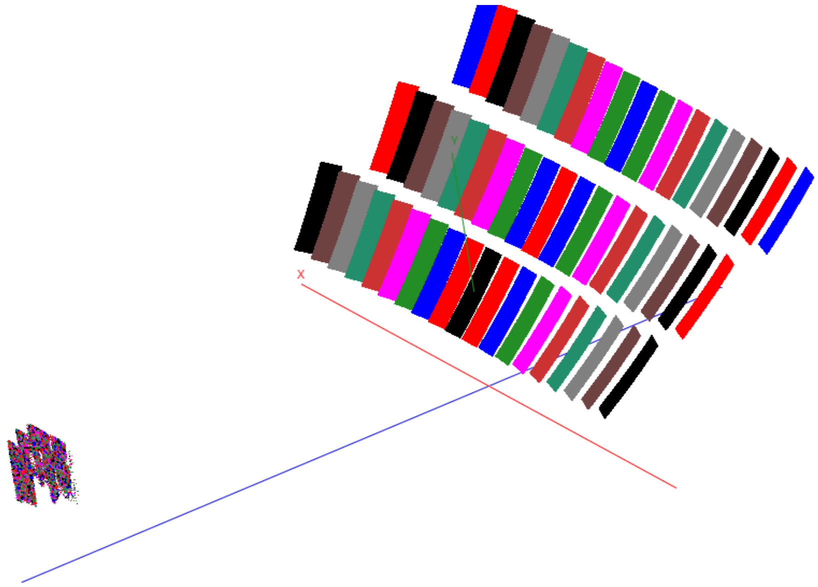

Fig. 3.11 The mirror field and the receiver geometry definition in SolTrace

The mirror field centroid is tilted by 60^0 about the X axis (north-south axis) using the standard right-hand rule through the rotation matrix given in Equ.3.8, so that the positive angle θ rotates the Y axis toward positive Z.

$$R_x(\theta) = \begin{bmatrix} 1 & 0 & 0 \\ 0 & \cos\theta & -\sin\theta \\ 0 & \sin\theta & \cos\theta \end{bmatrix} \qquad 3.8$$

3.4.2.3 Sun Vector Calculation

The sun position vectors were calculated through the solar declination angle (δ), hour angle (ω), solar altitude (α) and azimuth angle (A) were evaluated using solar time, latitude of the place ($\emptyset$) and from the day number of the year (n), as shown in Equ.3.9-3.12 [54], [61], [62].

$$\delta = 23.45 * \sin\left(\left(\frac{360}{365}\right) * (284 + n)\right) \qquad 3.9$$

$$\omega = 15 * (ST - 12) \qquad 3.10$$

$$\alpha = \sin^{-1}(\sin\emptyset * \sin\delta + \cos\emptyset \cos\delta \cos\omega) \qquad 3.11$$

$$A = \tan^{-1}\left(\frac{\sin\omega}{\cos\omega * \sin\emptyset - \tan\delta * \sin\emptyset}\right) \qquad 3.12$$

Finally using the above result the sun vector ($\hat{S}$) will be evaluated in SolTrace coordinate system using Equ.3.13-3.14 [62].

$$s_x = \cos\alpha \sin A \tag{3.13}$$

$$s_y = \sin\alpha \tag{3.14}$$

$$s_z = -\cos\alpha \sin A \tag{3.15}$$

3.4.2.4 Aiming strategy

In this study two aiming cases are considered as shown in Fig.3.13 below. The first case was aiming at the triangular face of the three absorber plates and dividing the mirror field into three part and each part is aiming at the three plates plane which are perpendicular to the mirror fields plane in this case it is the X-Y plane and this plate plane is created by weight averaging the centroid of the elements in that plate as shown in Fig 3.13 (a) , while the second aiming approach was developed by modifying how the plane was created, in this case the plane is created by taking the centroid of all triangular elements of the absorber plates and applying weighted averaging then using the result a plane will be created however in this case the plane will be parallel to the mirror field as shown in Fig 3.13 (b).

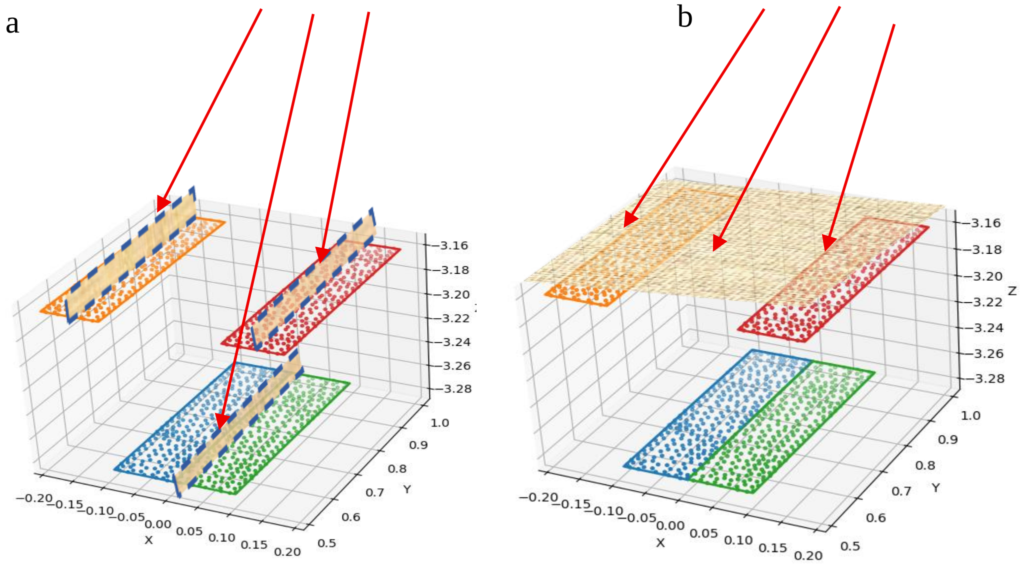

Fig. 3.12 Aiming at plane perpendicular to the mirror field (a) and aiming at global plane parallel to the mirror field (b)

Both aiming approaches divide the mirror field for each absorber plates. This was done as follows, the receiver absorber plates are divided into three group which are the front left and right with the back center plate using their centroid (x_s) of the plates triangular face. Using each mirror centroid (H) and absorber plate triangular face centroid (x_s), the absorber plate triangular faces are group by calculating the nearest distance (d_i) using Eq.3.16. Fig.3.14 shows these parameters including the mirror normal with other variable to help visualize the approach. Once the nearest absorber triangle centroid is selected, the unit target vector is evaluated using the Equ.3.17. Using this and sun vector ($\hat{S}$), the mirror normal which bisect the incoming sun vector and the vector from the mirror to the selected absorber center is evaluated using Equ.3.18 [48], [61].

$$d_i = |x_s + \mathrm{H}| \qquad 3.16$$

$$\hat{\mathrm{k}}_{out} = \frac{X_s+H}{|X_s+H|} \qquad 3.17$$

$$\hat{\mathrm{n}} = \frac{\hat{S}+\hat{\mathrm{k}}_{out}}{|\hat{S}+\hat{\mathrm{k}}_{out}|} \qquad 3.18$$

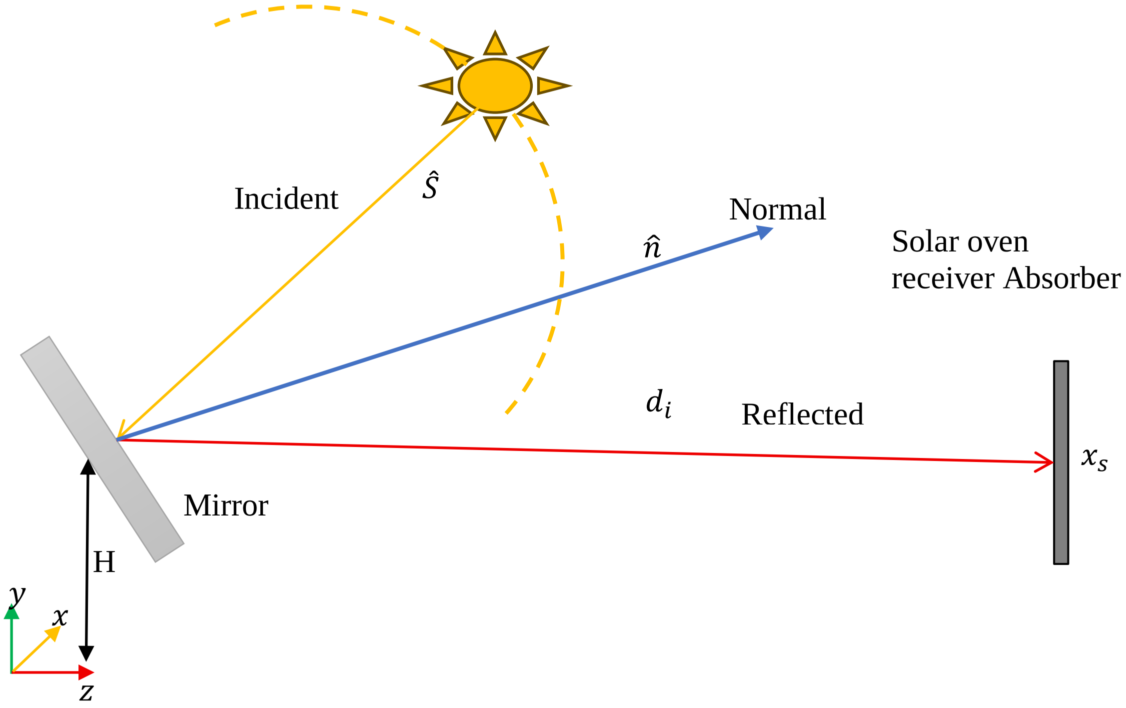

Fig. 3.13 Mirror aiming point grouping

The SolTrace model was developed using the LK scripting language which is used to define and compute the sun vector, as described in Equations (3.9–3.15), and the assigned optical properties of the system are summarized in Table 3.1. The solar source was represented using a pillbox sun model with a half-angle of 4.65 milirad, as illustrated in Fig.3.15, with a global sun vector definition [57], [63], [64].

Table 3.1 Optical parameters used in the LK script

Element	Property Definition	References
Mirror	Mirror reflectivity (ρ)= 0.94, slope error = 1.5, specular error = 0.5 mrad	[63]
Glass	Glass transmittance (τ) = 0.95, refractive index = 1.5, slope error = 0.2	[65]
Absorber	Absorber reflectivity = 0.03, transmittivity =0.0,	[63]
Side wall	Side wall reflectivity = 0.2, slope error=0.5	[63]

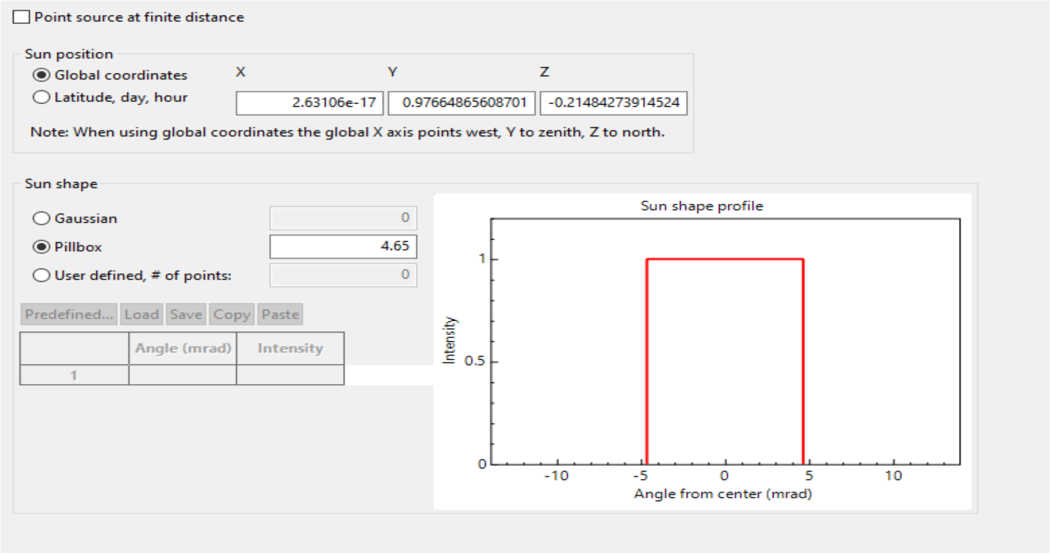

☐ Point source at finite distance

Sun position

● Global coordinates
○ Latitude, day, hour

X	Y	Z
2.63106e-17	0.97664865608701	-0.21484273914524

Note: When using global coordinates the global X axis points west, Y to zenith, Z to north.

Sun shape

○ Gaussian 0
● Pillbox 4.65
○ User defined, # of points: 0

Fig. 3.15 The sun shape and global sun vector definitions

3.5 Governing equations

The steady-state continuity, momentum and energy equations are shown in Equ.3.19-3.21 [59], [66].

$$\nabla \cdot (\rho\vec{v}) = 0 \tag{3.19}$$

$$\nabla . (\rho\vec{v}\vec{v}) = -\nabla p + \nabla . (\bar{\bar{\tau}}) + \rho\vec{g} + \vec{F} \tag{3.20}$$

$$\nabla \cdot (\vec{v}\,(\rho E + p)) = \nabla \cdot [\mathrm{k}\nabla T + \textstyle\sum_j h_j\vec{J}_j + (\bar{\bar{\tau}}_{eff} \cdot \vec{v})] + S_h \tag{3.21}$$

Buoyancy body force $\rho\vec{g}$ is evaluated using the ideal-gas density$\left(\rho = \frac{P}{RT}\right)$.

The terms in the Energy conservation equation used in ANSYS Fluent are left-hand side term $\nabla \cdot \left(\vec{v}\,(\rho E + p)\right)$ convective transport of total energy and right-hand side terms $\mathrm{k}\nabla T$ conduction heat transfer, $\sum_j h_j\vec{J}_j$ energy transport due to mass diffusion, $+(\bar{\bar{\tau}}_{eff} \cdot \vec{v})$ viscous dissipation term, and S_h absorbed solar heat flux.

3.5.1 Radiation model

The Surface-to-Surface (S2S) radiation model was employed to simulate radiative heat transfer within the closed chamber. The S2S model is designed for enclosures where radiation occurs between surfaces and the working fluid will not be considered. It calculates radiative exchange inside the solar oven based on geometric relationships between surfaces, using the view factors that quantify the fraction of radiation leaving one surface and reaches to the another surface [59].

The model assumes surfaces behave as grey, diffuse emitters and reflectors, where their emissivity and absorptivity are wavelength independent and radiation is uniformly scattered in all directions. This assumption simplifies the treatment of radiative heat transfer and it was used in similar studies involving natural convection coupled with surface radiation [58], [67], [68], [69]. The governing radiative heat exchange between surfaces is expressed using the radiative heat flux $q_{rad,i}$ from surface i to surface j in Equ.3.22 [59].

$$Q_{rad,i} = \textstyle\sum_{j=1}^{N} \sigma \varepsilon_i \mathrm{A}_i F_{i,j} \left({T_i}^4 - {T_j}^4\right) \tag{3.22}$$

Where, σ is the Stefan-Boltzmann constant, A_i is area of surface i, ε_i is emissivity of surface i, F_{ij} view factor between surface i and j, T_i and T_j are absolute temperatures of surface i and j. To handle all participating surface, the net radiosity J_i for N total surface will be computed using Equ.3.23 [59].

$$J_i = \varepsilon_i \sigma {T_i}^4 + (1 - \varepsilon_i) \sum_{j=1}^{N} F_{i,j} J_j \qquad 3.23$$

3.5.2 Turbulent model

Depending on the Rayleigh number (Equ.3.24), the flow could be turbulent or laminar.

$$Ra = \frac{g\beta(T_h - T_c)L^3}{\nu\alpha} \qquad 3.24$$

where β is the coefficient of thermal expansion (K^{-1}), g is the gravitational acceleration ($9.81 m^2/s$), L is the chamber height (1 m), $\Delta T = T_s - T_a(K)$ where T_s is temperature of absorber surface and T_a is ambient temperature, ν kinematic viscosity and α is the thermal diffusivity of the fluid. Property of air is evaluated at mean temperature $(T_s - T_a)/2$. The value of Rayleigh number of the considered case in this study is found to be around 1.55×10^9 in average and maximum value of around 7×10^9, based on temperature found from the experiment. This puts the flow in a transition to turbulent [70] and in simulation turbulent flow is considered.

There are different turbulent models in ANSYS, Shear Stress Transport (SST) k- ω model is found to be suitable for natural convection flow in a cavity. This model is widely accepted in industry for its ability to predict complex flow separation and recirculation phenomena in adverse pressure gradient conditions, making it suitable for capturing the turbulent natural convection behavior in vertical enclosures [71]&[70]. The k-ω SST model incorporates a limiter on turbulent viscosity to prevent over prediction of turbulence in regions with strong acceleration or stagnation [58].

For simulating turbulent natural convection in the chamber, the k- ω SST turbulence model was employed. The k-ω SST model is a two equation eddy viscosity model that solves transport equations for both the turbulent kinetic energy (k) and the specific dissipation rate (ω) [59]. It combines the advantages of the standard k-ω model near walls or inner boundary where it accurately resolves boundary layers and the k-ε model in the free stream or outer boundary layer, through a blending function that activates the appropriate model depending on the flow region.

The turbulent scalar quantities (k and ω) are determined from the Equ.3.25 and 3.26, respectively [59].

$$\frac{\partial}{\partial x_i}(\rho k u_i) = \frac{\partial}{\partial x_j}\left(\Gamma_K \frac{\partial k}{\partial x_j}\right) + G_k - Y_k + S_k \qquad 3.25$$

$$\frac{\partial}{\partial x_i}(\rho \omega u_i) = \frac{\partial}{\partial x_j}\left(\Gamma_\omega \frac{\partial \omega}{\partial x_j}\right) + G_\omega - Y_\omega + D_\omega + S_\omega \qquad 3.26$$

Here, G_k represents the generation of turbulent kinetic energy, G_ω is the production of ω, Γ_k is effective diffusivity of k, Γ_ω is effective diffusivity of ω, Y_k is turbulence dissipation of k, Y_ω is turbulence dissipation of ω, D_ω is cross diffusion, S_k and S_ω are user-defined source terms for k and ω respectively. The model constants for SST k-ω turbulence model are given below and the detail description and formulation of the model can be found in ANSYS FLUENT user guide [59].

$\sigma_{k,1} = 1.176$, $\sigma_{\omega,1} = 2.0$, $\sigma_{k,2} = 1.0$, $\sigma_{\omega,2} = 1.168$, $a_1 = 0.31$, $\beta_{i,1} = 0.075$, $\beta_{i,2} = 0.0828$,

$\alpha_\infty^* = 1$, $\alpha_\infty = 0.52$, $\alpha_0 = \frac{1}{9}$, $\beta_\infty^* = 0.09$, $R_\beta = 8$, $R_k = 6$, $R_\omega = 2.95$, $\zeta^* = 1.5$

3.6 Numerical methods and Boundary conditions

After setting the CFD models, the boundary conditions were set as described in below (Table.3). The fluid is considered as viscous and Newtonian. The fluid domain is set initially at reference temperature $T_{ref} = 288$ K. The thermo-physical properties of the air is modeled as ideal gas due to the higher temperature expected inside the solar oven which is using simple model like Boussinesq approximation may not represent the property of the air inside the solar oven [44]. Also the specific heat C_p and k thermal conductivity of air are defined with temperature dependent piecewise linear functions [56], [66]. There vales are presented in Table 3.2 below.

Table 3.2 Thermo-physical properties of the air

Temperature $T(K)$	$C_p(J/kg\cdot K)$	$k\ (10^{-2}\ \times \mathrm{W/m\cdot K})$
280	1005	2.53
300	1007	2.63
350	1010	2.79
400	1012	2.93
450	1015	3.07
500	1018	3.20
600	1024	3.45

There is no inlet boundary condition to force the external air, the flow is generated due to natural convection from heated absorber. The solver resolves buoyancy driven flow in the cavity and the outer boundaries are treated insulated that not heat transfer to the ambient. Absorber surface is mapped as a heat flux $q''(x, y)$ using the UDF which applies the result from the SolTrace optical model to corresponding mesh faces. The UDF used in this study is attached in APPENDIX 3. Internal emissivity is set to $\varepsilon_i = 0.95$ to model radiative losses to other surfaces. Side walls, oven compartment and glass walls are all opaque walls with prescribed emissivity ε_i of 0.85 and 1.0 and all participate in view factor calculations. Table 3.3 shows the properties of materials defined in the thermal modeling for different parts of the solar oven.

Table 3.3 Solar oven material properties

Part	**Material**	**Thickness**	**Thermal Conductivity ($\mathrm{W\ m^{-1}\ K^{-1}}$)**	**Specific Heat ($\mathrm{JKg^{-1}k^{-1}}$)**	**Density ($\mathrm{Kg\ m^{-1}}$)**	**Participates in View Factor Calculation**	**Radiation BC Type**	**Internal Emissivity**
Oven outer wall	Steel	2 mm	37.35	666.5	7850	yes	Opaque	0.85
Oven inner wall	Stainless steel	2 mm	21.27	535.48	8030	yes	Opaque	0.85
Tray	aluminum		202.4	871	2719	yes	Opaque	0.85
Absorber	Steel	2 mm	37.35	666.5	7850	yes	Opaque	0.95
Glass window	Glass	4 mm	1.5	786	2650	No	Opaque	1

Finally, the solution methods were set for a steady state pressure-based model. The pressure-velocity coupling algorithm was set as Coupled and second order upwind discretization was set for density, momentum, turbulence and energy whereas for pressure, the body force weighted discretization was set. The under-relaxation factors were set to their default value for all variables.

Convergence of the steady-state simulation was evaluated using the scaled residuals of 10^{-6} for energy equation and 10^{-4} for all other equations. Furthermore, a plane was created inside the domain and the area weighted average of temperature was monitored in this plane. The solution was considered to be fully converged when the percentage change in the consecutive iteration becomes less than 0.1% for the last 20 iteration in addition to the standard target criteria. Finaly the simulation result will be compared with the experimental result using the percentage difference of the two results using Equ.3.27.

$$Pd = \frac{Sim_{Tem} - Exp_{Tem}}{Exp_{Tem}} \times 100\% \qquad 3.27$$

3.7 Performance analysis

3.7.1 Concentration ratios

The geometric concentration ratio (CR_m) used in this study is calculated using Equ.3.28.

$$CR_m = \frac{A_{am}}{A_{ab}} \qquad 3.28$$

Where A_{am} (m^2) is the mirror concentrator surface area and A_{ab} (m^2) is the absorber surface area [72].

3.7.2 Intercept factor

Intercept factor (geometric) γ,which measures the fraction of reflected rays that successfully strikes the absorber is evaluated using Equ.3.29 [73]&[74].

$$\gamma = \frac{Power\ intercepted\ by\ absorber}{Power\ incident\ on\ primary\ reflector\ aperture} = \frac{Q_{ab}}{I_b * A_{am}} \qquad 3.29$$

3.7.3 Optical efficiency

The optical efficiency which is a function of the intercept factor and reflectivity of the mirror field (ρ), transmissivity of the glass cover (ρ), the absorptance of the absorber plates ($\alpha = 1 - \tau - \rho$) of LFPMR solar oven is evaluated using Equ.3.30 [74].

$$\eta_{opt} = \gamma * \rho\tau\alpha \qquad 3.30$$

3.7.4 Figure of merit

The first figure of merit F_1 of a solar oven is defined by the ratio of optical efficiency to heat loss coefficient of the system. It is evaluated from the no load testing using the following Equ.3.31 [36].

$$F_1 = \frac{\eta_o}{U_L} = \frac{T_{ps} - T_{as}}{I_b} \qquad 3.31$$

Where T_{ps} T_{amb} and I_b are stagnation temperature, average ambient temperature and direct normal radiation respectively.

3.7.5 Thermal efficiency of the system

To evaluate the thermal efficiency of the system the useful energy (Q_u) was divided by the available solar energy on the mirror field as show in Equ.3.32 [36].

$$\eta_{th,sys} = \frac{Q_u}{I_b A_{am} \Delta t} \qquad 3.32$$

The useful energy (Q_u) is obtained using Equ.3.33.

$$Q_u = Q_{sh} + Q_{lh} \qquad 3.33$$

Where, Q_{sh} is the sensible heat of the product and $Q_{lh}$is the latent heat and computed using Equ.3.34 and 3.35.

$$Q_{sh} = m_{im} c_{pb} (T_f - T_o) \qquad 3.34$$

$$Q_{lh} = m_{mb} L_w \qquad 3.35$$

Where, m_{im} is the initial mass loaded bread/dough on to the solar oven, and m_{mb} is the mass of water removed from the bread ($m_{im} - m_{fm}$) , L_w is latent heat of water (2,260 kJ/kg), T_o and T_f are the initial and final temperature of the bread and c_{pb} specific heat of bread dough which is evaluated using the a temperature dependent equation give for a bread dough given below in Equ.3.36 [36].

$$c_p = 0.077 * T^2 - 68.94 * T + 16646 \qquad 3.36$$

3.7.6 Water boiling test

The water boiling test on the LFPMR integrated solar oven was conducted and the performance was evaluated. A pot filled with 5 L tap water was used to conducted the experiment following the 7000 g per aperture area [75]. the water filled pot was placed at the middle tray of the solar oven. To measure the change in temperature of the water, a thermocouple was inserted from the top lid to the center of the pot, and the hole is then sealed to prevent leakage. During the experiment the temperature of the water, the air around the pot, incident radiation and the ambient temperature were measured. The measurements were taken between the 1 hours from solar noon.

The solar oven instantaneous power, $\dot{Q}''$ is defined as the rate of useful energy available during heating period. It is the product of mass, specific heat capacity of water and change in water temperature over the time duration was used to evaluate the solar oven power in Watts using Equ.3.37 [76]

$$\dot{Q}'' = \frac{(m_w C_W)(T_{wi} - T_{wf})}{\Delta t} \qquad 3.37$$

Where, T_{wi} and T_{wf} are the initial and final water temperature in °C, m_w is mass of water in kg which is in this case 5 kg and C_W is heat capacity of water 4186 J/kg.°C. here the pot specific heat and mass have not been considered due to their minimal effect on the output result [77].

Using the Hottel -Whillier-Bliss equation for the concentrating system, the instantaneous oven power can be related to the energy balance inside the solar oven, can be evaluated using Equ.3.38 [78].

$$\dot{Q}'' = F' \left[\eta_O \, I_b - \left(\frac{U_L}{CR_m}\right)(T_{wm} - T_a)\right] \qquad 3.38$$

Where $\dot{Q}''$ is the rate of useful energy gain per unit area by water, η_O is the optical efficiency , I_b is the average total irradiance, U_L is the heat loss factor, CR_m is the concentration ratio, T_{wm} and T_a are the average mean water temperature in the interval and average ambient temperature, respectively and the heat exchange efficiency factor (F'). In this equation, the changes in ambient temperature and solar radiation are assumed to be constant, so that the heat loss can be considered constant. The instantaneous efficiency of the oven can be calculated by dividing Equ.38 with average radiation (I_b), as shown in Equ.3.39 [79].

$$\frac{\dot{Q}''}{I_b} = \left[F'\eta_O{}' - \left(\frac{F'U_L}{CR_m}\right)\left(\frac{T_{wm}-T_a}{I_b}\right)\right] \qquad 3.39$$

where $\eta_O{}'$ is the corrected optical efficiency, and using the experimental test data the values of the other parameters can be found by plotting the $\dot{Q}''/I_b$ vs. $(T_{wm} - T_a)/I_b$ and the slope and intercept of a linear plot fit can be used to find $F'\eta_O$ and $F'U_L/CR_m$ [78]. Finally using the ratio of the $F'\eta_O$ and $F'U_L/CR_m$ the opto-thermal ratio (COR) can be evaluated as shown in Equ.3.40 [78],

$$COR = \frac{\eta_O CR_m}{U_L} \qquad 3.40$$

The second figure of merit F_2 for the solar oven is defined using [80] Equ.3.41,

$$F_2 = \frac{F_1\, m_w C_w}{A_{am}\Delta t} \ln\left[\frac{1-\frac{1}{F_1}\left(\frac{T_{wi}-T_a}{I_b}\right)}{1-\frac{1}{F_1}\left(\frac{T_{wf}-T_a}{I_b}\right)}\right] \qquad 3.41$$

Chapter 4

Results and Discussion

In this chapter the results obtained from both simulation and experimental investigation conducted on Linear Fresnel Parabolic Mirror Reflector integrated with solar baking oven will be presented in the consecutive subsection. The analyses were performed to evaluate the solar bakery's optical, thermal, and overall baking performance. The results include outcomes from optical and thermal simulations using SolTrace and ANSYS, findings from experimental stagnation and baking tests, performance analysis comparing modeled and experimental data, and a comparative discussion with relevant literature.

4.1 Simulation Result

The optical and thermal simulations were conducted for the weather conditions of May 5, using the average direct normal irradiance (DNI) of 1000 W/m² and ambient temperature of 300k around solar noon (Fig.4.1).

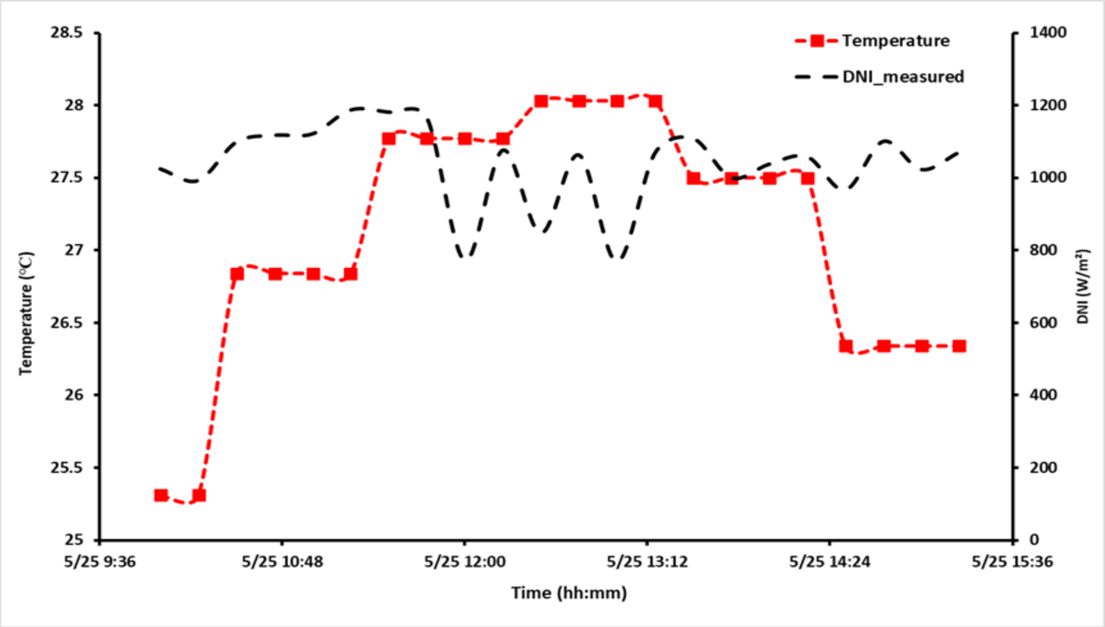

Fig. 4.1 Global horizontal irradiance (GHI) and ambient temperature for 5/25/2024

4.1.1 Optical model result

The Linear Fresnel Parabolic Mirror Reflector (LFPMR) integrated with the solar oven receiver was modeled as a multi-stage optical system consisting of the absorber, front glass cover, and sidewalls of the solar oven. These components were generated using the code presented in Appendix C, which converts ANSYS mesh elements into the SolTrace coordinate system, defines the mirror field, and generates the element definitions and aiming vectors required as input files for SolTrace.

Using the script provided in Appendix D, developed with the LK scripting language in SolTrace, a Monte Carlo ray-tracing model of the LFPMR integrated with the solar oven receiver was established. The exported geometry was then imported into SolTrace and defined across four optical stages, each with its corresponding optical properties, as illustrated in Fig. 4.2.

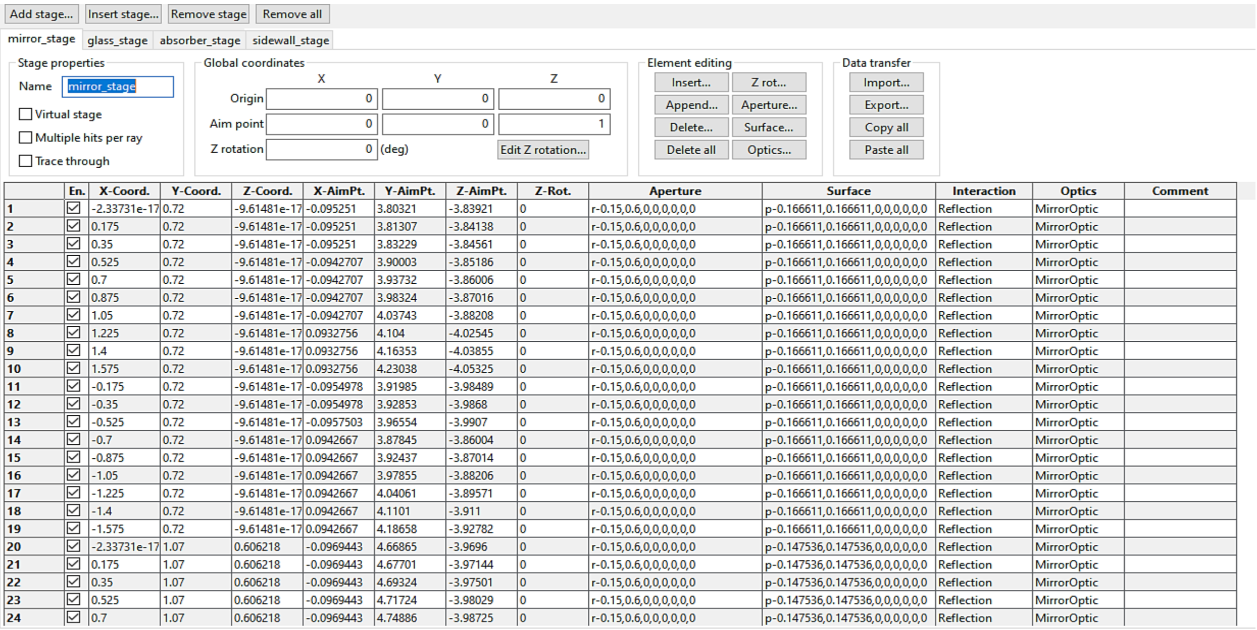

Name mirror_stage

☐ Virtual stage

☐ Multiple hits per ray

☐ Trace through

	X	Y	Z
Origin	0	0	0
Aim point	0	0	1
Z rotation	0	(deg)	

	En.	X-Coord.	Y-Coord.	Z-Coord.	X-AimPt.	Y-AimPt.	Z-AimPt.	Z-Rot.	Aperture	Surface	Interaction	Optics	Comment
1	☑	-2.33731e-17	0.72	-9.61481e-17	-0.095251	3.80321	-3.83921	0	r-0.15,0.6,0,0,0,0,0,0	p-0.166611,0.166611,0,0,0,0,0,0	Reflection	MirrorOptic	
2	☑	0.175	0.72	-9.61481e-17	-0.095251	3.81307	-3.84138	0	r-0.15,0.6,0,0,0,0,0,0	p-0.166611,0.166611,0,0,0,0,0,0	Reflection	MirrorOptic	
3	☑	0.35	0.72	-9.61481e-17	-0.095251	3.83229	-3.84561	0	r-0.15,0.6,0,0,0,0,0,0	p-0.166611,0.166611,0,0,0,0,0,0	Reflection	MirrorOptic	
4	☑	0.525	0.72	-9.61481e-17	-0.0942707	3.90003	-3.85186	0	r-0.15,0.6,0,0,0,0,0,0	p-0.166611,0.166611,0,0,0,0,0,0	Reflection	MirrorOptic	
5	☑	0.7	0.72	-9.61481e-17	-0.0942707	3.93732	-3.86006	0	r-0.15,0.6,0,0,0,0,0,0	p-0.166611,0.166611,0,0,0,0,0,0	Reflection	MirrorOptic	
6	☑	0.875	0.72	-9.61481e-17	-0.0942707	3.98324	-3.87016	0	r-0.15,0.6,0,0,0,0,0,0	p-0.166611,0.166611,0,0,0,0,0,0	Reflection	MirrorOptic	
7	☑	1.05	0.72	-9.61481e-17	-0.0942707	4.03743	-3.88208	0	r-0.15,0.6,0,0,0,0,0,0	p-0.166611,0.166611,0,0,0,0,0,0	Reflection	MirrorOptic	
8	☑	1.225	0.72	-9.61481e-17	0.0932756	4.104	-4.02545	0	r-0.15,0.6,0,0,0,0,0,0	p-0.166611,0.166611,0,0,0,0,0,0	Reflection	MirrorOptic	
9	☑	1.4	0.72	-9.61481e-17	0.0932756	4.16353	-4.03855	0	r-0.15,0.6,0,0,0,0,0,0	p-0.166611,0.166611,0,0,0,0,0,0	Reflection	MirrorOptic	
10	☑	1.575	0.72	-9.61481e-17	0.0932756	4.23038	-4.05325	0	r-0.15,0.6,0,0,0,0,0,0	p-0.166611,0.166611,0,0,0,0,0,0	Reflection	MirrorOptic	
11	☑	-0.175	0.72	-9.61481e-17	-0.0954978	3.91985	-3.98489	0	r-0.15,0.6,0,0,0,0,0,0	p-0.166611,0.166611,0,0,0,0,0,0	Reflection	MirrorOptic	
12	☑	-0.35	0.72	-9.61481e-17	-0.0954978	3.92853	-3.9868	0	r-0.15,0.6,0,0,0,0,0,0	p-0.166611,0.166611,0,0,0,0,0,0	Reflection	MirrorOptic	
13	☑	-0.525	0.72	-9.61481e-17	-0.0957503	3.96554	-3.9907	0	r-0.15,0.6,0,0,0,0,0,0	p-0.166611,0.166611,0,0,0,0,0,0	Reflection	MirrorOptic	
14	☑	-0.7	0.72	-9.61481e-17	0.0942667	3.87845	-3.86004	0	r-0.15,0.6,0,0,0,0,0,0	p-0.166611,0.166611,0,0,0,0,0,0	Reflection	MirrorOptic	
15	☑	-0.875	0.72	-9.61481e-17	0.0942667	3.92437	-3.87014	0	r-0.15,0.6,0,0,0,0,0,0	p-0.166611,0.166611,0,0,0,0,0,0	Reflection	MirrorOptic	
16	☑	-1.05	0.72	-9.61481e-17	0.0942667	3.97855	-3.88206	0	r-0.15,0.6,0,0,0,0,0,0	p-0.166611,0.166611,0,0,0,0,0,0	Reflection	MirrorOptic	
17	☑	-1.225	0.72	-9.61481e-17	0.0942667	4.04061	-3.89571	0	r-0.15,0.6,0,0,0,0,0,0	p-0.166611,0.166611,0,0,0,0,0,0	Reflection	MirrorOptic	
18	☑	-1.4	0.72	-9.61481e-17	0.0942667	4.1101	-3.911	0	r-0.15,0.6,0,0,0,0,0,0	p-0.166611,0.166611,0,0,0,0,0,0	Reflection	MirrorOptic	
19	☑	-1.575	0.72	-9.61481e-17	0.0942667	4.18658	-3.92782	0	r-0.15,0.6,0,0,0,0,0,0	p-0.166611,0.166611,0,0,0,0,0,0	Reflection	MirrorOptic	
20	☑	-2.33731e-17	1.07	0.606218	-0.0969443	4.66865	-3.9696	0	r-0.15,0.6,0,0,0,0,0,0	p-0.147536,0.147536,0,0,0,0,0,0	Reflection	MirrorOptic	
21	☑	0.175	1.07	0.606218	-0.0969443	4.67701	-3.97144	0	r-0.15,0.6,0,0,0,0,0,0	p-0.147536,0.147536,0,0,0,0,0,0	Reflection	MirrorOptic	
22	☑	0.35	1.07	0.606218	-0.0969443	4.69324	-3.97501	0	r-0.15,0.6,0,0,0,0,0,0	p-0.147536,0.147536,0,0,0,0,0,0	Reflection	MirrorOptic	
23	☑	0.525	1.07	0.606218	-0.0969443	4.71724	-3.98029	0	r-0.15,0.6,0,0,0,0,0,0	p-0.147536,0.147536,0,0,0,0,0,0	Reflection	MirrorOptic	
24	☑	0.7	1.07	0.606218	-0.0969443	4.74886	-3.98725	0	r-0.15,0.6,0,0,0,0,0,0	p-0.147536,0.147536,0,0,0,0,0,0	Reflection	MirrorOptic	

Fig. 4.2 SolTrace stage definition for the solar oven receiver and mirror field

4.1.1.1 Ray independent study

An appropriate balance between simulation efficiency and ray-tracing accuracy can be obtained through a ray independence study. This study was carried out using different ray counts, ranging from 50,000 to 10,000,000 rays, and the resulting average flux on the absorber surface was compared for each case.

The results of the ray independence study are presented in Fig. 4.3. The findings indicate that beyond a ray count of 1,000,000, the variation in the average flux on the absorber plates becomes negligible. Table 4.1 summarizes the percentage differences in average flux on the absorber surface corresponding to each ray count.

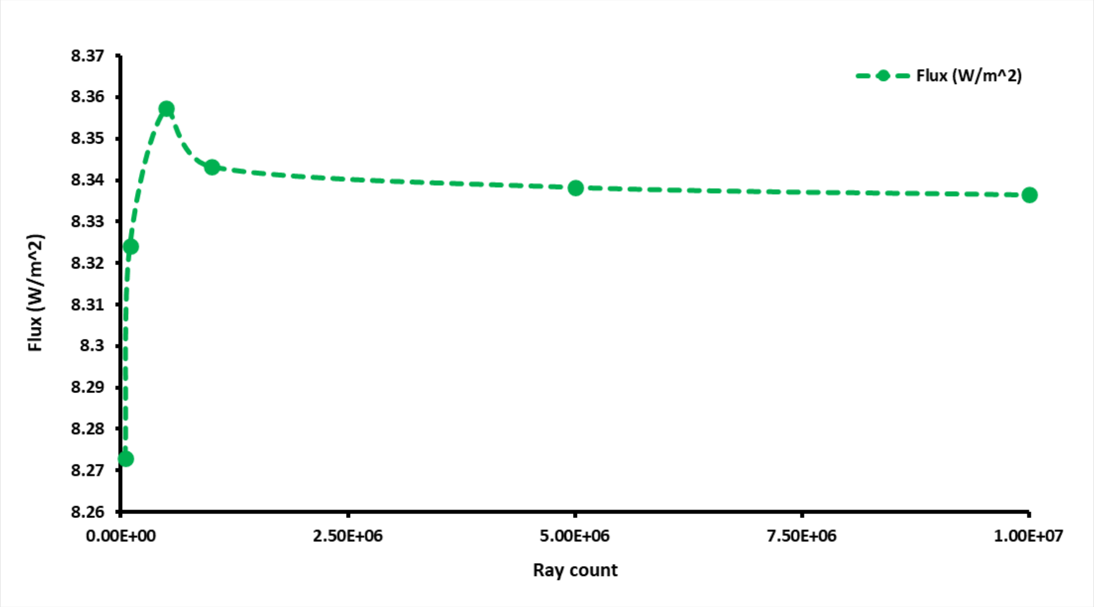

Fig. 4.3 Ray count with average absorber flux

The percentage difference after 5,000,000 ray count was found to be below 5% and the average flux became constant. The result on optical model presented in the next section was conducted using 10,000,000 rays and the ray tracing parameters applied in this model is shown in Fig.4.4.

Table 4.1 Result of average flux on absorber plate with ray count and percentage difference

Ray count	Average Flux (W/m^2)	Percentage difference (%)
50,000	8.27	-
100,000	8.32	0.612
500,000	8.35	0.397
1,000,000	8.34	0.167
5,000,000	8.34	0.059
10,000,000	8.34	0.021

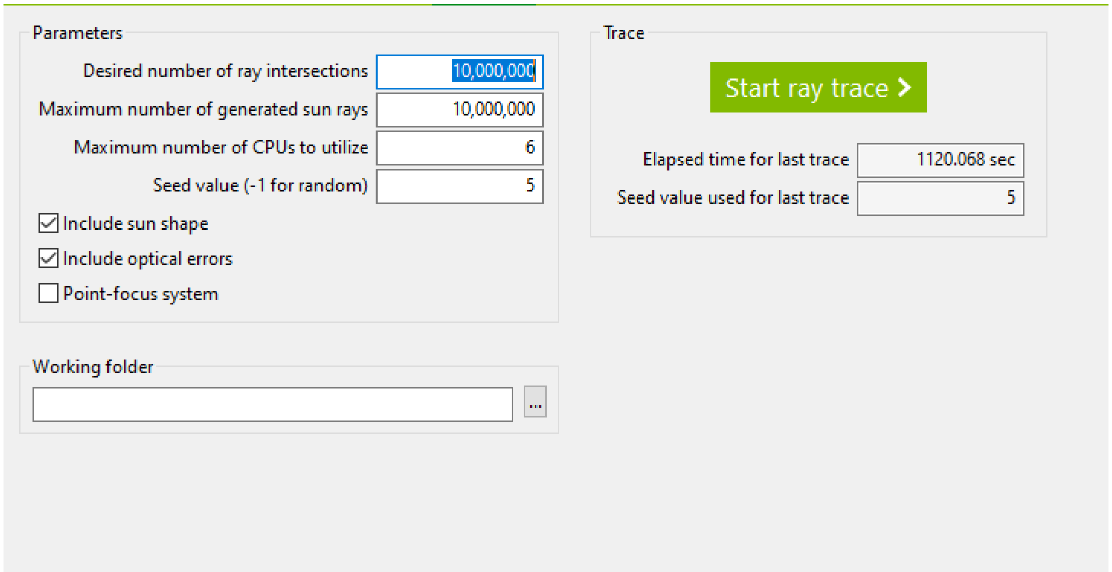

Desired number of ray intersections: 10,000,000
Maximum number of generated sun rays: 10,000,000
Maximum number of CPUs to utilize: 6
Seed value (-1 for random): 5
☑ Include sun shape
☑ Include optical errors
☐ Point-focus system
Elapsed time for last trace: 1120.068 sec
Seed value used for last trace: 5

Fig. 4.4 SolTrace ray tracing parameters applied in this study

4.1.2 Receiver Energy and Optical Efficiency

As described in Section 3.4.2.4, the simulations were performed using two aiming vector definition cases while maintaining the same concentration ratio and aperture area. Fig 4.5 illustrates the ray distribution and their interactions across the different stages of the system.

Solar rays originating from the modeled source (the sun) are first reflected by the mirror field (first stage). During this process, a portion of the incident energy is lost due to absorption and scattering before the rays are directed toward the solar oven receiver. The reflected rays then pass through the glass cover (second stage), where additional losses occur due to absorption and reflection. The transmitted rays subsequently reach the absorber plates (third stage), where they are absorbed and contribute to an increase in absorber temperature. The remaining rays that do not directly strike the absorber interact with the side walls (fourth stage), where they may either be absorbed or reflected back toward the absorber, contributing further to the overall energy captured.

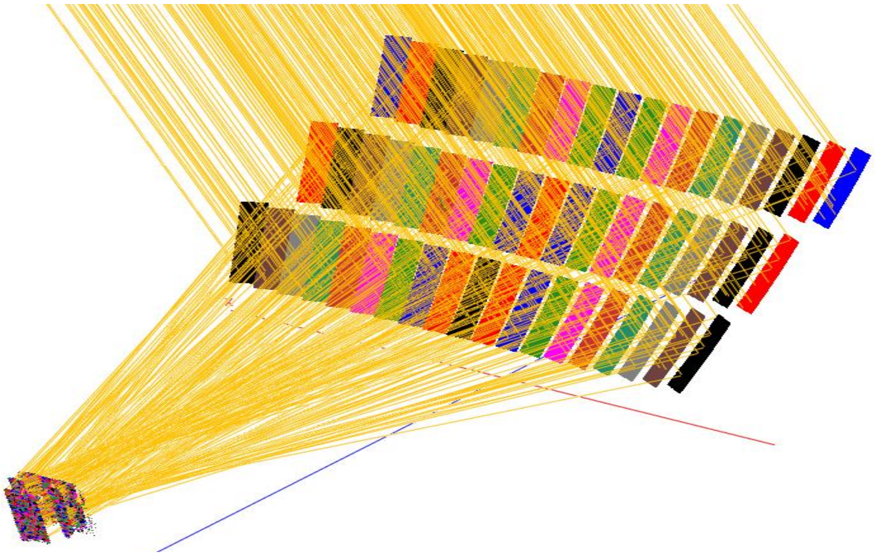

Fig.4.5 Ray distribution at different stages

Table 4.2 shows the optical performance and the power absorbed by the receiver for the two aiming vector definition cases. The results indicate that the absorbed power at the receiver is 1636.4 W for Case 1 and 2219 W for Case 2 (Table 4.2). This demonstrates that the use of a global aiming plane significantly enhances the total collected power compared to the plate-based aiming approach.

Table 4.2 Result of the optical model

Variable	Case 1	Case 2	Unit
DNI	1,000	1,000	W/m^2
Aperture area	5.13	5.13	m^2
Concentration ratio	35.53	35.53	-
Absorber power	1,636.39	2,219.08	W
Max. flux	99.63	147.03	kW/m^2
Intercept factor	41.74	57.4	%
Optical efficiency	36.16	49.72	%

The intercept factor of the system for the two aiming approaches is evaluated using Equ.28 and found to be 42% and 57% for case one and two respectively (Tabel.4.2). The result found is comparable with reported result between 46.16% to 61.05% for a receiver with cavity by Liu et al. [81]. Also the interception factor can be increase by modifying the receiver area and concentration ratio as shown in the Brooks et al. [82] study, where by modifying this two parameters the intercept factor above 80% was achieved.

The optical efficiency was computed for both cases, resulting in values of 36% and 50% for Case 1 and Case 2 respectively (Tabel.4.2). The results indicate that the strategy applied in Case 2 improved the optical efficiency by increasing the intercept factor. The result found in this study is in line with the values reported in Azmi et al. [83], where optical efficiency was between 21.6% to 38.6% and in Morin et al. [84] between 40 to 60% for Linear Fresnel system[85][86]. Also in Brooks et al. [82] for glass shielded receiver an optical efficiency of 55.3% was reported and similarly an optical efficiency between 42.89 % to 26.98 % was reported by Said et al. [48].

4.1.3 Surface Heat Flux Characteristics and Flux Distribution

The results presented in Table 4.2 indicate maximum flux values of 99.63 kW/m² and 147.03 kW/m² for Case 1 and Case 2 respectively. This demonstrates that the aiming strategy applied in Case 2 resulted in higher flux and power on the absorber plates. The corresponding flux and power distributions on the absorber plates are illustrated in Fig. 4.6 and Fig. 4.7, respectively.

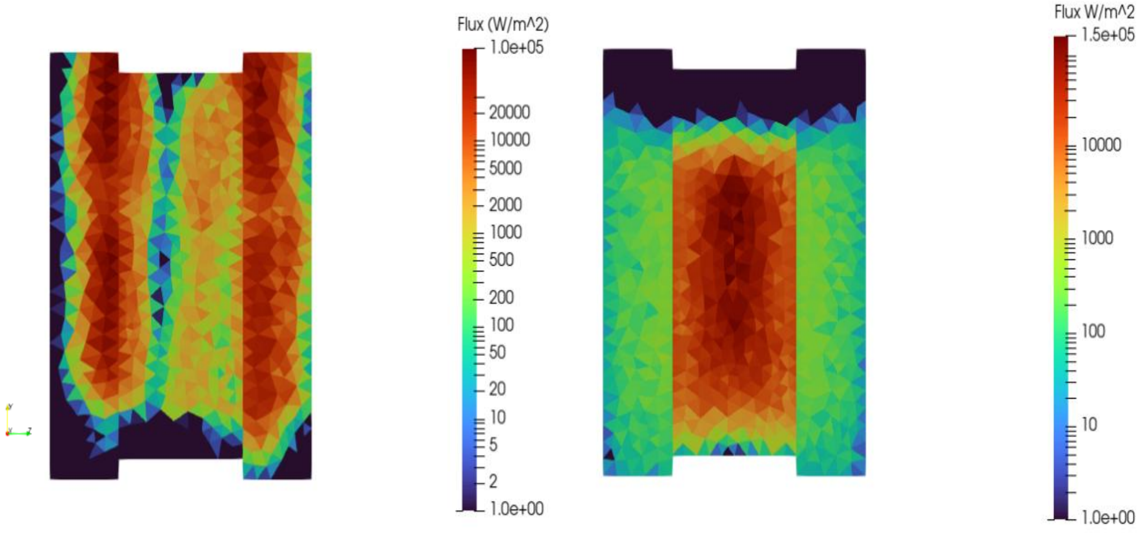

Fig. 4.6 Flux distribution through the absorber plates elements for case one (left) and case two (right)

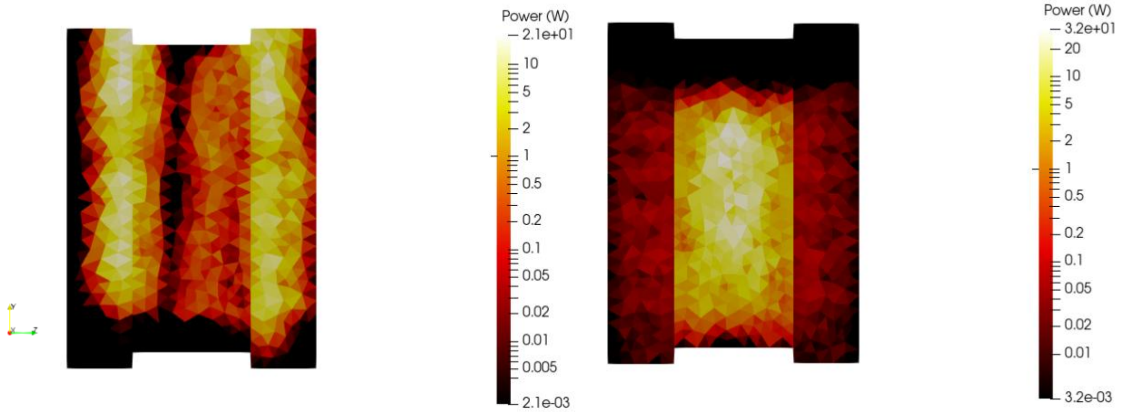

Fig.4.7 Power distribution through the absorber plate elements for case one (left) and case two (right)

The results indicate that under the global plane aiming approach, the peak flux is concentrated on the middle plate of the absorber, whereas the plate based aiming approach distributes the flux more evenly. Since localized high flux concentrations are a primary cause of hotspot formation, the reduced peak flux observed in case 1 suggests that the plate based aiming strategy can effectively mitigate hotspot development, a common challenge in linear Fresnel solar systems, thereby eliminating the need for specialized cooling systems and the associated costs. Additionally, case 1 enhances flux uniformity across the entire absorber surface.

4.1.4 Thermal simulation result

The simulation in Ansys Fluent was performed using the absorber heat flux computed in SolTrace for each element of the absorber plates. To ensure accurate mapping, the heat flux on the absorber elements was transferred using the same transformation matrix applied during the mesh preparation for the SolTrace model, allowing proper alignment of the elements in Ansys Fluent for thermal analysis. This mapping was implemented using the user defined function (UDF) tool in Ansys Fluent, and the code used to define the absorber flux is provided in Appendix E

Fig.4.8 shows convergence history of the area weighted average temperature of the monitored mid plane temperature of the solar oven. The simulation was run until the residual and monitored temperature became below the convergence criteria. The result shows that the change in temperature for the consecutive iteration became under 0.027 % and it shows that the solution have reached the steady state condition.

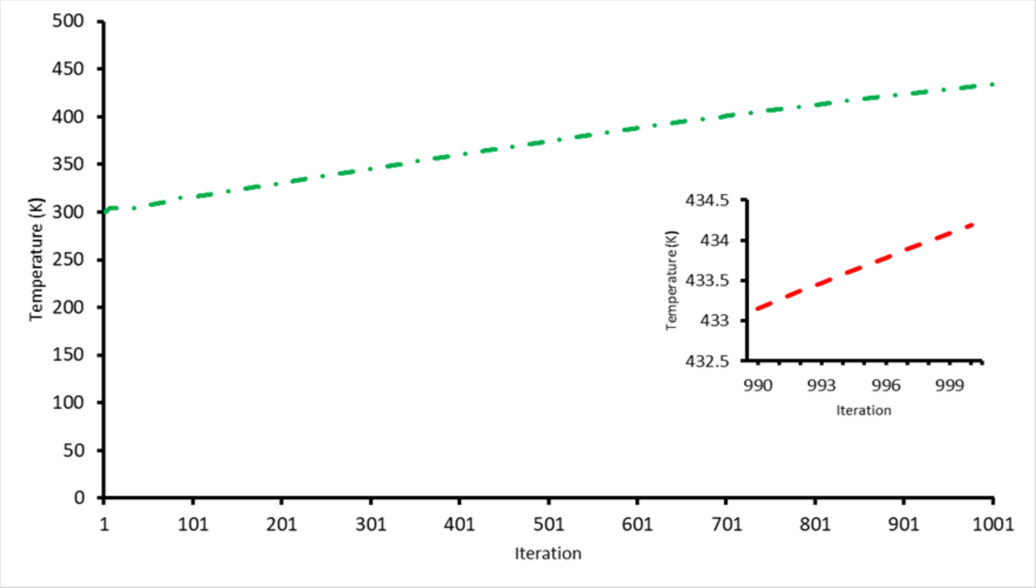

Fig.4.8 Simulation convergence control through area weighted average temperature

The temperature contour at the mid-plane of the model is shown in Fig. 4.9. Temperatures at different locations within the oven range from 425 to 443 K. Additionally, the top tray exhibits higher temperatures compared to the bottom trays which was also observed in the experimental results recorded on 5/25/2025.

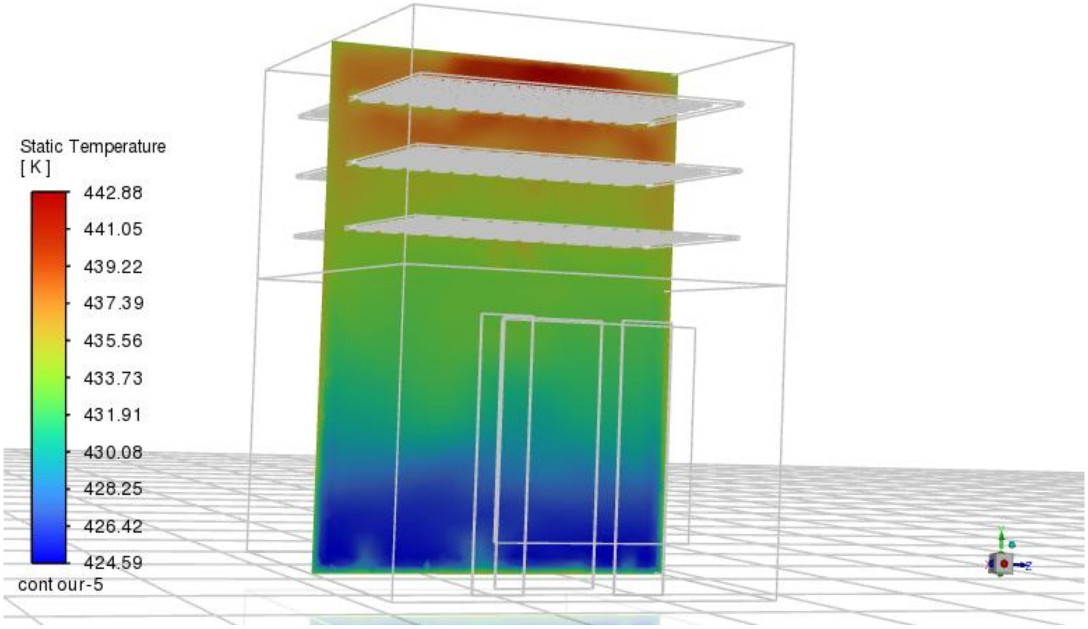

Fig.4.9 Temperature contour at the mid plane of the solar oven

As a result of the mapped flux distribution, the absorber surface heats rapidly, with temperatures reaching up to 555 K in the hotspot regions, while the area-weighted average temperature is approximately 440 K, as shown in Fig. 4.10. These results indicate that the solar oven operates within safe thermal limits, remaining below the maximum allowable operating temperature of the steel used for the absorber plates.

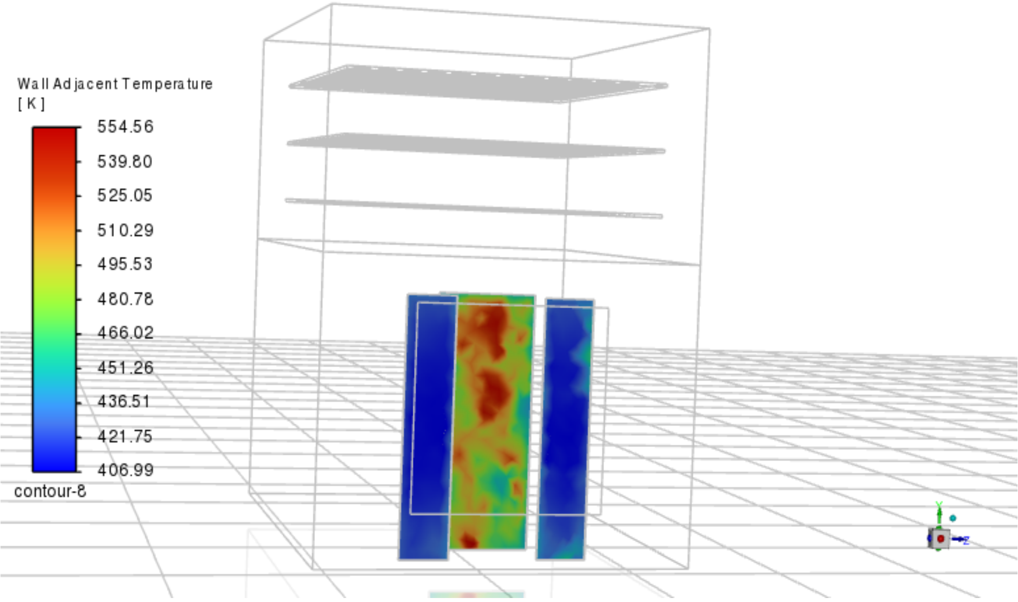

Fig. 4.10 Wall temperature contour of the absorber plates

The velocity vector field at the mid-plane of the model is shown in Fig. 4.11. The results show that near the bottom region, where the baking air is heated, the airflow is relatively weak and the velocity is about 0.05 m/s. As the air rises due to natural convection it gains acceleration and the velocity increases to about 0.21 m/s at the top of the baking cavity. The velocity vectors also show that when the air reaches the baking trays and passes through the porous tray supports and side wall gaps the flow becomes disturbed and turbulence develops. This behavior enhances convective heat transfer and improves air mixing inside the cavity. The velocity values obtained in this study are comparable with those reported in previous studies where velocities ranged from 0.2 to 1.5 m/s [87] and 0.17 to 0.6 [88].

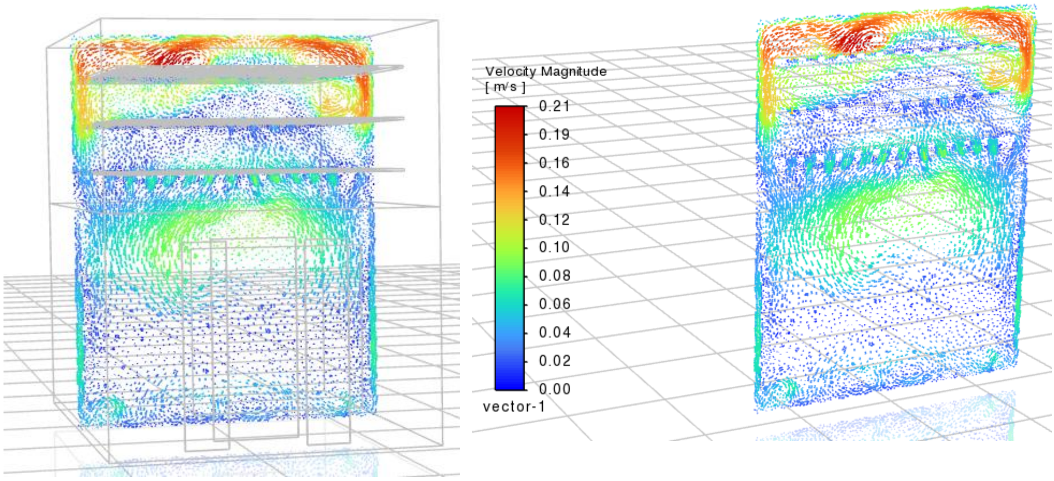

Fig. 4.11 Velocity vector plot at the mid plane of the solar baking chamber

The contour of density variation for the air inside the solar oven is shown in Fig.4.12 (left). The result shows that the air density varies between 0.8 to 0.83 kg/m^3 within the baking chamber. Even though the air temperature at the bottom of the baking oven is higher and increases at the top of the baking compartment, similarly the density of the air is expected to be lower at the bottom and higher at the top of the baking compartment. However, in our case the air is modeled as an ideal gas in which the density of the air is dependent on both temperature and pressure. The result of the density variation can be explained as follows, the air at the bottom experience a higher hydrostatic pressure (Fig.4.12 (right)), because of the weight of the air column above it and this higher pressure counteracts the reducing effect of temperature on the density of air at the bottom and keeps the air density at slightly higher value of 0.83 kg/m^3 compared to the air at the top 0.8 kg/m^3.

At the top of the baking chamber the pressure is lower and adding to this, a higher air temperature at the top resulted in a lower density of the air due to the combined effect of both temperature and pressure. The density variation shown in the result is consistent with the ideal gas law and both buoyancy and hydrostatic balance ensures that denser air remains near the bottom. The applied ideal gas model for the density of the air allowed us to capturing the buoyancy effect on the air distribution (Fig.4.12).

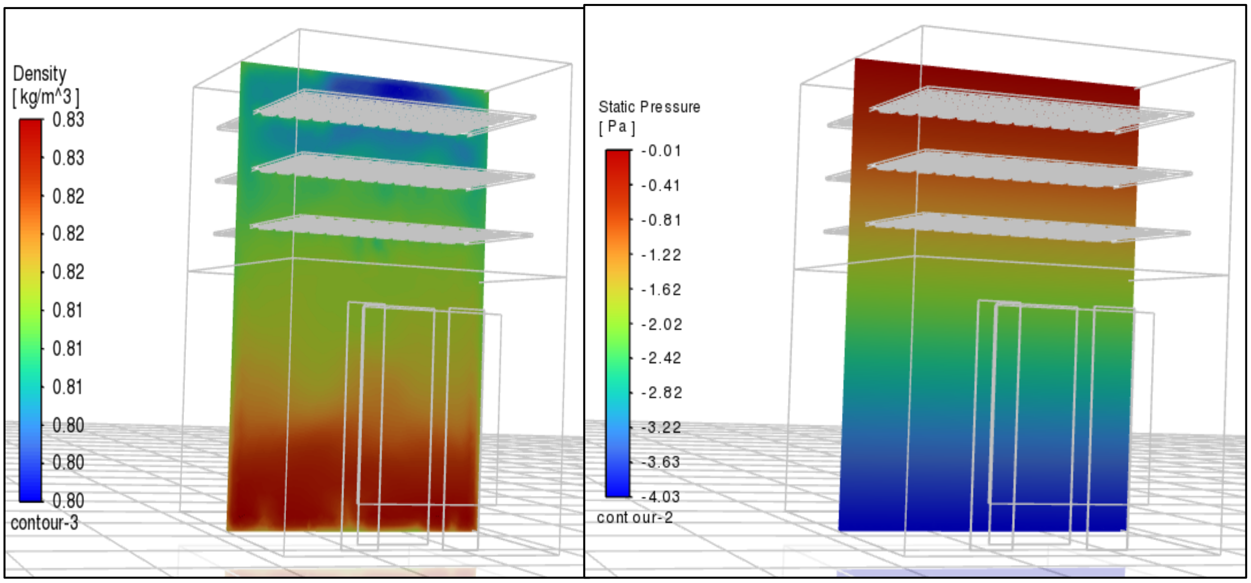

Fig. 4.12 Density variation (left-side) and pressure variation (right-side) of air inside the solar oven

The pressure distribution shown in the Fig.4.12 (b) describes that the air pressure around the baking tray is almost uniform and this helps to maintain a uniform flow velocity around the baking trays which is important for uniform baking of the bread loaf at different trays. The static pressure of the air at the bottom was found to be -4.03 Pa and at the top it was -0.01 Pa relative to the reference. This pressure drop of 4 Pa can be explained by the perforated tray that results a pressure loss due to friction.

The turbulent intensity of the air is shown in Fig.4.13 below. The result shows the upward flow of air from the absorber into the upper baking compartment due to buoyancy enhanced by turbulent mixing. It can be seen that near the absorber, a thin boundary layer forms where conduction and convective transport couples and further above the absorber the flow became wider and accelerates toward the top of the cavity. Turbulence inside the solar oven increases the convective heat transfer coefficients on the absorber surface. The applied SST k–ω turbulent model resolved the hot air property inside the solar oven.

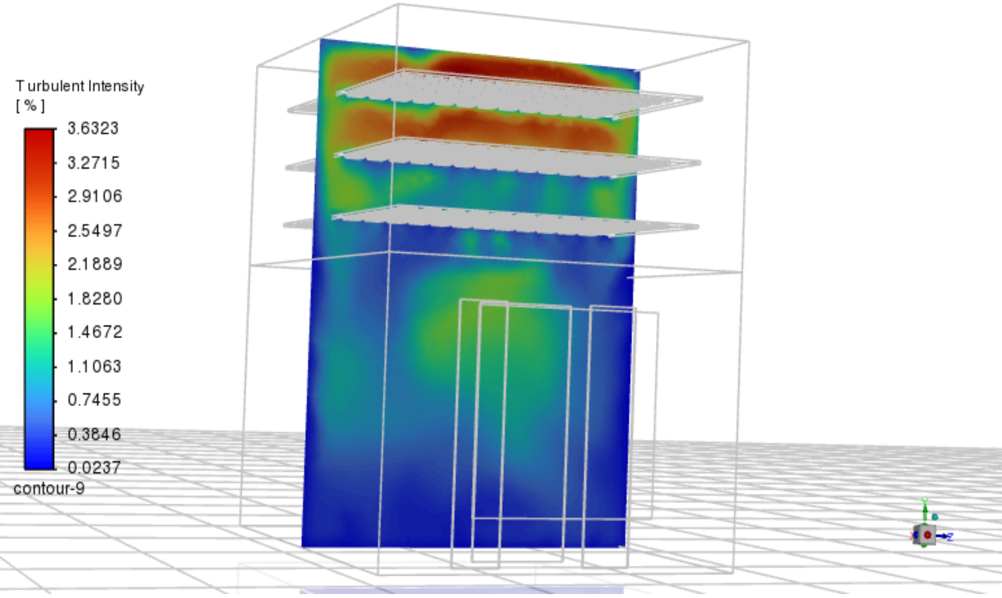

Fig.4.13 Turbulent intensity of the air inside the solar oven

4.2 Experimental Result

The experimental testing was conducted in the months of May and June 2024 on four different days, during which various data sets were collected. The no load experiment was conducted in May 20 and 25 and in June 4 whereas the load test was conducted on May 30.

The measured global horizontal irradiance (GHI) values for 5/25/2024, 5/30/2024 and 6/4/2024 were found comparability with the satellite data as shown in Fig.4.14 up to 4.16. Moreover, the solar radiation for 6/4/2024 is lower when compared to 5/25/2024 with a maximum and average radiation of 824 and 607 W/m^2 and 1187 and 1038 W/m^2 respectively for these two days.

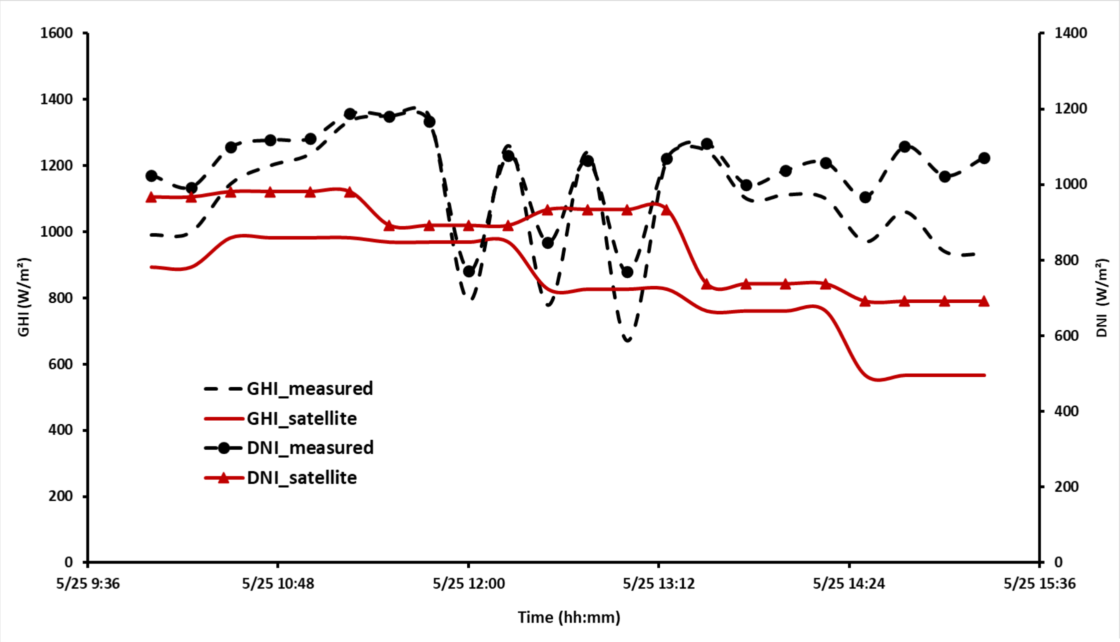

Fig.4.14 The measured and satellite global horizontal irradiance (GHI) and direct normal irradiance (DNI) for 5/25/2024

The direct normal irradiance for June 4, 2024 (Fig.4.16) exhibits a decreasing trend after reaching its peak at solar noon. In contrast, the irradiance on May 25, 2024 (Fig.4.14) remains relatively stable throughout the day, except around solar noon, where significant fluctuations are observed. These variations can be attributed to changes in cloud coverage during that period.

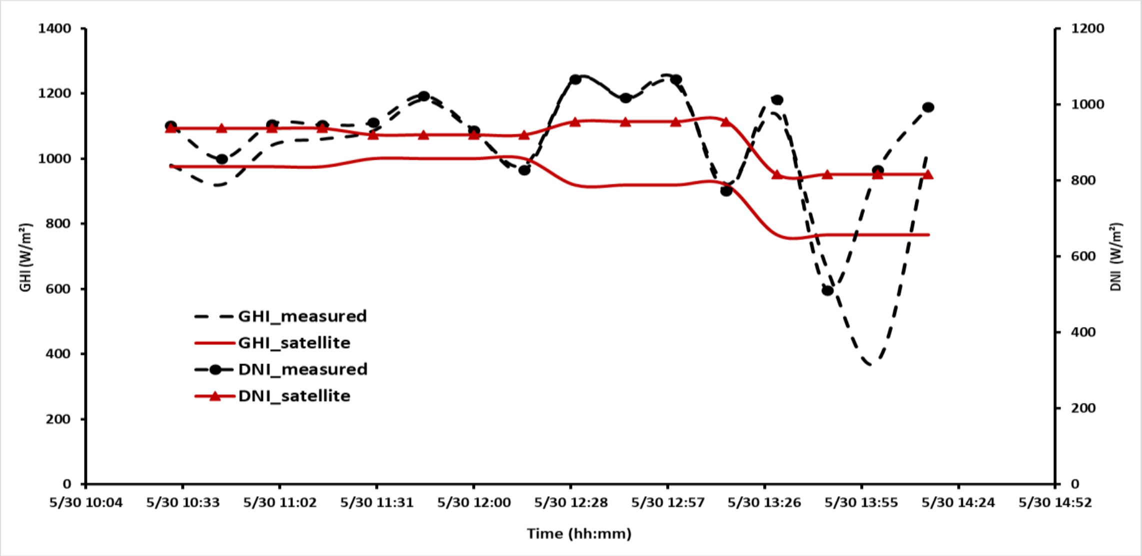

Fig.4.15 The measured and satellite global horizontal irradiance (GHI) and direct normal irradiance (DNI) for 5/30/2024

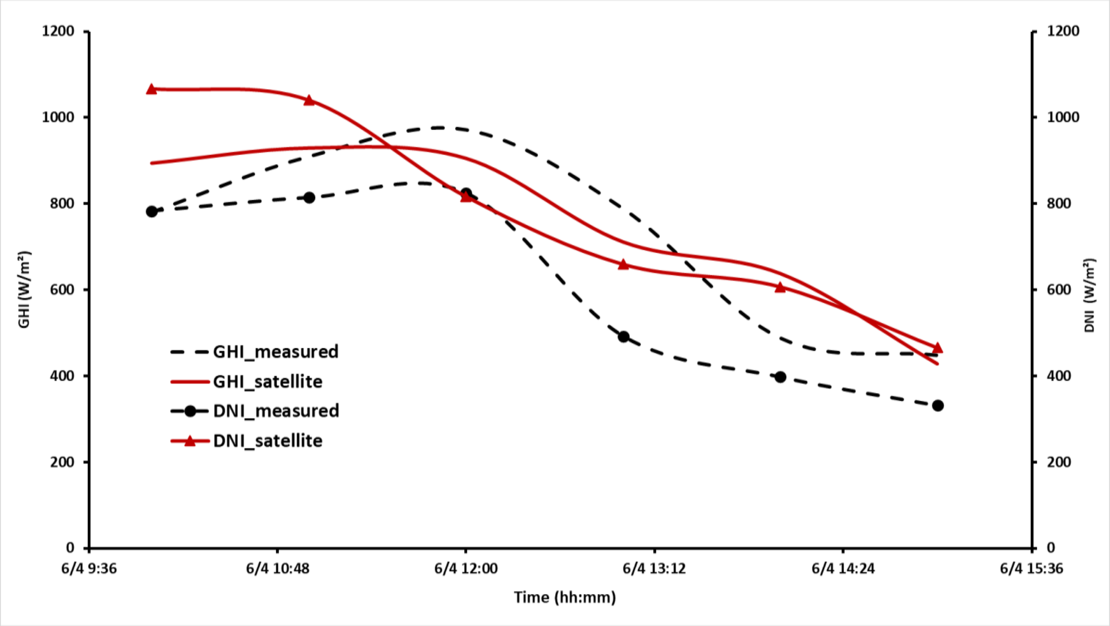

Fig.4.16 The measured and satellite global horizontal irradiance (GHI) and direct normal irradiance (DNI) for 6/4/2024

4.2.1 No load result

The temperature distribution through the solar oven trays is shown in the Fig.4.17 up to 4.19 for the no load experiment days of 5/20/2025, 5/25/2024 and 6/4/2024. The temperature change between baking trays shows similar pattern throughout the experimental period with relatively uniform distribution between trays. The result for day 6/4/2024 (Fig.4.19), a decreasing pattern after reaching its pick temperature at around noon and steadily decreases. Whereas for the other two no load cases, the tray temperature increases throughout the experiment as shown in Fig.4.17 and Fig.4.18. Also, in these two cases the temperature of the top tray was found to be higher than the bottom trays. That can be related to the buoyance effect where the high temperature air gets pushed by the lower air temperature due to the lower density of the high temperature air so that the higher air temperature which is found around the top trays in this study could be due to this effect. The temperature distribution over the baking trays follows similar pattern with the direct normal radiation which are shown in the Fig.4.14 and 4.16 for no load conditions.

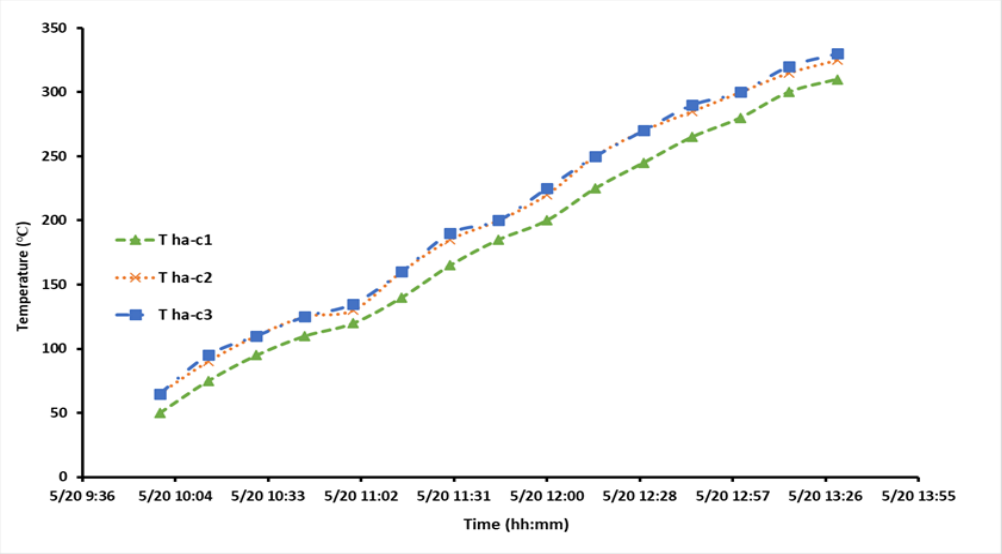

Fig.4.17 The measured air temperature over baking trays for the day of 5/20/2024 for no load condition

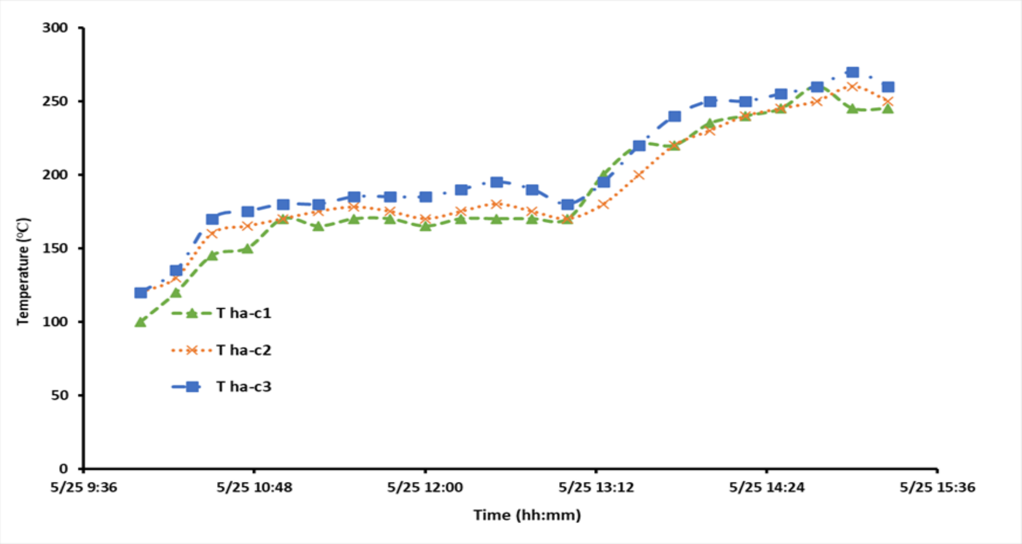

Fig.4.18 The measured air temperature over baking trays for the day of 5/25/2024 for no load condition

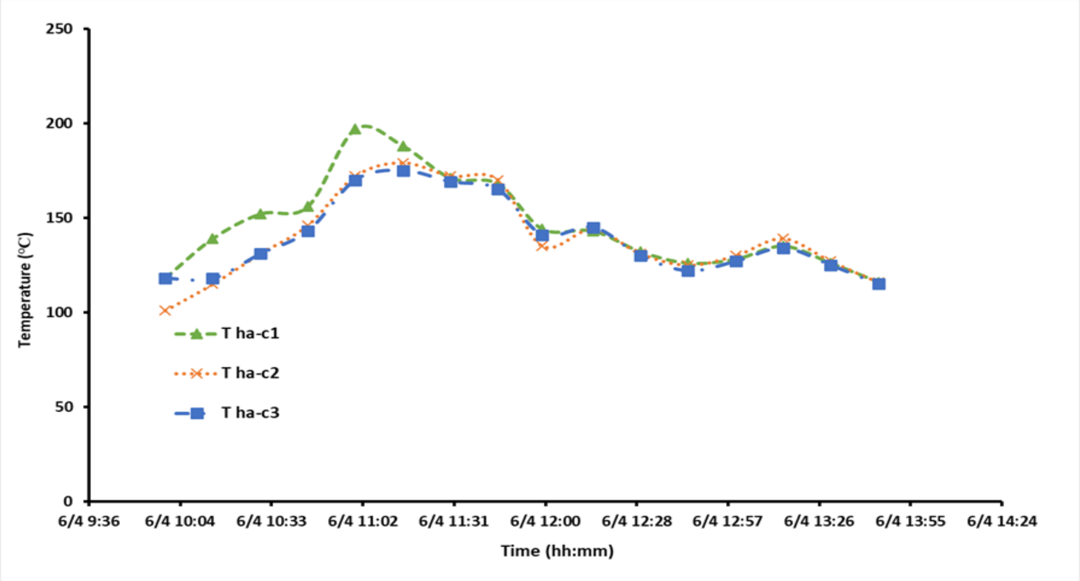

Fig. 4.19 The measured air temperature over baking trays for the day of 6/4/2024 for no load condition

The maximum, minimum, and average air temperatures above the baking trays are presented in Table 4.3. On May 20, 2024, the highest air temperature of 326 °C was recorded at the top tray, while the lowest temperature of 50 °C was observed at the bottom tray.

The temperature distribution among the trays shows that on May 20 and May 25, 2024, the top tray consistently exhibited higher temperatures than the middle and bottom trays. In contrast, on June 4, 2024, the bottom tray recorded the highest temperature, while the temperatures of the middle and top trays showed negligible differences.

Table 4.3 Baking chamber air temperature over the trays for no load experiment

	Air Temperature (^{0}C)		
	Maximum	Minimum	Average
Day	Bottom baking compartment (C1)		
5/20/2025	310	50	184.33
5/25/2025	260	100	188.40
6/4/2025	197	116	146.18
	Middle baking compartment (C2)		
5/20/2025	325	65	202
5/25/2025	260	120	191.72
6/4/2025	179	101	139.56
	Top baking compartment (C3)		
5/20/2025	330	65	204.33
5/25/2025	270	120	203.18
6/4/2025	175	115	139.25

The absorber temperature for 6/4/2024 with the solar radiation on that day is shown in Fig.4.120. The maximum and average temperature was found to be 330 ℃ and 256.7 ℃. The surface temperature of the absorber exhibits a comparable trend with the variation in solar radiation where it shows a higher value before solar noon and decreasing after this period.

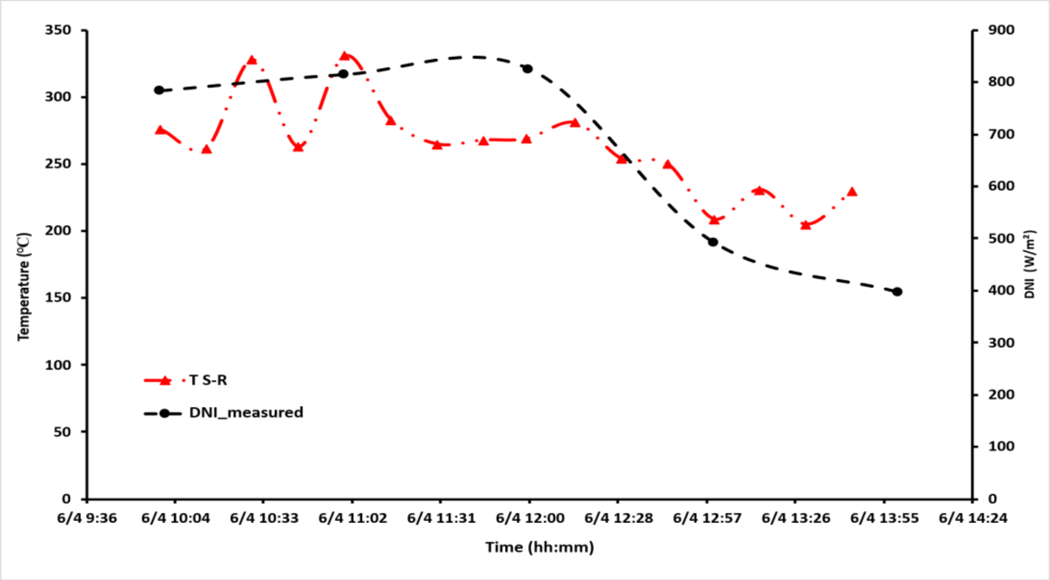

Fig.4.20 The absorber temperature and direct normal irradiance (DNI) for 6/4/2024 no load condition

When compared to the trays temperature, the absorber temperature remains consistently higher than the tray temperature. The higher temperature on the absorber plates of the solar oven is a direct consequence of the concentrated radiation which is directed toward the absorber from the mirror field. The result for the first figure of merit ($F1$) was evaluated and it was found to be 0.37.

The result from the simulation and experiment for the trays of the solar oven and the percentage difference is shown in Table 4.4. The result indicates that the simulation result was comparable with the result found from the experiment with percentage difference less than 5% in all trays of the solar oven. The simulation results were found to be in good agreement with the experimental measurements, demonstrating the reliability of the numerical model. Similar levels of agreement have been reported in previous studies on temperature distribution over baking trays, where comparisons between simulation and experimental results yielded an average absolute relative error of 3% [22] and 3.35% [45].

Table 4.4 Temperature of the trays from the simulation and experiment with the percentage error

Location	Experimental temperature (K)	Simulation temperature (K)	Percentage difference (%)
Bottom	438.15	433.67	1.02
Middle	443.15	434.19	2.02
Top	458.15	436.76	4.67

4.2.2 The load test

The load test was conducted using water and bread dough loaded in the solar oven. The result from the load test will be presented in this section. The result from the water boiling test is shown in Fig.4.21 and it shows the water temperature with the oven air temperature and the direct normal irradiance for the day of 5/31/2024. The result shows that the water temperature for the first 20 minutes was rising and after that, the change in the temperature of the water stabilized. The water temperature gets to 98 ℃ of the standard reference in 32 min from the ambient temperature of 26 ℃. The second figure of merit ($F2$) from the water boiling test was found to be 0.67.

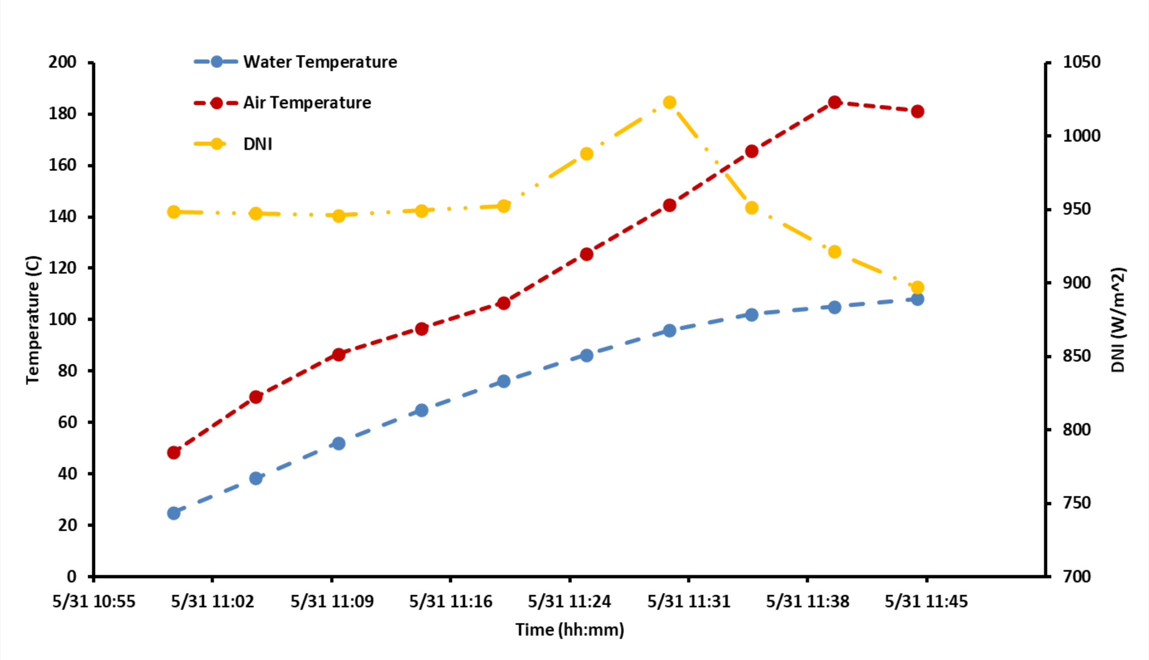

Fig. 4.21 Water and oven air temperature with direct normal irradiance (DNI) for 5/31/2024 water boiling test in load condition

The result from the linear fit of the $\dot{Q}''/I_b$ vs. $(T_{wm} - T_a)/I_b$is show in Fig.4.22. From the linear fit of the result, the value of $F'\eta_O$ and $F'U_L/CR_m$ were found to be 0.31 and 1.54 respectively. From these values the Opto-thermal ratio (COR) is found to be 0.2. The result was comparable with reported values for $F'U_L/CR_m$, $F'\eta_O$ and COR of 2.26, 0.348 and 0.155 respectively for solar concentrating type cooker [78].

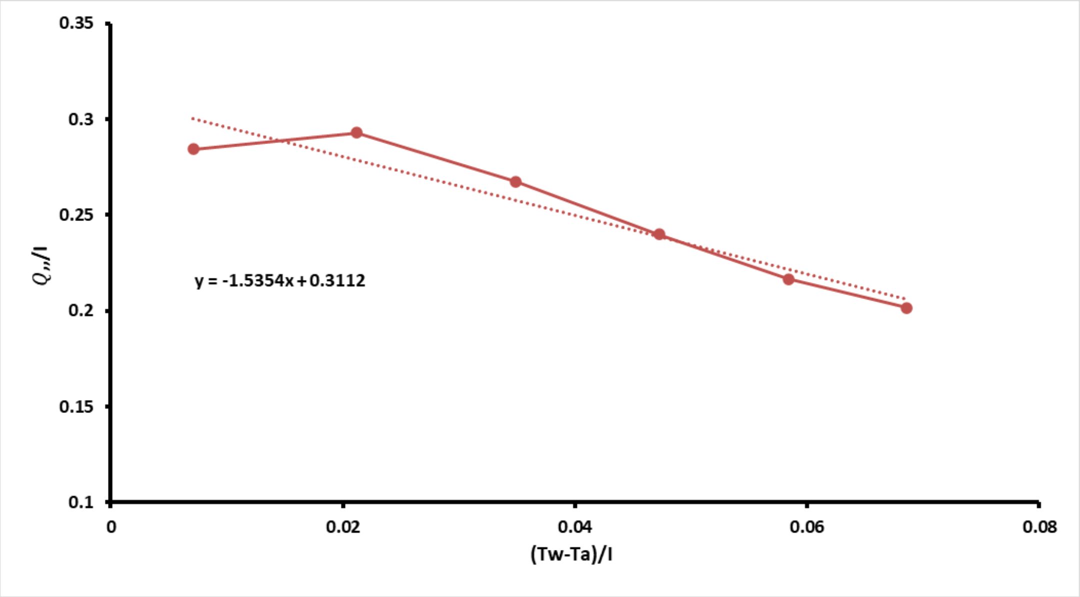

Fig. 4.22 The linear fit of $\dot{Q}''/I_b$ vs. $(T_{wm} - T_a)/I_b$

The bread load test was conducted in 5/30/2024 and the result is presented in Fig.4.23. The temperature distribution over the baking trays shows a uniform distribution almost through the experimental period and only showing small variation at the end of the backing period. Also, it was found to be above the ambient temperature. It was also observed from the load experiment that the maximum and average temperature over the trays was found to be between 231.3 ℃ to 249.8 ℃ and 201.5 to 205.85 ℃ respectively, over the entire load testing period. Which shows that the system have provided the required baking temperature which is reported to be between 180 to 230 ℃ [35][26][41]. The absorber temperature (T_{S-R}) was found to be above the tray temperature throughout the experiment. Moreover, the result shows that the tray temperature shows similar pattern with the absorber temperature.

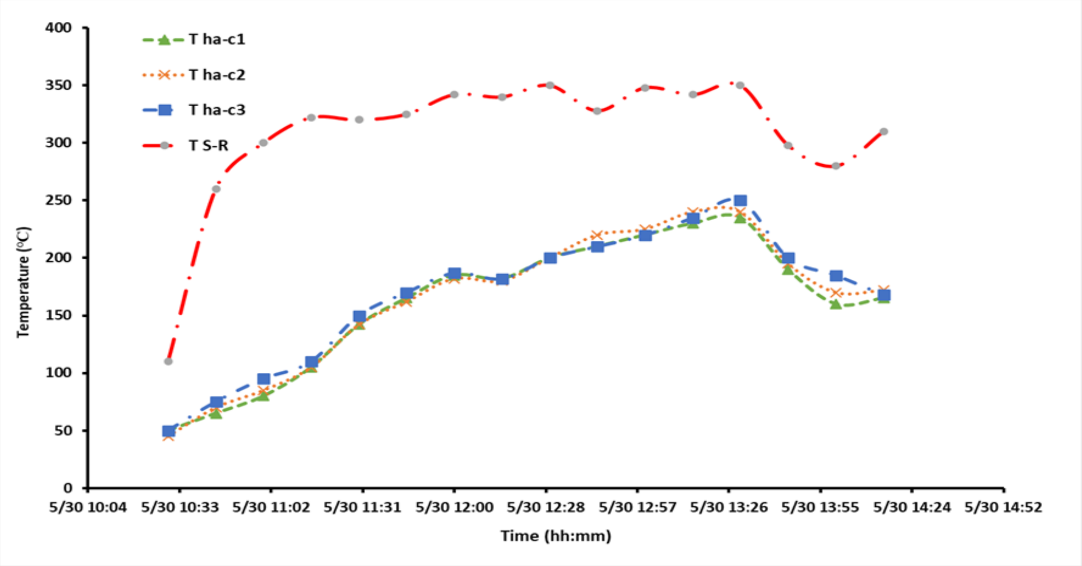

Fig.4.23 The measured tray air temperature with the absorber temperature for the day of 5/30/2024 for load condition

The bread crumb temperature (T_{cb}) is also presented in Fig.4.24, where it shows the crumb temperature was lower than the air over the tray. The lower temperature the crumb shows the direction of the heat and mass transfer. Also, after only 15 min of baking, the temperature of the core has reached 65 ℃, where it was reported a dough started to change into a solidified crumb state between 60 ℃ to 85 ℃ [24]. The system efficiency (η_{sys}) of the solar oven was calculated using the average specific heat of the dough (2153.1 J/℃.Kg) a total mass of 9.2 kg bread dough and it was found to be 36 %. To bake a 9.2 kg of bread dough, a total baking power of 1.18 kW was required with final mass of 7.5 kg in 1 hour and 10 minutes.

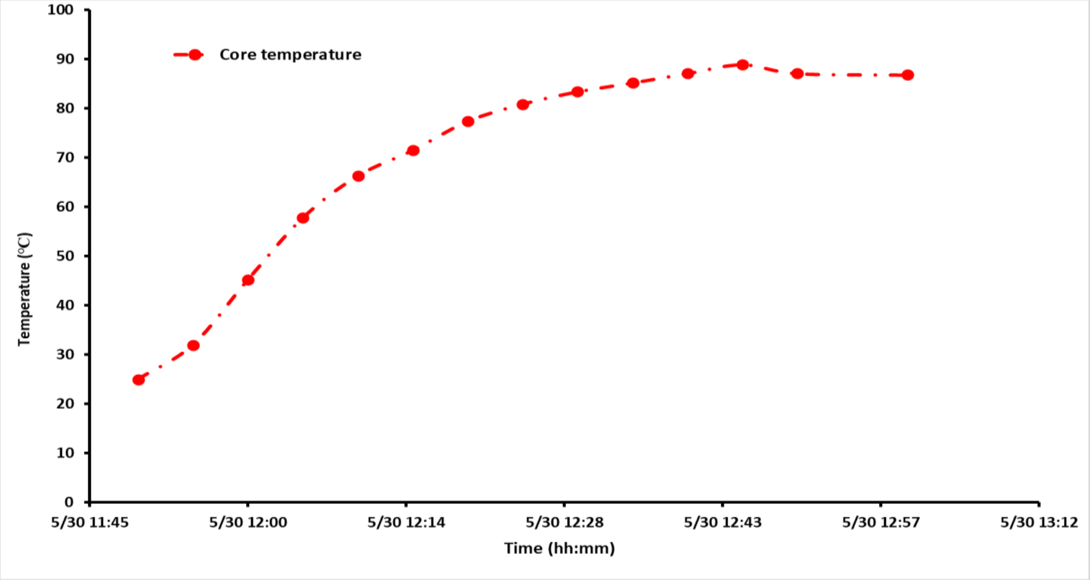

Fig.4.24 Bread crumb temperature

Fig 4.25 illustrates the baked bread obtained at the end of the baking test, confirming that the achieved thermal conditions were sufficient to produce properly baked bread using the LFPMR-integrated solar baking oven.

Fig. 4.25 Baking process and baked bread texture

Overall, the load test results clearly demonstrate the effective thermal and baking performance of the LFPMR-integrated solar baking oven under real operating conditions. The water boiling test confirmed a rapid temperature rise to near-boiling conditions within a relatively short time, yielding a second figure of merit and opto-thermal parameters that are comparable to values reported for similar concentrating solar cookers. The bread load test further verified the oven’s practical applicability, showing a nearly uniform temperature distribution across the baking trays and sustained temperatures well within the required baking range. The observed thermal relationship between absorber, tray, and crumb temperatures confirms efficient heat transfer into the dough, enabling proper phase transformation of the crumb within a relatively short baking duration. Moreover, the achieved system efficiency of 36% and the ability to bake 9.2 kg of bread dough within 70 minutes highlight the oven’s capability to deliver sufficient and stable thermal power for commercial-scale baking. These results collectively validate the suitability of the developed solar baking oven for reliable and efficient solar-based bread production.

Chapter 5

Conclusion and Recommendations

5.1 Conclusion

This study investigated the modeling, simulation, construction of prototype, and experimental evaluation of a Linear Fresnel Parabolic Mirror Reflector (LFPMR) integrated solar baking oven with the objective of assessing its optical, thermal, and baking performance for sustainable bread production. Both numerical simulations and experimental investigations were conducted to validate the proposed system under real operating conditions.

Optical simulations carried out using SolTrace demonstrated that the aiming strategy plays a critical role in enhancing the optical performance of the LFPMR system. The global aiming plane approach resulted in a significantly higher absorbed power (2219 W) and optical efficiency (49.7%) compared to the plate-based aiming method, primarily due to an increased intercept factor. However, the plate-based aiming approach provided improved flux uniformity and reduced peak flux levels, which is advantageous for mitigating hotspot formation on the absorber surface. These results confirm that a trade-off exists between maximizing optical efficiency and ensuring thermal uniformity, and that the selected aiming strategy should be aligned with system safety and operational requirements.

Thermal simulations conducted using ANSYS Fluent, with absorber heat flux mapped from the optical model, showed good convergence and stable steady-state behavior. The predicted temperature distribution within the baking chamber ranged between 425 K and 443 K, while the absorber surface reached a maximum temperature of approximately 555 K, remaining within safe material limits. The simulated airflow patterns revealed buoyancy-driven natural convection enhanced by turbulence near the baking trays, which promoted effective air mixing and uniform heat distribution. The predicted velocity, pressure, and density distributions were consistent with the ideal gas assumption and aligned well with values reported in similar solar thermal systems.

Experimental no-load tests confirmed that the solar oven is capable of achieving and sustaining high internal temperatures, with tray air temperatures exceeding 300 °C under favorable solar conditions. The temperature variation among trays followed similar trends to the direct normal irradiance, and buoyancy effects resulted in slightly higher temperatures at the upper trays. A close agreement between simulated and experimental tray temperatures was achieved, with percentage differences below 5%, validating the accuracy and reliability of the developed numerical model.

Load tests using water and bread dough further demonstrated the practical baking capability of the system. The water boiling test showed that water temperature reached 98 °C of the standard reference within 32 minutes, yielding a second figure of merit of 0.67 and opto-thermal performance parameters comparable to those reported for concentrating solar cookers. During the bread baking test, the oven maintained tray temperatures between 201.5 °C and 249.8 °C, which fall within the standard bread baking temperature range. The absorber temperature consistently remained higher than the tray temperatures, confirming effective heat transfer from the receiver to the baking chamber.

The bread crumb temperature results indicated rapid internal heating, with the dough core reaching 65 °C within 15 minutes, marking the onset of starch gelatinization and crumb formation. The system achieved an overall efficiency of 36% and successfully baked 9.2 kg of bread dough within 1 hour and 10 minutes. The quality of the baked bread further confirmed that the thermal conditions provided by the LFPMR-integrated solar oven were sufficient for proper baking.

Overall, the combined simulation and experimental results validate the technical feasibility, thermal reliability, and practical applicability of the developed LFPMR-integrated solar baking oven. The system demonstrates strong potential as a sustainable alternative to conventional fossil-fuel-based baking technologies, particularly in regions with high solar resource availability.

5.2 Recommendations

Based on the observations made during this study, the following recommendations are given to improve the system's performance.

1. In this study, the mirror field configuration, receiver geometry, and aiming strategies were selected based on predefined design constraints. However, further optimization of these parameters could significantly enhance optical efficiency and improve flux uniformity across the absorber surface. Therefore, additional studies focusing on optimizing the optical configuration are recommended.
2. The thermal performance of the system was evaluated without the inclusion of thermal energy storage. Although satisfactory baking temperatures were achieved, incorporating thermal storage materials, such as phase change materials (PCMs), could help stabilize temperature fluctuations and extend baking operation during transient solar conditions. Hence, the integration of thermal storage systems should be studied.
3. The insulation materials and heat loss mechanisms of the oven enclosure were not extensively optimized in this study. Since thermal losses directly affect system efficiency and baking performance, future work should focus on minimizing heat losses through the oven glazing.
4. The system was operated without an automated solar tracking mechanism. While acceptable performance was obtained under manual alignment, the integration of low-cost solar tracking systems could improve solar concentration and maintain higher efficiency throughout the day. Therefore, the feasibility of automated tracking should be explored.
5. The experimental investigation was limited to short-term testing under specific weather conditions. Long-term field testing under diverse climatic conditions is recommended to evaluate the durability, reliability, and operational stability of the system over extended periods.
6. This study focused primarily on the technical performance of the system, without a detailed socio-economic analysis. Future research should assess the economic

feasibility, market potential and social impacts of deploying the system, particularly in rural where clean cooking solutions are most needed.

7. The system was developed at a prototype scale. To support broader adoption, further work is required to evaluate scalability, manufacturability, and commercialization potential for application in small-scale bakeries and community-based enterprises.
8. The performance of the LFPMR-based system was not compared with other solar concentrator technologies. Comparative studies involving parabolic troughs, dish concentrators, and compound parabolic concentrators (CPCs) are recommended to assess relative performance, cost effectiveness, and suitability for baking applications.

Reference

[1] A. Kumar, A. Karn, C. McGregor, and V. P. Singh, “A critical analysis of paradigm shifts from domestic solar cooking to institutional solar cooking technologies,” *Renew. Sustain. Energy Rev.*, vol. 218, no. May, p. 115840, 2025, doi: 10.1016/j.rser.2025.115840.

[2] G. Bensch, M. Grimm, and J. Peters, “Why do households forego high returns from technology adoption? Evidence from improved cooking stoves in Burkina Faso,” *J. Econ. Behav. Organ.*, vol. 116, pp. 187–205, Aug. 2015, doi: 10.1016/j.jebo.2015.04.023.

[3] F. Odoi-Yorke, B. Baah, and R. Opoku, “Scientific mapping of experimental research on solar cookers: Global trends, evolution, and future directions,” *Sol. Energy Adv.*, vol. 5, no. January, p. 100093, 2025, doi: 10.1016/j.seja.2025.100093.

[4] A. C. Araújo, A. Gomes, P. M. Rodrigues, and C. L. M. Silva, “Advancing solar cooking: Challenges, innovations, and future directions,” *Energy Nexus*, vol. 19, no. August, p. 100521, Sep. 2025, doi: 10.1016/j.nexus.2025.100521.

[5] FAO, *The State of the World’s Forests 2020*. FAO and UNEP, 2020. doi: 10.4060/ca8642en.

[6] N. E. Benti *et al.*, “The current status, challenges and prospects of using biomass energy in Ethiopia,” *Biotechnol. Biofuels*, vol. 14, no. 1, pp. 1–24, 2021, doi: 10.1186/s13068-021-02060-3.

[7] A. K. Quinn *et al.*, “An analysis of efforts to scale up clean household energy for cooking around the world,” *Energy Sustain. Dev.*, vol. 46, pp. 1–10, 2018, doi: 10.1016/j.esd.2018.06.011.

[8] K. Lentswe, A. Mawire, P. Owusu, and A. Shobo, “A review of parabolic solar cookers with thermal energy storage,” *Heliyon*, vol. 7, no. 10, p. e08226, 2021, doi: 10.1016/j.heliyon.2021.e08226.

[9] T. J. Hager and R. Morawicki, “Energy consumption during cooking in the residential sector of developed nations: A review,” *Food Policy*, vol. 40, pp. 54–63, 2013, doi: 10.1016/j.foodpol.2013.02.003.

[10] E. Cuce and P. M. Cuce, “A comprehensive review on solar cookers,” *Appl. Energy*, vol. 102, pp. 1399–1421, 2013, doi: 10.1016/j.apenergy.2012.09.002.

[11] A. Herez, M. Ramadan, and M. Khaled, “Review on solar cooker systems: Economic and environmental study for different Lebanese scenarios,” *Renew. Sustain. Energy Rev.*, vol. 81, no. February 2017, pp. 421–432, 2018, doi: 10.1016/j.rser.2017.08.021.

[12] S. Indora and T. C. Kandpal, “Institutional cooking with solar energy: A review,” *Renew. Sustain. Energy Rev.*, vol. 84, no. October 2017, pp. 131–154, 2018, doi: 10.1016/j.rser.2017.12.001.

[13] G. Guimbretière, B. Pillot, C. Révillion, C. Mathiak, and R. Authier, “Territorial solar baking potential: A socio-technical analysis for planning the sustainable energy transition of the bakery world,” *Clean. Responsible Consum.*, vol. 17, no. April, p. 100276, 2025, doi: 10.1016/j.clrc.2025.100276.

[14] B. A. Mekonnen, K. W. Liyew, and M. T. Tigabu, “Solar cooking in Ethiopia: Experimental testing and performance evaluation of SK14 solar cooker,” *Case Stud. Therm. Eng.*, vol. 22, no. October, p. 100766, 2020, doi: 10.1016/j.csite.2020.100766.

[15] A. D. Hailu and D. K. Kumsa, “Ethiopia renewable energy potentials and current state,” *AIMS Energy*, vol. 9, no. 1, pp. 1–14, 2020, doi: 10.3934/ENERGY.2021001.

[16] Q. J. Abdul-Ghafoor, S. H. Abed, S. A. Kadhim, and M. A. Al-Maliki, “Experimental and numerical study of a linear Fresnel solar collector attached with dual axis tracking system,” *Results Eng.*, vol. 23, no. May, p. 102543, 2024, doi: 10.1016/j.rineng.2024.102543.

[17] W. T. Xie, Y. J. Dai, R. Z. Wang, and K. Sumathy, “Concentrated solar energy applications using Fresnel lenses: A review,” *Renew. Sustain. Energy Rev.*, vol. 15, no. 6, pp. 2588–2606, 2011, doi: 10.1016/j.rser.2011.03.031.

[18] A. Sarangi, A. Sarangi, S. S. Sahoo, J. Nayak, and R. K. Mallik, “Advancements and global perspectives in solar cooking technology: A comprehensive review,” *Energy Nexus*, vol. 13, no. December 2023, p. 100266, 2024, doi: 10.1016/j.nexus.2023.100266.

[19] R. Khatri, R. Goyal, and R. K. Sharma, “Advances in the developments of solar cooker for

sustainable development: A comprehensive review," *Renew. Sustain. Energy Rev.*, vol. 145, no. May, p. 111166, 2021, doi: 10.1016/j.rser.2021.111166.

[20] S. Talbi, I. Atmane, N. El Moussaoui, K. Kassmi, O. Deblecker, and N. Bachiri, "Thermal Modeling of Photovoltaic Ovens and Hotplates," in *Sustainable Entrepreneurship, Renewable Energy-Based Projects, and Digitalization*, no. Mohan 2018, 2020, pp. 245–259. doi: 10.1201/9781003097921-13.

[21] M. M. Adane, G. D. Alene, S. T. Mereta, and K. L. Wanyonyi, "Facilitators and barriers to improved cookstove adoption: a community-based cross-sectional study in Northwest Ethiopia," *Environ. Health Prev. Med.*, vol. 25, no. 1, p. 14, 2020, doi: 10.1186/s12199-020-00851-y.

[22] R. Ouqazzamar *et al.*, "Numerical investigation of Scheffler parabolic solar ovens: thermal performance and bread baking application," *Therm. Sci. Eng. Prog.*, vol. 69, no. December 2025, p. 104479, Jan. 2026, doi: 10.1016/j.tsep.2026.104479.

[23] B. Pillot, G. Guimbretière, C. Révillion, C. Mathiak, and R. Authier, "Scaling up solar cooking studies: A modeling framework for planning sustainable transition of the bakery sector," *Energy Res. Soc. Sci.*, vol. 118, no. September, p. 103815, Dec. 2024, doi: 10.1016/j.erss.2024.103815.

[24] A. Mondal and A. K. Datta, "Bread baking - A review," *J. Food Eng.*, vol. 86, no. 4, pp. 465–474, 2008, doi: 10.1016/j.jfoodeng.2007.11.014.

[25] N. Tsegay, H. Admassu, B. Zegale, and A. Gosu, "Nutritional and functional potentials of wheat, cowpea, and yam composite flours on bread formulations: Effect of blending ratio and baking parameters," *J. Agric. Food Res.*, vol. 18, no. February, p. 101294, 2024, doi: 10.1016/j.jafr.2024.101294.

[26] C. Cevoli, V. Panarese, C. Catalogne, and A. Fabbri, "Estimation of the effective moisture diffusivity in cake baking by the inversion of a finite element model," *J. Food Eng.*, vol. 270, no. March 2019, 2020, doi: 10.1016/j.jfoodeng.2019.109769.

[27] H. Wang, J. Huang, M. Song, and J. Yan, "Effects of receiver parameters on the optical performance of a fixed-focus Fresnel lens solar concentrator/cavity receiver system in

solar cooker," *Appl. Energy*, vol. 237, no. December 2018, pp. 70–82, 2019, doi: 10.1016/j.apenergy.2018.12.092.

[28] U. C. C. Arunachala and A. Kundapur, "Cost-effective solar cookers: A global review," *Sol. Energy*, vol. 207, no. July, pp. 903–916, Sep. 2020, doi: 10.1016/j.solener.2020.07.026.

[29] A. Gallagher, "A solar fryer," *Sol. Energy*, vol. 85, no. 3, pp. 496–505, 2011, doi: 10.1016/j.solener.2010.12.018.

[30] A. Harmim, M. Merzouk, M. Boukar, and M. Amar, "Design and experimental testing of an innovative building-integrated box type solar cooker," *Sol. Energy*, vol. 98, no. PC, pp. 422–433, 2013, doi: 10.1016/j.solener.2013.09.019.

[31] B. Y. Mekonnen and A. Y. Kebede, "Development and Performance Evaluation of a Solar Baking Oven," in *15th National Conference on Machines and Mechanisms*, vol. 3, no. 3, Springer International Publishing, 2020, pp. 610–622. doi: 10.1007/978-3-030-43690-2_46.

[32] R. M. Muthusivagami, R. Velraj, and R. Sethumadhavan, "Solar cookers with and without thermal storage—A review," *Renew. Sustain. Energy Rev.*, vol. 14, no. 2, pp. 691–701, Feb. 2010, doi: 10.1016/j.rser.2008.08.018.

[33] J. Silva, L. Serrano, P. Martins, H. Ferreira, P. Váz, and E. Guerra, "A Case Study of a Solar Oven's Efficiency: An Experimental Approach," *Sustainability*, vol. 17, no. 2, p. 428, Jan. 2025, doi: 10.3390/su17020428.

[34] B. B. Paneru *et al.*, "Solar energy for operating solar cookers as a clean cooking technology in South Asia: A review," *Sol. Energy*, vol. 283, no. October, p. 113004, Nov. 2024, doi: 10.1016/j.solener.2024.113004.

[35] M. T. Farimani, M. Zahraei, A. Faezian, and A. Kianifar, "Novel Method to Design and Construction a Dual-Purpose Solar Oven for Baking Bread," *J Appl Mech Eng*, vol. 11, pp. 1–9, 2022, doi: 10.35248/2168-9873.22.11.433.

[36] Y. T. Aragaw and K. D. Adem, "Development and performance evaluation of tube-type direct solar oven for baking bread," *Heliyon*, vol. 8, no. 11, p. e11502, 2022, doi:

10.1016/j.heliyon.2022.e11502.

[37] S. Nazari, A. Karami, M. Bahiraei, M. Olfati, M. Goodarzi, and H. Khorasanizadeh, “A novel technique based on artificial intelligence for modeling the required temperature of a solar bread cooker equipped with concentrator through experimental data,” *Food Bioprod. Process.*, vol. 123, pp. 437–449, Sep. 2020, doi: 10.1016/j.fbp.2020.08.001.

[38] A. H. Tesfay, M. B. Kahsay, and O. J. Nydal, “Design and development of solar thermal Injera baking: Steam based direct baking,” in *Energy Procedia*, Elsevier B.V., 2014, pp. 2946–2955. doi: 10.1016/j.egypro.2014.10.330.

[39] R. Chaudhary and A. Yadav, “Twin vessel solar cook stove for the simultaneous cooking of two different cooking articles,” *Sol. Energy*, vol. 208, no. January, pp. 688–696, 2020, doi: 10.1016/j.solener.2020.08.032.

[40] D. M. F. Hilda and M. M. Daniel, “Experimental performance assessment of a solar powered baking oven,” *Procedia Manuf.*, vol. 35, pp. 535–540, 2019, doi: 10.1016/j.promfg.2019.05.076.

[41] I. Ayub, A. Munir, A. Ghafoor, W. Amjad, and M. S. Nasir, “Solar Thermal Application for Decentralized Food Baking Using Scheffler Reflector Technology,” *J. Sol. Energy Eng. Trans. ASME*, vol. 140, no. 6, pp. 1–9, 2018, doi: 10.1115/1.4040206.

[42] I. Ayub, A. Munir, W. Amjad, A. Ghafoor, and M. S. Nasir, “Energy- and exergy-based thermal analyses of a solar bakery unit,” *J. Therm. Anal. Calorim.*, vol. 133, no. 2, pp. 1001–1013, 2018, doi: 10.1007/s10973-018-7165-3.

[43] H. T. Retta, M. H. Hailu, A. T. Baheta, and M. G. Haile, “Design of an injera baking system using parabolic trough solar collectors at Mekelle University cafeteria,” *Heliyon*, vol. 10, no. 17, p. e36864, 2024, doi: 10.1016/j.heliyon.2024.e36864.

[44] M. A. A. Moghimi, K. J. J. Craig, and J. P. P. Meyer, “Simulation-based optimisation of a linear Fresnel collector mirror field and receiver for optical, thermal and economic performance,” *Sol. Energy*, vol. 153, pp. 655–678, Sep. 2017, doi: 10.1016/j.solener.2017.06.001.

[45] A. E. Rungasamy, K. J. Craig, and J. P. Meyer, “Comparative performance evaluation of

candidate receivers for an etendue-conserving compact linear Fresnel mirror field," *Sol. Energy*, vol. 231, pp. 646–663, 2022, doi: 10.1016/j.solener.2021.12.014.

[46] M. J. Montes, C. Rubbia, R. Abbas, and J. M. Martínez-Val, "A comparative analysis of configurations of linear fresnel collectors for concentrating solar power," *Energy*, vol. 73, pp. 192–203, 2014, doi: 10.1016/j.energy.2014.06.010.

[47] N. Kincaid, G. Mungas, N. Kramer, M. Wagner, and G. Zhu, "An optical performance comparison of three concentrating solar power collector designs in linear Fresnel, parabolic trough, and central receiver," *Appl. Energy*, vol. 231, no. September, pp. 1109–1121, 2018, doi: 10.1016/j.apenergy.2018.09.153.

[48] Z. Said, M. Ghodbane, A. A. Hachicha, and B. Boumeddane, "Optical performance assessment of a small experimental prototype of linear Fresnel reflector," *Case Stud. Therm. Eng.*, vol. 16, no. August, p. 100541, 2019, doi: 10.1016/j.csite.2019.100541.

[49] P. Mishra, M. Pandey, Y. Tamaura, and S. Tiwari, "Numerical analysis of cavity receiver with parallel tubes for cross-linear concentrated solar system," *Energy*, vol. 220, p. 119609, 2021, doi: 10.1016/j.energy.2020.119609.

[50] M. Babu, S. S. Raj, and A. Valan Arasu, "Experimental analysis on Linear Fresnel reflector solar concentrating hot water system with varying width reflectors," *Case Stud. Therm. Eng.*, vol. 14, no. March, p. 100444, Sep. 2019, doi: 10.1016/j.csite.2019.100444.

[51] I. Ayub, M. S. Nasir, Y. Liu, A. Munir, F. Yang, and Z. Zhang, "Performance improvement of solar bakery unit by integrating with metal hydride based solar thermal energy storage reactor," *Renew. Energy*, vol. 161, pp. 1011–1024, 2020, doi: 10.1016/j.renene.2020.07.133.

[52] S. FIRE, "SOLAR FIRE." [Online]. Available: www.solarefre.com

[53] N. E. Benti, A. B. Aneseyee, A. A. Asfaw, C. A. Geffe, G. A. Tiruye, and Y. S. Mekonnen, "Estimation of global solar radiation using sunshine-based models in Ethiopia," *Cogent Eng.*, vol. 9, no. 1, pp. 1–25, 2022, doi: 10.1080/23311916.2022.2114200.

[54] T. Wendelin, A. Dobos, and A. Lewandowski, "SolTrace: A ray-tracing code for complex

solar optical systems," *Natl. Renew. Energy Lab.*, vol. 303, no. October, pp. 275–3000, 2013.

[55] T. Wendelin, "Soltrace: A new optical modeling tool for concentrating solar optics," *Int. Sol. Energy Conf.*, no. March 2003, pp. 253–260, 2003, doi: 10.1115/ISEC2003-44090.

[56] S. S. Sahoo, S. M. Varghese, C. Suresh Kumar, S. P. Viswanathan, S. Singh, and R. Banerjee, "Experimental investigation and computational validation of heat losses from the cavity receiver used in linear Fresnel reflector solar thermal system," *Renew. Energy*, vol. 55, pp. 18–23, 2013, doi: 10.1016/j.renene.2012.11.036.

[57] R. Mitchell, Y. Wang, M. Izygon, J. Pye, and G. Zhu, "Modeling receiver flux of commercial power tower concentrating solar power plants using ray tracing: a round-robin comparison of SolTrace, Solstice, and TieSOL," *Sol. Energy*, vol. 300, no. March, p. 113785, 2025, doi: 10.1016/j.solener.2025.113785.

[58] S. Y. Jeong, M. P. Shah, J. Martinek, and Z. Ma, "Modeling and experimental demonstration of flux spreading in light trapping planar-cavity solar enclosed particle receivers," 2025. doi: 10.2139/ssrn.5615663.

[59] I. ANSYS, "Ansys Fluent Theory Guide," ANSYS, Inc., Canonsburg, PA, 2021. [Online]. Available: https://dl.cfdexperts.net/cfd_resources/Ansys_Documentation/Fluent/Ansys_Fluent_Theory_Guide.pdf

[60] K. J. Craig, M. Slootweg, W. G. Le Roux, T. M. Wolff, and J. P. Meyer, "Using CFD and ray tracing to estimate the heat losses of a tubular cavity dish receiver for different inclination angles," *Sol. Energy*, vol. 211, no. October, pp. 1137–1158, 2020, doi: 10.1016/j.solener.2020.10.054.

[61] K. Faye, A. Thiam, and M. Faye, "Optimum Height and Tilt Angle of the Solar Receiver for a 30 kWe Solar Tower Power Plant for the Electricity Production in the Sahelian Zone," *Int. J. Photoenergy*, vol. 2021, 2021, doi: 10.1155/2021/1961134.

[62] S. Memme and M. Fossa, "A novel approach for incidence angle modifier calculation of arbitrarily oriented linear Fresnel collectors: Theory, simulations and case studies,"

Renew. Energy, vol. 222, no. December 2023, p. 119857, 2024, doi: 10.1016/j.renene.2023.119857.

[63] A. Santos, D. Canavarro, C. A. Arancibia-Bulnes, P. Horta, and M. Collares-Pereira, “A comparison of secondary optic designs for linear Fresnel collectors with a single tubular absorber,” *Sol. Energy*, vol. 282, no. July, 2024, doi: 10.1016/j.solener.2024.112936.

[64] M. Lin, K. Sumathy, Y. J. Dai, and X. K. Zhao, “Performance investigation on a linear Fresnel lens solar collector using cavity receiver,” *Sol. Energy*, vol. 107, pp. 50–62, 2014, doi: 10.1016/j.solener.2014.05.026.

[65] M. A. Moghimi, K. J. Craig, and J. P. Meyer, “A novel computational approach to combine the optical and thermal modelling of Linear Fresnel Collectors using the finite volume method,” *Sol. Energy*, vol. 116, pp. 407–427, 2015, doi: 10.1016/j.solener.2015.04.014.

[66] M. A. Moghimi, K. J. Craig, and J. P. Meyer, “Optimization of a trapezoidal cavity absorber for the Linear Fresnel Reflector,” *Sol. Energy*, vol. 119, pp. 343–361, 2015, doi: 10.1016/j.solener.2015.07.009.

[67] Y. Qiu, Y. L. He, M. Wu, and Z. J. Zheng, “A comprehensive model for optical and thermal characterization of a linear Fresnel solar reflector with a trapezoidal cavity receiver,” *Renew. Energy*, vol. 97, pp. 129–144, 2016, doi: 10.1016/j.renene.2016.05.065.

[68] S. Yang *et al.*, “Modelling of radiative and convective heat transfer in an open cavity volumetric receiver for a 50-MWth beam-down integrated receiver-storage concentrating solar thermal system,” *Renew. Energy*, vol. 242, no. September 2024, p. 122457, 2025, doi: 10.1016/j.renene.2025.122457.

[69] K. S. Reddy and N. Sendhil Kumar, “Combined laminar natural convection and surface radiation heat transfer in a modified cavity receiver of solar parabolic dish,” *Int. J. Therm. Sci.*, vol. 47, no. 12, pp. 1647–1657, 2008, doi: 10.1016/j.ijthermalsci.2007.12.001.

[70] Z. Altaç and N. Uğurlubilek, “Assessment of turbulence models in natural convection from two- and three-dimensional rectangular enclosures,” *Int. J. Therm. Sci.*, vol. 107, pp. 237–246, 2016, doi: 10.1016/j.ijthermalsci.2016.04.016.

[71] O. López, A. Baños, and A. Arenas, “On the thermal performance of flat and cavity receivers for a parabolic dish concentrator and low/medium temperatures,” *Sol. Energy*, vol. 199, pp. 911–923, 2020, doi: 10.1016/j.solener.2019.07.056.

[72] M. Adavi, S. Gorjian, H. Mokhtarzadeh, and B. Ghobadian, “Development and performance evaluation of an indirect fresnel lens solar cooker with thermal oil storage tank,” *Results Eng.*, vol. 26, no. February, p. 105535, 2025, doi: 10.1016/j.rineng.2025.105535.

[73] J. D. McTigue, L. Hulett, and G. Zhu, “Techno-economic design of a linear Fresnel reflector for industrial process heat,” *Sol. Energy*, vol. 303, no. November 2025, p. 114124, 2026, doi: 10.1016/j.solener.2025.114124.

[74] A. E. Rungasamy, K. J. Craig, and J. P. Meyer, “Comparative study of the optical and economic performance of etendue-conserving compact linear Fresnel reflector concepts,” *Sol. Energy*, vol. 181, no. February 2018, pp. 95–107, 2019, doi: 10.1016/j.solener.2019.01.081.

[75] A. Kundapur and C. V. Sudhir, “Proposal for new world standard for testing solar cookers,” *J. Eng. Sci. Technol.*, vol. 4, no. 3, pp. 272–281, 2009.

[76] T. Kanyowa, G. Victor Nyakujara, E. Ndala, and S. Das, “Performance analysis of Scheffler dish type solar thermal cooking system cooking 6000 meals per day,” *Sol. Energy*, vol. 218, no. August 2019, pp. 563–570, 2021, doi: 10.1016/j.solener.2021.03.019.

[77] I. Alonso *et al.*, “Thermal performance assessment of a novel concentrating solar cooker with equatorial tracking from full load tests,” *Sol. Energy*, vol. 300, no. April, 2025, doi: 10.1016/j.solener.2025.113812.

[78] P. J. Lahkar, R. K. Bhamu, and S. K. Samdarshi, “Enabling inter-cooker thermal performance comparison based on cooker opto-thermal ratio (COR),” *Appl. Energy*, vol. 99, pp. 491–495, 2012, doi: 10.1016/j.apenergy.2012.05.034.

[79] S. C. Mullick, T. C. Kandpal, and A. K. Saxena, “Thermal test procedure for box-type solar cookers,” *Sol. Energy*, vol. 39, no. 4, pp. 353–360, 1987, doi: 10.1016/S0038-

092X(87)80021-X.

[80] H. M. Wassie, M. Z. Getie, M. S. Alem, T. B. Kotu, and Z. M. Salehdress, “Experimental investigation of the effect of reflectors on thermal performance of box type solar cooker,” *Heliyon*, vol. 8, no. 12, p. e12324, 2022, doi: 10.1016/j.heliyon.2022.e12324.

[81] B. Liu, V. Mbabazi, and W. Huang, “Performance Simulation and Optimization of Cylindrical Mirror-Spliced Parabolic Trough Solar Collector,” *Appl. Sci.*, vol. 14, no. 24, 2024, doi: 10.3390/app142411828.

[82] M. Brooks, I. Mills, and T. Harms, “Design, construction and testing of a parabolic trough solar collector for a developing-country application,” *Proc. Sol. World Congr. 2005 Bringing Water to World, Incl. Proc. 34th ASES Annu. Conf. Proc. 30th Natl. Passiv. Sol. Conf.*, vol. 2, pp. 849–854, 2005.

[83] M. Azmi Aktacir *et al.*, “Hot fluid production with condensing solar collector for industrial thermal processes: Development of a 20-kW linear fresnel collector prototype,” *Therm. Sci. Eng. Prog.*, vol. 55, no. 6, p. 102971, Oct. 2024, doi: 10.1016/j.tsep.2024.102971.

[84] G. Morin, J. Dersch, W. Platzer, M. Eck, and A. Häberle, “Comparison of Linear Fresnel and Parabolic Trough Collector power plants,” *Sol. Energy*, vol. 86, no. 1, pp. 1–12, 2012, doi: 10.1016/j.solener.2011.06.020.

[85] A. E. Rungasamy, K. J. Craig, and J. P. Meyer, “A review of linear Fresnel primary optical design methodologies,” *Sol. Energy*, vol. 224, pp. 833–854, 2021, doi: 10.1016/j.solener.2021.06.021.

[86] L. F. L. de Souza, N. Fraindenraich, and C. Tiba, “Evaluation of Linear Fresnel Reflectors,” 2024. doi: 10.2139/ssrn.4923778.

[87] M. Sakin, F. Kaymak-Ertekin, and C. Ilicali, “Convection and radiation combined surface heat transfer coefficient in baking ovens,” *J. Food Eng.*, vol. 94, no. 3–4, pp. 344–349, 2009, doi: 10.1016/j.jfoodeng.2009.03.027.

[88] M. J. Aberuee, M. Ziaei-Rad, and H. Ahmadikia, “The effects of an internal isolated plate on natural convective heat transfer inside an industrial oven,” *Appl. Therm. Eng.*, vol. 144,

pp. 769–778, 2018, doi: 10.1016/j.applthermaleng.2018.08.087.

Appendix

Appendix A: Materials for Solar Bakery Construction

S. No	Item Description	Designation	Specification	Length in mm/quantity
1	Steel Profile	SHS	50× 50 × 3	3350
2	>>	SHS	50× 50 × 2	11300
3	>>	SHS	40× 40 × 2	15464
4	>>	SHS	25× 25 × 2	5950
5	>>	SHS	15× 15 × 1	36000
6	>>	Angle Iron	40× 40 × 3	9870
7	>>	Angle Iron	50× 50 × 5	4000
8	>>	Angle Iron	60× 60 × 6	1400
9	>>	Round tube	Ø45	395
10	>>	Flat Bar	50 × 6	500
11	>>	Flat Bar	50 × 3	200
12	>>	Flat Bar	30 × 4	8340
13	>>	Flat Bar	30 × 3	200
14	>>	Flat Bar	30 × 2	15000
15	>>	Flat Bar	25 × 3	5960
16	Reinforcement Bar	Rebar	Ø8	6960
17	Metal primer	-	4 liter	1pc
18	Metal Paint	-	4 Liter	1 pc
19	Wheelbarrow Wheel	-	Ø350	2 pc
20	Simple straight caster wheel	-	Ø75	2 pc
21	Cater wheel with brake	-	Ø75	2 pc
22	Glass Mirror	Face Mirror	150 × 600 × 3	57 pc
23	Transparent glass	Clear mirror	380 × 380 × 3	1 pc
24	Steel Sheet metal	Receiver plate	100 ×350 ×3	12 pc

Appendix B: Experimental data collection format

Table 1: No Load Test

Time (Hrs.)	$I_G(\frac{W}{m^2})$	T_{ha-C1}	T_{ha-C1}	T_{ha-C1}	T_{S-R}	T_{amb}
10:00 am						
10:15 am						
10:30 am						
10:45 am						
11:00 am						
11:15 am						
11:30 am						
11:45 am						
12:00 am						
12:15 pm						
12:30 pm						
12:45 pm						
1:00 pm						
1:15 pm						
1:30 pm						
1:45 pm						
2:00 pm						
2:15 pm						
2:30 pm						
2:45 pm						
3:00 pm						
3:15 pm						

Where

T_{ha-C1}: Temperature of hot air in the bottom (first) baking compartment

T_{ha-C2}: Temperature of hot air in the middle (Second) baking compartment

T_{ha-C3}: Temperature of hot air in the top (third) baking compartment

T_{S-R}: Surface Temperature of the receiver

$I_G(\frac{W}{m^2})$: Global Irradiance

T_{amb}: Ambient Temperature

Table 2: Load Test Result

Time (Hrs.)	$I_G(\frac{W}{m^2})$	T_{ha-C1}	T_{ha-C1}	T_{ha-C1}	T_{S-R}	T_{BC}	T_{amb}
10:00 am							
10:15 am							
10:30 am							
10:45 am							
11:00 am							
11:15 am							
11:30 am							
11:45 am							
12:00 am							
12:15 pm							
12:30 pm							
12:45 pm							
1:00 pm							
1:15 pm							
1:30 pm							
1:45 pm							
2:00 pm							
2:15 pm							
2:30 pm							
2:45 pm							
3:00 pm							
3:15 pm							

Where

T_{ha-C1}: Temperature of hot air in the bottom (first) baking compartment

T_{ha-C2}: Temperature of hot air in the middle (Second) baking compartment

T_{ha-C3}: Temperature of hot air in the top (third) baking compartment

T_{S-R}: Surface Temperature of the receiver

T_{BC}: Temperature of bread core

$I_G(\frac{W}{m^2})$: Global Irradiance

T_{amb}: Ambient Temperature

Appendix C: ANSYS exporter for SolTrace

This Code processes the ANSYS mesh file output of the receiver zones and generates the input files for SolTrace simulation which its code, lk script, is presented in Appendix D.

```
#!/usr/bin/env python3
"""
SolTrace + ANSYS exporter (summary version):
 - Reads mirror centers and receiver zones
 - Computes sun vector (Duffie & Beckman)
 - Applies 60° tilt and alignment
 - Assigns focal lengths and curvature
 - Builds receiver/mirror files for SolTrace
"""

import os, csv, math, numpy as np, meshio

# Configuration
ZONES_DIR = r"C:\Users\path"
ABSORBER_VTK = os.path.join(ZONES_DIR, "absorber2.vtk")
MIRROR_BASE  = os.path.join(ZONES_DIR, "mirrors_base.tsv")
MIRROR_WX, MIRROR_WY = 0.15, 0.60
row_to_F = {0.720: 3.001, 1.334: 3.389, 1.974: 3.894}
REC_TX, REC_TY, REC_TZ = 0.0, 1.510, -3.06

def sun_dir(lat_deg, day_of_year, hour_solar, gamma_deg=0.0):
    """Compute sun vector (Duffie & Beckman)."""
    φ = math.radians(lat_deg)
    ω = math.radians(15.0*(hour_solar - 12.0))
    δ = math.radians(23.45*math.sin(2*math.pi*(284+day_of_year)/365.0))
    α          =          math.asin(math.sin(φ)*math.sin(δ)          +
math.cos(φ)*math.cos(δ)*math.cos(ω))
    A     =     math.atan2(math.sin(ω),     math.cos(ω)*math.sin(φ)     -
math.tan(δ)*math.cos(φ)) + math.radians(gamma_deg)
    return        np.array([math.cos(α)*math.sin(A),        math.sin(α),
math.cos(α)*math.cos(A)])
    return vec
def load_mirror_centers(path):
    """Load mirror base positions. from .txt"""
      with open(path) as f: return np.array([list(map(float,row.split())) for
      row in f])
    return centers
def apply_field_tilt_X(mirrors, theta_deg, pivot_y):
    """Tilt mirror field about X axis."""
    th = math.radians(theta_deg)
    Rx             =             np.array([[1,0,0],[0,math.cos(th),
math.sin(th)],[0,math.sin(th),math.cos(th)]])
    mirrors[:,1] = pivot_y
    mirrors = (Rx @ mirrors.T).T
    mirrors[:,1] = pivot_y
    return mirrors
def write_receiver_files(shift, mirror_mean):
    """Export receiver zone files."""
    # Implementation omitted
    return active_count, side_count
```

```
def compute_mirror_aims(mirrors, sun_vec, tri_centroids, mirror_plate):
    """Bisector aiming toward absorber centroids."""
    # Implementation omitted
    return aim_rows
# -------------------- MAIN PIPELINE --------------------
if __name__ == "__main__":
    # 1) Load mirrors
    mirrors = load_mirror_centers(MIRROR_BASE)
    # 2) Align and tilt
    mirrors = apply_field_tilt_X(mirrors, theta_deg=60.0, pivot_y=0.72)
   # 3) Receiver export
    active,    side    =    write_receiver_files([REC_TX,    REC_TY,    REC_TZ],
mirrors.mean(axis=0))
    # 4) Sun vector
    sun_vec = sun_dir(9.03, 148, 12.0)

    # 5) Mirror aims
  aim_rows    =    compute_mirror_aims(mirrors,    sun_vec,    tri_centroids=None,
mirror_plate=None)

   # Export results
    print("Receiver export:", active, side)
    print("Sun vector:", sun_vec)
    print("Exported mirror aims:", len(aim_rows))
```

Appendix D: SolTrace lk script

The code was developed using the LK scripting language in SolTrace to perform Monte Carlo ray tracing for a Linear Fresnel parabolic mirror reflector. Receiver zones (absorber, glass, and sidewall) were generated using the ANSYS exporter for SolTrace (Appendix C) and used as input files.

```
// ==============================
// Helpers
// ==============================
// Sun setup
// ==============================
latitude_deg = 9.03;day_of_year = 150; hour_solar = 12.0;gamma_deg = 0.0;phi =
deg2rad(latitude_deg);
gamma = deg2rad(gamma_deg);omega = deg2rad(15 * (hour_solar - 12));decl = deg2rad(23.45 *
sin(2*PI*(284 + day_of_year)/365));alt = asin(sin(phi)*sin(decl) + cos(phi)*cos(decl)*cos(omega));az =
atan2(sin(omega), cos(omega)*sin(phi) - tan(decl)*cos(phi)) + gamma;sx = cos(alt) * sin(az);sy =
sin(alt);sz = cos(alt) * cos(az);
// Assign to SolTrace Sun object
// ==============================
// File paths
// ==============================
// Direct Optics
// ==============================
clearoptics();
// ---------- Stage Optics ----------
```

```
addoptic("stage_optics ");general_ stage _optics_front.refl = value;general_ stage _optics_front.trans =
value;general_ stage _optics_front.errslope = value; general_ stage _optics_front.errspec =
value;general_ stage _optics_front.refractr = value; general_ stage _optics_back.refl = value;general_
stage _optics_back.trans = value;general_ stage _optics_back.errslope = value;general_ stage
_optics_back.errspec = value;general_ stage _optics_back.refractr = value;opticopt("stage _optics", 1,
general_optics_front);opticopt("stage _optics ", 2, general_optics_back);
// ==============================
// Stages
// ==============================
clearstages();
// -------- mirror_stage (Stage 1) --------
addstage("mirror_stage");activestage("mirror_stage");MirrorStage = {};
MirrorStage.virtual = false;
MirrorStage.multihit = false; // one hit per mirror
MirrorStage.tracethrough = false; // opaque
MirrorStage.x = 0; MirrorStage.y = 0; MirrorStage.z = 0;
MirrorStage.ax = 0; MirrorStage.ay = 0; MirrorStage.az = 1;
MirrorStage.zrot = 0;
stageopt("mirror_stage", MirrorStage);
// front/back optics
stageopt("mirror_stage", "frontsurf", "MirrorOptic");
stageopt("mirror_stage", "backsurf", "black_absorber");
mf = open(mirror_file, "r");
if (!mf) { outln("ERROR opening mirrors: " + mirror_file); exit; }
MirrorCount = 0;
line = "";
while (read_line(mf, line)) {
 if (line == "") continue;
 parts = split(line, "\t");
 addelement();
 idx = nelements()-1;
 md = {};
 md.en = true;
 md.x = to_real(parts[0]); md.y = to_real(parts[1]); md.z = to_real(parts[2]);
 md.ax = to_real(parts[3]); md.ay = to_real(parts[4]); md.az = to_real(parts[5]);
 md.zrot = (parts[6] ? to_real(parts[6]) : 0);
 md.aper = ['r',
 to_real(parts[7]), to_real(parts[8]),
 0,0,0, 0,0,0];
 md.surf = ['p',to_real(parts[9]),to_real(parts[10]),0,0,0, 0,0,0];
 md.optic = "MirrorOptic";
 elementopt(idx, md);
 MirrorCount++;
}
outln("Mirrors loaded: " + MirrorCount);
// -------- glass_stage (Stage 2) --------
// -------- absorber_stage (Stage 3) --------
// -------- sidewall_stage (Stage 4) --------
// ==============================
// Trace
// ==============================
```

```
// =====================
// CONFIGURATION
// =====================
amount_of_seeds = 10; // 10 seed
amount_of_rays = 10000000; // 10 M rays per seed
ray_data_file = 0;
element_hit_file = 1;
I_n = 1000.0; // DNI [W/m_]
ProjectName = "Folder";
// =====================
s_abs = 3; // mirror=1, glass=2, absorber=3
for (seed = 1; seed <= amount_of_seeds; seed = seed + 1) {
 project_path = cwd() + "\\" + ProjectName;
 seed_str = (seed < 10) ? "0" + seed : "" + seed;
 // 1) Trace
 traceopt({
 'rays' = amount_of_rays,
 'maxrays' = amount_of_rays,
 'seed' = seed,
 'cpus' = 6,
 'include_sunshape'= true,
 'optical_errors' = true
 });
 PowerPerRay = to_real(I_n) * Tarea / max(nr,1);
 if (!isFiniteVal(PowerPerRay) || PowerPerRay <= 0) {
 outln("ERROR: PowerPerRay=" + PowerPerRay + " _ forcing 0");
 PowerPerRay = 0.0;
 }
 // load element_metrics.txt
 area_file_path = project_path + "\\element_metrics.txt";
 if (!file_exists(area_file_path)) {
 outln("ERROR: matrix file not found, abort seed " + seed);
 continue;

 // write CSV via rayhits()
 // after activestage("absorber_stage") and reading absorber_list/absorber_area_
 outcsv = project_path
 + "\\Element_Hit_Results_seed" + seed_str
 + "_rays" + amount_of_rays + ".csv";

 }
}
```

Appendix E: ANSYS UDF

The absorber surface was mapped using the radiative heat flux q″(x,y)q"(x,y)q″(x,y) through a user-defined function (UDF) (`udf_soltrace_flux_profile: libudf`). The UDF transfers SolTrace power density values (W/m²) to the corresponding mesh faces and was applied in ANSYS Fluent as a boundary condition for the absorber walls, as presented below.

```
#include "udf.h"
#include <stdio.h>
#include <stdlib.h>
#include <string.h>
#include <math.h>
/* ---------------- USER CONFIG ---------------- */
#define absorber_wall_id  8   /* from .msh: wall absorber */
#define glass_wall_id     7   /* from .msh: wall glass */
#define fluid_zone_id     3   /* from .msh: fluid part_8-solid */
#define N_FLUID_PTS 5
static const real fluid_pts[N_FLUID_PTS][3] = {
/* Transform from Fluent mesh frame to SolTrace global */
static const double T_TX = 0.0, T_TY = 1.510, T_TZ = -3.06;
/* ---------------- GLOBALS ---------------- */
/* ---------------- HELPERS ---------------- */
static inline void apply_transform(const real c[ND_ND], double p[3])
{
   /* Ry(+90): [x',y',z'] = [ z, y, -x ] */
   const double xr = c[2], yr = c[1], zr = -c[0];
   p[0] = xr + T_TX;
   p[1] = yr + T_TY;
   p[2] = zr + T_TZ;
/* ---------------- INIT ---------------- */
DEFINE_INIT(read_flux_and_elements, domain)
      Message("INIT: loaded fluxes and %d absorber elements; faces cap=%d\n", n_elements,
UDF_MAX_FACES);       }
/* ---------------- PROFILE (APPLY FLUX) ---------------- */
DEFINE_PROFILE(soltrace_flux_profile, thread, i)
/* ---------------- REPORT HELPERS ---------------- */
static real fluid_T_near_point(Thread* ft, const real P[3], real *out_d)
{
   /* 5) Write probes CSV */
#if PARALLEL
#endif /* !RP_HOST */
}
```

Appendix F: Part drawings

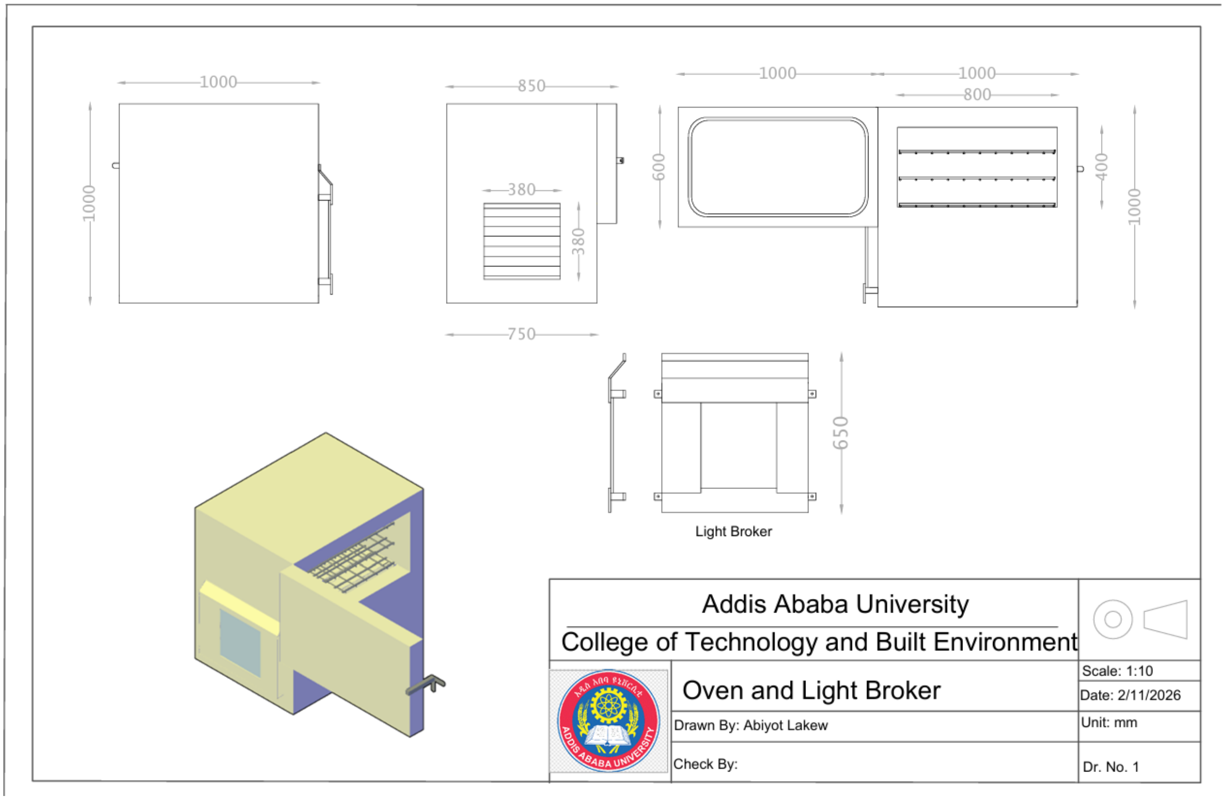

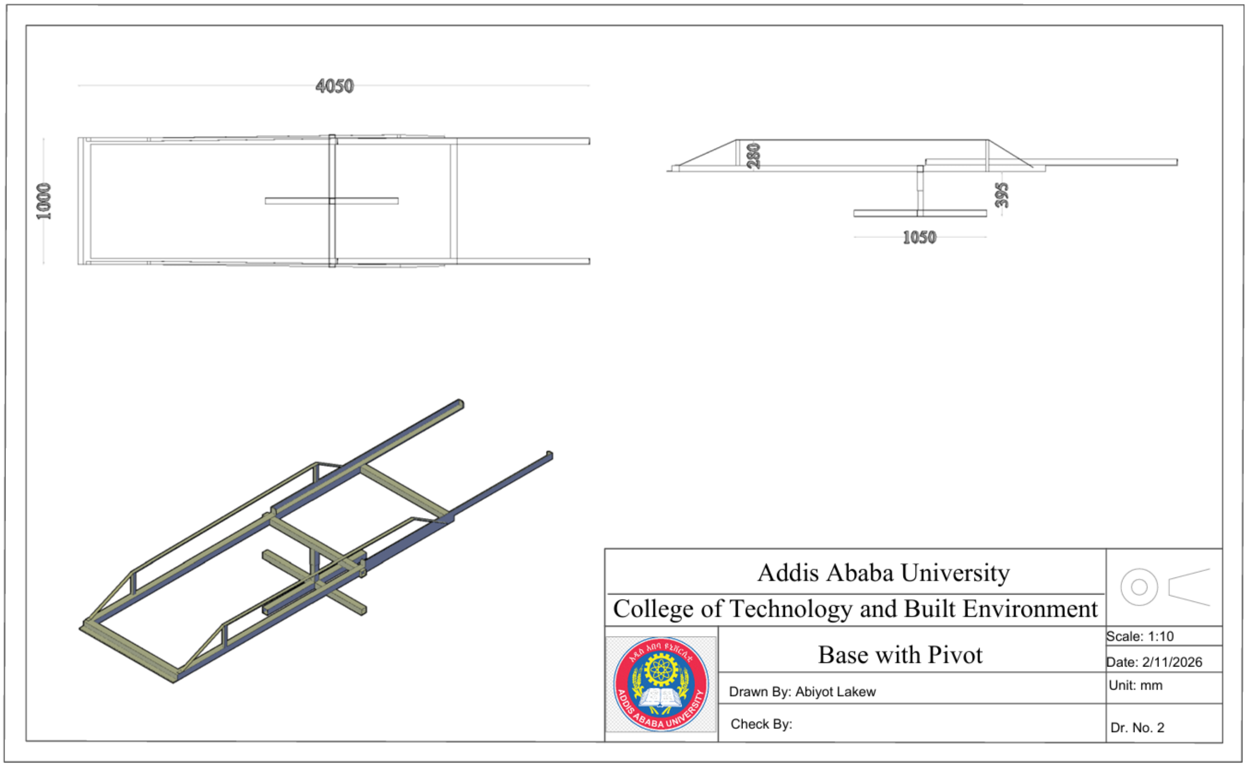

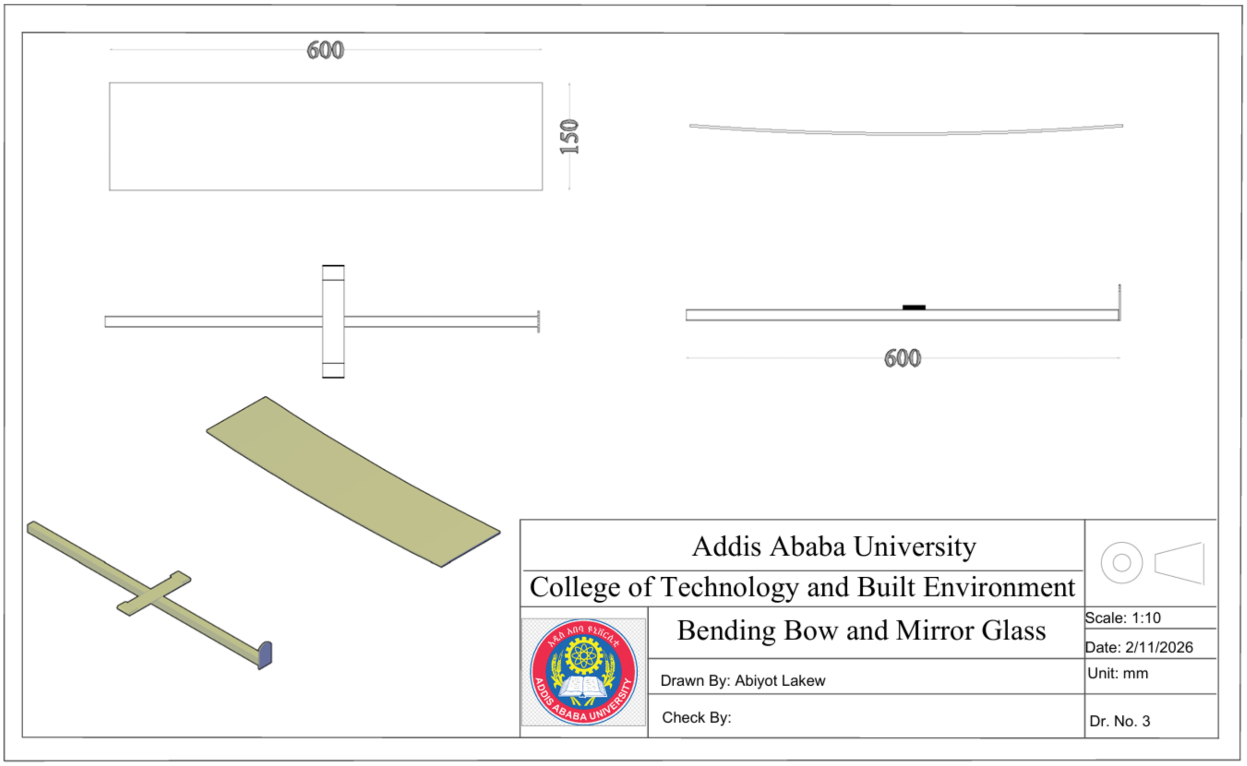

Addis Ababa University
College of Technology and Built Environment
Bending Bow and Mirror Glass
Drawn By: Abiyot Lakew
Check By:
Scale: 1:10
Date: 2/11/2026
Unit: mm
Dr. No. 3

Appendix G: Construction of Prototype